

國立臺灣大學生物資源暨農學院農業化學系

碩士論文

Department of Agricultural Chemistry  
College of Bioresources and Agriculture

National Taiwan University

Master Thesis

探討鹵素離子對二氧化鈦奈米顆粒聚集和紫外光照下  
光催化降解磺胺甲噁唑之效應

The effect of halide ions on the aggregation of TiO<sub>2</sub>  
nanoparticles and photocatalytic degradation of  
sulfamethoxazole

林宜璇

Yi-Hsuan Lin

指導教授：施養信 博士

Advisor: Yang-hsin Shih, Ph.D.

中華民國 107 年 7 月

July 2018



## 誌謝



首先要感謝指導教授 施養信博士。謝謝老師在我大三進入實驗室後鼓勵我申請大專生計畫，並在我執行計畫時給了我很多指導與實驗建議，讓我在大學時就熟悉儀器的操作、數據處理與文獻整理。進入研究所之後更鼓勵我多方嘗試研究，在我遇到實驗上的瓶頸時給予支持與鼓勵，每次與老師討論之後總能更好地思考研究的方向。謝謝老師時常關心學生的身體健康，邀約我們一起去運動，也常常提醒大家實驗安全第一。還要感謝老師時常鼓勵我練習上台報告並以英文演講，增加我的自信，並帶大家參加國內外的研討會磨練膽量及開拓視野，勉勵大家積極參加競賽與爭取獎學金。這本論文的完成需要感謝老師的指導與建議。感謝老師這三年多以來的諄諄教誨與照顧，我獲益良多，相信碩士班的訓練以及研究精神的培養對我來說能夠一生受用。

感謝臺大環工所的 吳先琪博士、交大環工所的 董瑞安博士以及輔英科大環工系的 陳世裕博士於百忙之中撥空出席口試，並在口試時給予我許多重要的建議與不同的思考方向，使論文及研究更加完整。

感謝實驗室的所有成員，謝謝博後優慧學姊、向宸學長、如邦學長、子禾學長、Rama，助理千瑩學姊、哲豪學長、文齊學姊以及天宇學長，還有學長姊穎捷、朝源、進順、冠博、佳燊和 Hepsiba 以及學弟妹明翰、吳珍、安均、恩生、蕙真、雅文、德宇、書頡等人平時的陪伴、鼓勵還有實驗上的幫助。謝謝你們總是讓實驗室充滿歡笑以及共同努力的氣氛。更要感謝同屆的張茗，一路走來我們互相扶持，一起討論實驗、激盪彼此的想法。很開心我們都順利完成了研究，祝福我們未來一切順利！

感謝我的父母親及弟弟們的支持，使我能無後顧之憂地完成學業與研究。感謝從大學就認識，到研究所還是同學的好朋友佳娟、卓穎、家莉和聆亦，謝謝妳們的陪伴讓我的碩士生涯多采多姿。

## 摘要



磺胺甲噁唑(Sulfamethoxazole, SMZ)是一種於人類及動物醫療常用的抗生素。SMZ 流佈於水體中造成污染，是目前最需進行詳細風險評估及發展處理方法的污染物之一。光催化降解被視為最有效快速移除 SMZ 的方法之一，其中二氧化鈦(titanium dioxide,  $\text{TiO}_2$ )奈米顆粒為典型且具有發展潛力的光催化奈米材料。其具有很好的穩定性，但在含有鹽類的環境下， $\text{TiO}_2$  奈米顆粒易發生聚集與沉降現象，進而減少比表面積與表面活性位置，可能會降低其光催化效率。然而本研究發現當系統中含有 NaBr 時，會使 P25 (一種商用  $\text{TiO}_2$ )奈米顆粒聚集，但其光降解 SMZ 之速率不但沒有降低，甚至隨著鹽類濃度上升而升高。紫外光照 2 小時後，P25 可以降解 75% 的 SMZ，而當系統中有 100 mM NaBr 時，光照 45 分鐘即可降解 95% 的 SMZ，其降解反應速率常數為  $0.0636 \text{ min}^{-1}$ ，比 P25 的速率常數  $0.0104 \text{ min}^{-1}$  高 6 倍。因此本研究的目的是瞭解  $\text{TiO}_2$  在不同條件下降解 SMZ 的速率變化，與探討在含有鹵素鹽類的系統中  $\text{TiO}_2$  光催化降解 SMZ 的機制，並找出可能使之促進反應的原因。從以草酸根離子作為光生電洞的捕捉劑實驗中可發現，P25 + 100 mM NaBr 的組別其反應比 P25 被抑制地更多，顯示 NaBr 促進反應的原因跟光生電洞有關。以 coumarin 和 coumarin-3-carboxylic acid (CCA) 分別測定溶液中和近  $\text{TiO}_2$  表面的  $\cdot\text{OH}$ ，在 P25 的組別皆可測到此兩種  $\cdot\text{OH}$ ，但系統中含有 NaBr 時，則無法測到  $\cdot\text{OH}$ ，表示  $\text{Br}^-$  也會與  $\cdot\text{OH}$  發生反應。N,N-diethyl-p-phenylenediamine (DPD) 實驗結果證實了 P25 + NaBr 經紫外光照的系統中產生了活性溴物種。另外，系統中可能也有  $\text{Br}_2$  的產生。由於  $\text{Br}_2$  會與 cyclohexene 反應產生 dibromocyclohexane，也會與  $\text{Br}^-$  反應產生  $\text{Br}_3^-$ ，而系統中可以測得以上兩種產物，證實反應過程中有產生  $\text{Br}_2$ 。這很可能是因為在有 NaBr 的情況下， $\text{Br}^-$  與光生電洞和  $\cdot\text{OH}$  反應產生  $\cdot\text{Br}$ ，進而產生其他活性溴物種，包含  $\text{Br}_2$ ，來促進  $\text{TiO}_2$  降解 SMZ，且此反應可能發生在  $\text{TiO}_2$  表面。本研究中有

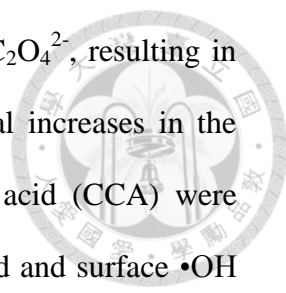
製備一種材料將 Br 修飾在 P25 表面，而此材料對於 SMZ 的光催化降解也有促進的效應，並且以 DPD 法也可以測得活性溴物種，顯示促進反應的關鍵在表面。在以 allyl alcohol (AA) 作為表面活性氧物種( $\cdot\text{OH}$ 、 $\cdot\text{Br}$  等)的捕捉者，tertiary butanol (*t*-buOH)為溶液中活性氧物種捕捉者的實驗中，P25 的光催化反應皆會被抑制，且抑制程度相近，但在系統中含有 NaBr 時，加入 AA 的反應會有非常明顯的抑制情形，而加入 *t*-buOH 則只會稍微抑制反應，證明表面活性氧物種作用的重要性。最後以 HPLC-MS 分析副產物，發現系統中會存在 SMZ 的溴化產物，分別是在苯環或胺基上接上一個 Br，以及在苯環位置接上 2 個溴，間接證實了系統中有產生活性溴物種去攻擊 SMZ。

關鍵字：二氧化鈦，光催化降解，磺胺甲噁唑，溴離子，活性鹵素自由基

## Abstract



Since the widespread detection of synthetic antibiotics in aquatic environments is raising public health concerns, there is growing interest in the development of technologies to efficiently remove these antibiotics. Photocatalysis is a green technology to treat the wastewater with antibiotics such as sulfamethoxazole (SMZ), one of the broad-spectrum antibiotics. Titanium dioxide ( $\text{TiO}_2$ ) is the most well-known and promising photocatalyst. However, in natural water systems,  $\text{TiO}_2$  may be subject to the deactivation by the presence of inorganic ions, including halide anions. The presence of halide anions can have both positive and negative influence on the photocatalytic performance. This study aims to investigate the photocatalytic degradation mechanism of SMZ in aqueous suspensions of P25, one commercial  $\text{TiO}_2$ , nanoparticles (NPs) with the addition of halide salts. When there were halide salts in the solution, P25 aggregated and became larger particle agglomerates, resulting in the decrease of surface area and active site on the surface, which reduced the photocatalytic performance of  $\text{TiO}_2$ . Therefore, the addition of NaCl slowed down the photodegradation rate. However, the photodegradation rate of SMZ by  $\text{TiO}_2$  with the addition of NaBr increased instead of decreasing. With the addition of 100 mM NaBr, the photodegradation efficiency was 95% after 45 min illumination, and reached equilibrium of 99% removal efficiency at 75 min. The photodegradation rate constant of P25 was  $0.0104 \text{ min}^{-1}$ , increasing to  $0.0636 \text{ min}^{-1}$  with the addition of 100 mM NaBr. Since the increase of degradation kinetics enlarged with the increase of NaBr concentration, the enhancement of SMZ degradation could be related to the presence of bromide ions. The degradation of SMZ by P25 was significantly inhibited by allyl alcohol (AA) and tertiary butanol (*t*-buOH), two oxidant scavengers. The



photogenerated holes on the surface of TiO<sub>2</sub> were consumed by C<sub>2</sub>O<sub>4</sub><sup>2-</sup>, resulting in the inhibition of SMZ degradation. Under UV irradiation, gradual increases in the fluorescence of TiO<sub>2</sub> with coumarin and coumarin-3-carboxylic acid (CCA) were observed with the UV irradiation time, indicating that the dissolved and surface •OH increased. However, with the addition of NaBr, the generation of both surface and dissolved •OH was totally inhibited. Furthermore, the results of N,N-diethyl-p-phenylenediamine (DPD) test depicted that there were reactive bromine species generated in the system of P25 with NaBr. By the cyclohexene test, the production of bromine on the surface of P25 with NaBr was confirmed by dibromocyclohexane. Some Br<sup>-</sup> even reacted with bromine to form Br<sub>3</sub><sup>-</sup>. Under UV light irradiation, Br<sup>-</sup> was proposed to react with the photogenerated holes of TiO<sub>2</sub> or •OH to produce •Br and reactive bromine species, accelerating the photodegradation of SMZ. Compared to P25, surface brominated P25 (HBr-P25) had an enhanced photocatalytic performance. Reactive bromine species generated on HBr-P25 were also detected by DPD method and the cyclohexene test. On the other hand, in the system of P25 with 100 mM NaBr, the degradation rate of SMZ was significantly decreased by AA (surface-bound oxidants scavenger), but was slightly decreased by *t*-buOH (dissolved oxidants scavenger), thus confirming the importance of surface-bound oxidants. This enhanced reaction by bromide ions occurred on the surface of TiO<sub>2</sub>. Reactive bromine species can react with unsaturated bonds and electron-rich moieties such as aromatic rings to form halogenated products. HPLC-MS results showed that there were two halogenated byproducts, mono and di-brominated derivatives of SMZ, in the photodegradation process of SMZ by P25 in the presence of NaBr and by HBr-P25.

Keywords: Titanium dioxide, photocatalytic degradation, sulfamethoxazole (SMZ), bromide ion, reactive halogen species (RHS)

# Table of contents



誌謝.....	I
摘要.....	II
Abstract.....	IV
Table of contents .....	VI
List of Tables.....	IX
List of Figures .....	XI
Chapter 1 Introduction .....	1
Chapter 2 Literature Review .....	4
2.1 Introduction of sulfamethoxazole (SMZ) .....	4
2.1.1 The environmental issue of sulfamethoxazole (SMZ).....	4
2.1.2 The removal of SMZ by different methods .....	5
2.2 Introduction of titanium dioxide (TiO <sub>2</sub> ).....	6
2.2.1 The titanium dioxide (TiO <sub>2</sub> ).....	6
2.2.2 The principle of photocatalytic degradation .....	6
2.2.2.1 Effect of particle size .....	10
2.2.2.2 Effect of pH.....	12
2.2.2.3 Effect of halide ions .....	15
2.3 Introduction of reactive halogen species (RHS) .....	17
2.3.1 The formation of halogen molecules from TiO <sub>2</sub> powder .....	19
2.3.2 The formation of RHS from hydroxyl radicals.....	20
2.3.3 Photocatalytic transformation of organic compounds with halide ions .....	22
2.4 Introduction of natural organic matter (NOM) .....	23
Chapter 3 Materials and methods .....	26
3.1 Chemicals.....	26
3.2 Synthesis of HBr-P25, HCl-P25, NaBr-P25 and NaCl-P25 .....	26
3.3 Characterization .....	27
3.3.1 Dynamic light scattering (DLS).....	27
3.3.2 Transmission electron microscope (TEM).....	27
3.3.3 Field-emission scanning electron microscope (SEM) .....	27
3.3.4 Brunauer-Emmett-Teuller (BET) surface area.....	28
3.3.5 X-ray diffraction (XRD) .....	28
3.3.6 Fourier transform infrared spectroscopy (FTIR) .....	28
3.3.7 Raman spectroscopy .....	29
3.3.8 X-ray photoelectron spectroscopy (XPS) .....	29

3.4	Aggregation and sedimentation of TiO <sub>2</sub> .....	29
3.5	Photodegradation experiments.....	30
3.6	Photoluminescence (PL) .....	30
3.7	Photocurrent.....	31
3.8	ROS measurements.....	31
3.8.1	Trapping experiments of radicals and holes.....	31
3.8.2	The measurements of hydroxyl radicals .....	32
3.8.3	The measurement of chlorine and bromine species .....	33
3.8.4	The measurement of bromine by dibromocyclohexane test .....	35
3.8.5	The measurement of photocatalytic sites by TBO method .....	36
3.8.6	Transient absorption spectra (TAS) .....	36
3.8.7	Halide ions .....	37
3.9	Analytical methods.....	37
3.9.1	HPLC .....	37
3.9.2	Byproducts and mineralization efficiency .....	38
3.10	Calculation .....	38
3.10.1	SMZ reaction rate constants.....	38
3.10.2	Removal efficiency .....	39
Chapter 4	Results and Discussion.....	40
4.1	Characterization of TiO <sub>2</sub> .....	40
4.1.1	DLS, zeta potential, TEM, and SEM-EDX.....	40
4.1.2	BET surface area .....	42
4.1.3	XRD .....	44
4.1.4	FTIR.....	46
4.1.5	Raman .....	48
4.1.6	XPS .....	50
4.2	Aggregation and sedimentation of TiO <sub>2</sub> .....	51
4.2.1	The effect of TiO <sub>2</sub> concentration .....	52
4.2.2	The effect of sodium halides .....	53
4.2.3	HBr, HCl, NaBr and NaCl modified TiO <sub>2</sub> .....	54
4.2.4	The effect of NOM.....	57
4.3	Photocatalytic degradation of SMZ by TiO <sub>2</sub> .....	59
4.3.1	The effect of TiO <sub>2</sub> dosage on the removal of SMZ.....	59
4.3.2	The effect of the initial SMZ concentration on photodegradation.....	61
4.3.3	The effect of sodium halide concentration on the removal of SMZ ...	62
4.3.3.1	The effect of NaCl concentration on the removal of SMZ .....	63
4.3.3.2	The effect of NaBr concentration on the removal of SMZ .....	67
4.3.3.3	The effect of pH on the removal of SMZ in the presence of 100	



mM Br <sup>-</sup> .....	71
4.3.4 Photocatalytic degradation of SMZ by surface modified TiO <sub>2</sub> .....	74
4.3.5 The effect of NOM on the removal of SMZ .....	78
4.4 The Mechanism of photocatalytic degradation.....	83
4.4.1 The effect of different scavengers on the removal of SMZ .....	83
4.4.1.1 The effect of oxidants' scavengers on the removal of SMZ by TiO <sub>2</sub> .....	83
4.4.1.2 The effect of photogenerated hole scavengers on the removal of SMZ by TiO <sub>2</sub> .....	85
4.4.2 Photoluminescence of TiO <sub>2</sub> .....	88
4.4.3 Photocurrent measurements .....	91
4.4.4 Radical measurements .....	92
4.4.4.1 The measurement of hydroxyl radicals by coumarin and CCA method.....	92
4.4.4.2 The measurement of reactive bromine species by DPD method .....	96
4.4.4.3 The measurement of bromine by dibromocyclohexane test ....	97
4.4.4.4 The measurement of tribromide ion.....	100
4.4.4.5 The measurement of photocatalytic sites by TBO method ....	101
4.4.4.6 Transient absorption spectra (TAS) .....	102
4.4.5 Byproducts measurements .....	103
Chapter 5 Conclusion.....	110
References.....	114
Appendix.....	129

## List of Tables



Table 2-1. Reduction potentials of one-electron inorganic couples (Isse et al., 2010).	22
Table 2-2. Aqueous phase bromine reactions (B. M. Matthew & C. Anastasio, 2006).	25
.....	25
Table 4-1. The surface area, pore diameter and pore hydraulic radius of P25 with different concentrations of NaBr.	45
Table 4-2. The surface area, pore diameter and pore hydraulic radius of P25 with different concentrations of NaCl.	46
Table 4-3. The surface area, pore diameter and pore hydraulic radius of different types of TiO <sub>2</sub> .	47
Table 4-4. The pH and SMZ photodegradation rate constant of different concentrations of P25 under UV-C light.	60
Table 4-5. The pH and SMZ photodegradation rate constant of different concentrations of P25 under UV-A light.	61
Table 4-6. The pH and SMZ photodegradation rate constant of P25.	63
Table 4-7. The pH, SMZ photodegradation rate constant, and final particle size at different concentrations of NaCl.	67
Table 4-8. The pH, SMZ photodegradation rate constant and final particle size at different concentrations of NaBr.	71
Table 4-9. The pH measurements and rate constants of the degradation of SMZ in the presence of 100 mM Br <sup>-</sup> at acidic pH.	73
Table 4-10. The pH measurements and rate constants of the degradation of SMZ in the presence of 100 mM Br <sup>-</sup> at alkaline pH.	74
Table 4-11. The pH and SMZ photodegradation rate constant of P25, HBr-P25 and HCl-P25 powder.	77
Table 4-12. The pH and SMZ photodegradation rate constant of P25, NaBr-P25 and NaCl-P25 powder.	78
Table 4-13. The released halide ions in solutions from HBr-P25, HCl-P25, NaBr-P25 and NaCl-P25 powder before and after photodegradation experiments detected by IC.	78
.....	78
Table 4-14. The pH and SMZ photodegradation rate constant of P25 with different concentrations of LHA in the presence of 100 mM NaBr.	82
Table 4-15. The pH and SMZ photodegradation rate constant of P25 with different concentrations of SRHA in the presence of 100 mM NaBr.	82
Table 4-16. Some selected characteristics of LHA and SRHA reported by IHSS. (Criquet et al., 2015; Hakim & Kobayashi, 2018; Ritchie & Perdue, 2003)	82

Table 4-17. The pH and SMZ photodegradation rate constant of P25 with 100 mM scavengers (AA and <i>t</i> -buOH) in the presence of 100 mM NaBr. ....	84
Table 4-18. The pH and SMZ photodegradation rate constant of P25 with 10 mM Na <sub>2</sub> C <sub>2</sub> O <sub>4</sub> (hole scavenger) in the presence of 100 mM NaBr. ....	87
Table 4-19. The pH and SMZ photodegradation rate constant of P25 with 10 mM C <sub>2</sub> O <sub>4</sub> <sup>2-</sup> (hole scavenger) in the presence of 100 mM NaBr. ....	88
Table 4-20. The structure and m/z ([M+H] <sup>+</sup> ) of susceptible byproduct.....	107
Table 4-21. The structure and m/z ([M+H] <sup>+</sup> ) of brominated byproducts.....	108

## List of Figures

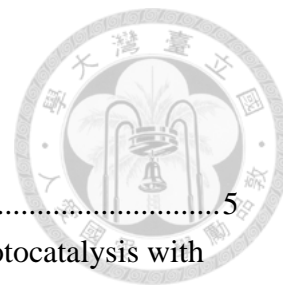


Figure 2-1. The chemical structure of sulfamethoxazole (SMZ).....	5
Scheme 2-1. Schematic diagram illustrates the principle of TiO <sub>2</sub> photocatalysis with the presence of water pollutant (RH) (Dong et al., 2015).....	7
Figure 2-2. Mechanism of photoinduced hydrophilicity (Fujishima et al., 2000).....	9
Scheme 2-2. Increased photocatalytic activity through energy/exciton transfer in aggregated photocatalyst particles (antenna effect) (Wang et al., 2003). ....	11
Scheme 2-3. Illustration of TiO <sub>2</sub> Nanoparticles Aggregate Assembly Employed for the Dye-Sensitized Production of H <sub>2</sub> (Park et al., 2013). ....	12
Figure 2-3. Acid–base dissociation equilibrium of SMZ (Xekoukoulotakis et al., 2011). ....	13
Scheme 2-4. Generation of RHS in waters through the action of sunlight (Yang & Pignatello, 2017). ....	19
Scheme 3-1. Fe <sup>3+</sup> mediated current collection on an inert C electrode immersed in UV-illuminated TiO <sub>2</sub> suspension. ....	31
Figure 3-1. Reactions for detection of •OH with fluorescence probes, (a) coumarin, and (b) coumarin-3-carboxylic acid (CCA), which become corresponding fluorescent molecules to be measured with a common fluorescence spectrometer. (Nosaka & Nosaka, 2017) .....	33
Figure 3-2. The reaction between DPD and chlorine in water (Van London Company, 2015). ....	34
Figure 3-3. The bromination of cyclohexene.....	36
Figure 3-4. The absorbance spectrum of SMZ. ....	38
Figure 4-1. The DLS measurements of (a) P25, (b) HBr-P25, (c) HCl-P25, (d) NaBr-P25, (e) NaCl-P25, and (f) zeta potential measurements of P25, HBr-P25 and HCl-P25. ....	41
Figure 4-2. (a) The TEM images and (b) HRTEM image of P25 nanoparticles.....	42
Figure 4-3. The SEM images of (a) P25, (b) HBr-P25, (c) HCl-P25, (d) NaBr-P25 and (e) NaCl-P25. ....	43
Figure 4-4. The EDX spectra of (a) HBr-P25, (b) HCl-P25, (c) NaBr-P25 and (d) NaCl-P25.....	44
Figure 4-5. XRD patterns of different types of TiO <sub>2</sub> . (A: anatase phases, R: rutile phases).....	48
Figure 4-6. FTIR spectra of different types of TiO <sub>2</sub> . ....	48
Figure 4-7. Raman spectra of different types of TiO <sub>2</sub> .....	49
Figure 4-8. XPS full spectra (a), high-resolution XPS spectra of O1s (b) and Ti2p (c)	

for different TiO <sub>2</sub> . High-resolution XPS spectra of Br 3d (d) for HBr-P25 and NaBr-P25. ....	51
Figure 4-9. Aggregation kinetics of different concentrations of P25 in the solutions with 5 mg/L SMZ. ....	52
Figure 4-10. Aggregation kinetics of 10 mg/L P25 with different NaCl concentrations in 5 mg/L SMZ solutions. ....	54
Figure 4-11. Sedimentation kinetics of P25 with different NaCl concentrations in SMZ solutions (P25: 10 mg/L; SMZ: 5mg/L). ....	55
Figure 4-12. Aggregation kinetics of 10 mg/L P25 with different NaBr concentrations in 5 mg/L SMZ solutions. ....	55
Figure 4-13. Sedimentation kinetics of 10 mg/L P25 with different NaBr concentrations in 5 mg/L SMZ solutions. ....	56
Figure 4-14. Aggregation kinetics of 300 mg/L photocatalysts in 5 mg/L SMZ solutions. ....	56
Figure 4-15. Aggregation kinetics of 300 mg/L photocatalysts in 5 mg/L SMZ solutions. ....	57
Figure 4-16. Aggregation kinetics of 10 mg/L P25 at 2.5 and 5 mg/L LHA with or without 100 mM NaBr in 5 mg/L SMZ solutions. ....	58
Figure 4-17. Aggregation kinetics of 10 mg/L P25 at 2.5 and 5 mg/L SRHA with or without 100 mM NaBr in 5 mg/L SMZ solutions. ....	58
Figure 4-18. The photocatalytic degradation of SMZ by different concentrations of P25 under UV-C light. ....	60
Figure 4-19. The photocatalytic degradation of SMZ by different concentrations of P25 under UV-A light. ....	61
Figure 4-20. The photocatalytic degradation of different concentrations of SMZ by 10 mg/L P25 under UV light. ....	63
Figure 4-21. The photocatalytic degradation of 5 mg/L SMZ by 10 mg/L P25 at different NaCl concentrations under UV light. ....	65
Figure 4-22. The relationship between SMZ degradation rate constant and NaCl concentrations. ....	66
Figure 4-23. The relationship between SMZ degradation rate constant and P25 particle size in the presence of different concentrations of NaCl. ....	66
Figure 4-24. The photocatalytic degradation of 5 mg/L SMZ by 10 mg/L P25 at different NaBr concentrations under UV light. ....	69
Figure 4-25. The relationship between SMZ degradation rate constant and NaBr concentration with 5 mg/L SMZ and 10 mg/L P25. ....	70
Figure 4-26. The relationship between SMZ degradation rate constant and P25 particle size in the presence of different concentrations of NaBr. ....	70

Figure 4-27. The photocatalytic degradation of 5 mg/L SMZ by 10 mg/L P25 with NaBr at different pH under UV light. ....	73
Figure 4-28. The photocatalytic degradation of 5 mg/L SMZ by 10 mg/L P25 with NaBr at different pH under UV light. ....	74
Figure 4-29. The photocatalytic degradation of 5 mg/L SMZ by 0.3 g/L P25, HBr-P25 and HCl-P25 under UV light. ....	76
Figure 4-30. The photocatalytic degradation of 5 mg/L SMZ by 0.3 g/L P25, NaBr-P25 and NaCl-P25 under UV light. ....	77
Figure 4-31. The photocatalytic degradation of 5 mg/L SMZ by 10 mg/L P25 with 100 mM NaBr and LHA under UV light. ....	81
Figure 4-32. The photocatalytic degradation of 5 mg/L SMZ by 10 mg/L P25 with 100 mM NaBr and SRHA under UV light. ....	81
Figure 4-33. The photocatalytic degradation of 5 mg/L SMZ by 10 mg/L P25 with 100 mM scavengers (AA and t-buOH) under UV light. ....	84
Figure 4-34. The photocatalytic degradation of 5 mg/L SMZ by 10 mg/L P25 with 100 mM NaBr and 10 mM Na <sub>2</sub> C <sub>2</sub> O <sub>4</sub> (hole scavenger) under UV light. ....	86
Figure 4-35. The photocatalytic degradation of 5 mg/L SMZ by 10 mg/L P25 with 100 mM NaBr and Na <sub>2</sub> C <sub>2</sub> O <sub>4</sub> mixed with H <sub>2</sub> C <sub>2</sub> O <sub>4</sub> (as hole scavengers and the concentration of C <sub>2</sub> O <sub>4</sub> <sup>2-</sup> was fixed at 10 mM) under UV light. (UV light: $\lambda = 365$ nm, 32W) ....	87
Figure 4-36. The PL spectra of P25 and P25 with different concentration of NaBr (a), NaCl (b), and P25, HBr-P25 and HCl-P25 at 300 mg/L (c). ( $\lambda_{ex} = 350$ nm) ....	90
Figure 4-37. Time profiles of the generation of Fe <sup>3+</sup> -mediated photocurrent ( $I_{ph}$ ) in suspensions of P25 and P25 with different concentration of NaBr. ....	92
Figure 4-38. The dissolved and near-surface OH radicals measured by fluorescence probe molecule (a) coumarin and (b) coumarin-3-carboxylic acid (CCA), respectively. ....	95
Figure 4-39. The DPD results of P25 with different concentration of NaBr. ....	97
Figure 4-40. The DPD results of HBr-P25 and HCl-P25. ....	97
Figure 4-41. The result of dibromocyclohexane test by P25 with different concentrations of NaBr. ....	99
Figure 4-42. The result of dibromocyclohexane test by 300 mg/L P25 and HBr-P25. ....	100
Figure 4-43. The Br <sub>3</sub> <sup>-</sup> absorbance test ( $\lambda_{max} = 267$ nm) of 10 mg/L P25 with different concentration of NaBr under UV light irradiation. ....	101
Figure 4-44. The results of TBO test. ....	102
Figure 4-45. Transient absorption spectra of photoelectrons of TiO <sub>2</sub> and TiO <sub>2</sub> with 1 M NaBr. (a) TAS signals: 450 nm (b) TAS signals: 800 nm. ....	103
Figure 4-46. Mass spectra for byproducts of SMZ photocatalytic degradation by TiO <sub>2</sub>	

with 100 mM NaBr: (a) brominated SMZ and (b) dibrominated SMZ. ....	106
Figure 4-47. Mass spectra for byproducts of SMZ photocatalytic degradation by HBr-P25: (a) brominated SMZ and (b) dibrominated SMZ. ....	107
Figure 4-48. LC pattern of SMZ byproduct which was photodegraded by P25 NPs aggregates with 100 mM NaBr within 120 min.....	108
Figure 4-49. LC pattern of SMZ byproduct which was photodegraded by HBr-P25 within 30 min. ....	109

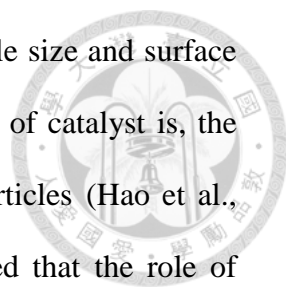
## Chapter 1 Introduction



Recently, the emergence of antibiotics and their residues in various aquatic systems has drawn wide attention due to their potential threat to both human health and aquatic ecosystems. As emerging persistent pollutants, though the concentration of antibiotics and their residues in the aquatic environment is usually low, ranging from  $\text{ng L}^{-1}$  to  $\mu\text{g L}^{-1}$ , they are believed to be able to raise antibiotic resistance in microorganisms in the long term. Sulfonamides are one of the most extensively used antibiotics in human and veterinary medicine, and large amount of sulfonamides finds their way into the environment every year. Among them, sulfamethoxazole (SMZ) is the most frequently detected, with concentrations as high as  $24.8 \mu\text{g L}^{-1}$  in wastewater treatment plant secondary effluent and  $940 \text{ ng L}^{-1}$  in surface water (Padhye et al., 2014). As a consequence, an intense research activity has been developed to find out efficient technologies aimed at removing SMZ from surface water and wastewater.

Photocatalytic oxidation is one of the advanced technologies employed for the elimination of gaseous and aqueous organic pollutants because of the efficiency in their mineralization and ideally producing final products as carbon dioxide, water, and inorganic ions. Widely used semiconductor photocatalyst,  $\text{TiO}_2$ , shows excellent UV-light photocatalytic activity and has been investigated extensively.  $\text{TiO}_2$  is attractive due to low cost, high stability, insoluble, safety, resistance to corrosion. Not only commercial but also self-synthesized  $\text{TiO}_2$  particles generally possess significant diversities in their crystal structure, particle size and photoelectrochemical characteristics, which plays a significant role in their photoactivity on organic pollutants. Particle size also plays an important role in nanocrystalline  $\text{TiO}_2$  based catalysts chiefly through affecting the electron-hole recombination. Previous studies





reported that the activity of the catalysts is dependent on its particle size and surface area. Most of them had a conclusion that the smaller particle size of catalyst is, the higher efficiency and activity it will be as compared to larger particles (Hao et al., 2002; Zhang et al., 1998). However, Wang et al. (2003) proposed that the role of interparticle charge transfers in agglomerated TiO<sub>2</sub> nanoparticles may increase the photocatalytic efficiency. Therefore, the connection between particle size and photoactivity of the aggregated nanoparticles needs to be investigated. On the other hand, ionic strength (IS) and pH also influence the photodegradation of organic compounds by TiO<sub>2</sub>. Moreover, natural organic matter (NOM) also affects the photocatalytic performance of TiO<sub>2</sub>. Besides, these parameters are also the main factors affecting particle size of TiO<sub>2</sub> in many studies. Consequently, it is necessary to investigate the effect of these environmental factors on the photocatalytic efficiency of SMZ by UV/TiO<sub>2</sub> process.

In this study, the photocatalytic degradation of SMZ in water under illumination of UVA light with one commercial TiO<sub>2</sub> (Degussa P25) was examined. We also investigated the effects of two kinds of halide salts (NaCl and NaBr) with different concentrations, pH and NOM on photodegradation of SMZ under UV irradiation by P25 aggregated NPs in suspension. To clarify where the effect of halide ions occurred, we synthesized some photocatalysts doped Br or Cl on the surface of P25. We also provided the results of photoluminescence of P25 with halide ions which may give an insight into the relation between electron-hole recombination and halide ions. On the other hand, in order to elucidate the relation between •OH and bromide ion in TiO<sub>2</sub> photocatalytic system, different kinds of scavengers were added to eliminate the photogenerated hole, surface-bound oxidants and dissolved oxidants. The DPD method was used to evaluate the concentration of reactive bromine species. The generation of Br<sub>2</sub> was confirmed by dibromocyclohexane and Br<sub>3</sub><sup>-</sup> tests. The

byproducts of SMZ during the photodegradation process were analyzed by HPLC-MS to further understand the photocatalytic degradation mechanism of SMZ. While TiO<sub>2</sub> NPs are spread into the environment, the transformation and halogenation of SMZ could occur in nature saline surface water under sunlight irradiation. These findings may have significant technical implications for optimizing the photochemical technologies in salt-rich wastewater treatment.

## Chapter 2 Literature Review



### 2.1 Introduction of sulfamethoxazole (SMZ)

#### 2.1.1 The environmental issue of sulfamethoxazole (SMZ)

Antibiotics have been widely used in prophylaxis and therapy of human and animal diseases and as promoters for animal growth. However, the pollution of antibiotics in environment is growing worse, which is mainly caused by the abuse and overuse of antibiotics due to the lack of scientific guidelines. Antibiotics residues in water and wastewater have brought potential threat to the environment, even in low concentrations, including antimicrobial resistance to microbes, disturbances and perturbations in ecosystems, and potential risks to human's health through drinking water and the food chain (Gao et al., 2014; Kim et al., 2015).

Sulfonamides, a large group of broad-spectrum antibiotics, have been extensively used since 1968. Their structures are characterized by a common sulfanilamide group and a distinct five- or six-member heterocyclic ring (denoted by R in the general structure). Sulfonamides are widely prescribed to treat human and animal infections. In bacteria, sulfonamides inhibit folic acid synthesis by competitive inhibition of the enzyme dihydropteroate synthetase (Zhang & Meshnick, 1991). Although previous studies demonstrated that sulfonamides are biodegraded in sewage, these processes are typically too slow to ensure complete elimination from treated wastewater effluent (Ingerslev & Halling-Sørensen, 2000; Pérez et al., 2005). As a result, detection of sulfonamides in aquatic environment has been reported by many researchers (Kummerer, 2009; Le-Minh et al., 2010; Sun et al., 2009). Among them, sulfamethoxazole (SMZ) was the most frequently detected, followed by sulfadiazine (SDZ) and sulfisoxazole (SSX). Due to its polarity and antibacterial nature, poor

removal of sulfamethoxazole was exhibited during conventional biological wastewater treatment (Gao et al., 2014; Gonzalez et al., 2007; Michael et al., 2013). SMZ has been repeatedly detected with concentrations as high as  $24.8 \mu\text{g L}^{-1}$  in wastewater treatment plant secondary effluent and  $940 \text{ ng L}^{-1}$  in surface water (Padhye et al., 2014). Previous studies also demonstrated that SMZ cannot be effectively eliminated during conventional drinking water treatment processes (coagulation, sedimentation and sand-filtration). Thus, an effective elimination of SMZ from surface water is very important for protecting human health and ecological safety.

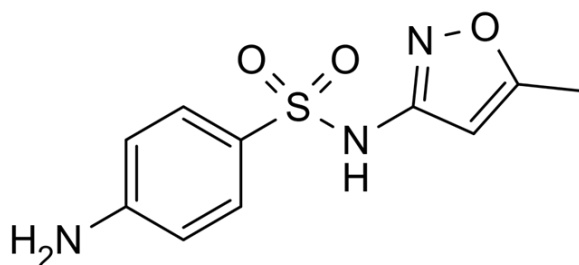


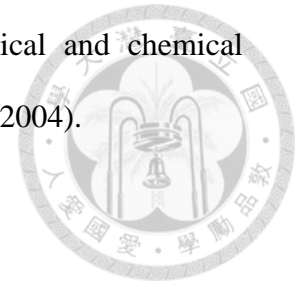
Figure 2-1. The chemical structure of sulfamethoxazole (SMZ).

### 2.1.2 The removal of SMZ by different methods

For better removal of sulfonamides, a lot of advanced water treatment methods have been investigated, such as membrane filtration (Koyuncu et al., 2008), ozonation, activated carbon adsorption, microbial degradation, electrolysis, photoelectrocatalysis (Su et al., 2016) and photocatalysis (Nasuhoglu et al., 2011; Song et al., 2017; Xekoukoulotakis et al., 2011). Among which, photocatalysis has recently received tremendous research attention because it's eco-friendly and efficient.

Photocatalysis, as one kind of advanced oxidation process (AOP) which has merits of almost completed degradation and easy to operate, is a green technology to treat the antibiotic wastewater. Various photocatalysts including CdS, SnO<sub>2</sub>, WO<sub>3</sub>, SiO<sub>2</sub>, ZnO, Nb<sub>2</sub>O<sub>3</sub>, Fe<sub>2</sub>O<sub>3</sub> have been studied, and TiO<sub>2</sub> is the most well-known and

promising among them for its high efficiency, low cost, physical and chemical stability, widespread availability, and noncorrosive property (Carp, 2004).



## **2.2 Introduction of titanium dioxide (TiO<sub>2</sub>)**

### **2.2.1 The titanium dioxide (TiO<sub>2</sub>)**

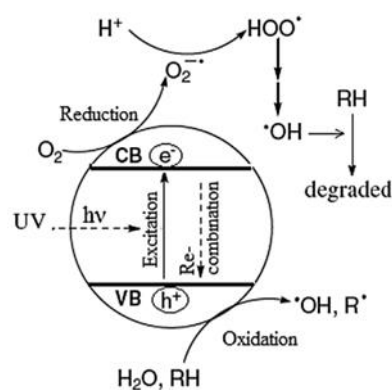
TiO<sub>2</sub> has attracted great interest in a variety of applications, including water splitting, hydrogen evolution and pollutant degradation (Nakata & Fujishima, 2012). The photocatalytic activity of TiO<sub>2</sub> has been shown to strongly rely on its phase structure, crystallite size, morphological characteristic, surface area and pore structure. TiO<sub>2</sub> has three main crystal structures, rutile, anatase, and brookite. Anatase is the most utilized given its abundance and ease of synthesis compared to brookite and its improved photocatalytic ability compared to rutile. Even though rutile has a band gap of 3.0 eV and anatase has a larger band gap of 3.2 eV, the former presents lower photocatalytic performance due to faster electron-hole pair recombination. Several papers have shown that the mixed phase-TiO<sub>2</sub>, especially P25, which contains ~70% anatase and ~30% rutile, has photocatalytic properties that exceed either pure phase (Hurum et al., 2003).

### **2.2.2 The principle of photocatalytic degradation**

Upon irradiation of TiO<sub>2</sub> with light energy equivalent to or greater than its band gap energy, electrons are excited from the valence band (VB) to the conduction band (CB), leaving the energized holes in VB ( $h^+_{VB}$ ) (reactions 2-1) (Fujishima et al., 2000). The electron and hole can migrate to the surface of TiO<sub>2</sub>, where they are trapped by surface titanol groups (reactions 2-2 & 2-3). However, in competition with the rapid migration, the recombination of electron-hole pair may happen. This can occur either in the volume or at the surface of TiO<sub>2</sub>, releasing input energy as heat and diminishing

the photocatalytic activity (reactions 2-4~2-6) (Ferguson et al., 2005). Before any chemistry begins, the photonic energy has decayed considerably to the point where only about 4% (the quantum yield) of active species are available at the surface to generate redox chemistry (Serpone, 1995).

The excited electrons in CB ( $e^-_{CB}$ ) are trapped at  $Ti^{IV}$  sites to give  $Ti^{III}$  centers, reducing oxygen to form superoxide radical anions ( $\bullet O_2^-$ ) (reactions 2-7), which may self-react via disproportionation (reaction 2-14) into  $H_2O_2$  and  $O_2$ , or be further reduced to yield  $H_2O_2$  (reactions 2-8). Afterwards,  $e^-_{CB}$  and  $\bullet O_2^-$  can react with  $H_2O_2$  to produce hydroxyl radicals ( $\bullet OH$ ) (reactions 2-9 & 2-10). Meanwhile, the trapped  $h^+_{VB}$  oxidizes the adsorbed water ( $H_2O$ ) or surface-bound hydroxyl ion ( $OH^-$ ) to yield the surface-bound  $\bullet OH$  radical (reactions 2-11 & 2-12). Target compounds can be oxidized by  $\bullet O_2^-$ ,  $\bullet OH$  and  $h^+_{VB}$  to form byproducts, which can be further oxidized to  $CO_2$  and  $H_2O$ . Scheme 2-1 (Dong et al., 2015) depicts the mechanism of the electron-hole pair formation when  $TiO_2$  is irradiated with light of adequate energy. The light wavelength for such photon energy usually corresponds to  $\lambda < 400$  nm (UV-A region).



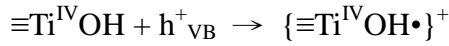
Scheme 2-1. Schematic diagram illustrates the principle of  $TiO_2$  photocatalysis with the presence of water pollutant (RH) (Dong et al., 2015).



### Charge separation



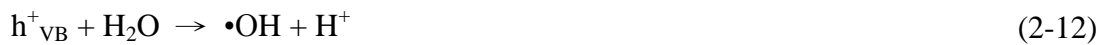
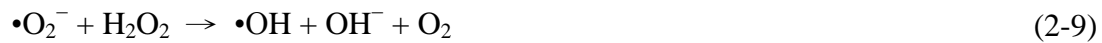
### Surface trapping



### Recombination



### Interfacial charge transfer: reactive oxygen species



### $\cdot\text{O}_2^-$ disproportionation



In addition,  $\text{TiO}_2$  surfaces become superhydrophilic with a contact angle of less than  $5^\circ$  under UV light irradiation (Wang et al., 1997). The superhydrophilicity is originated from chemical conformation changes of the surface. The majority of the holes are subsequently consumed by reacting directly with adsorbed organic species or adsorbed water, producing  $\cdot\text{OH}$  radicals as described above. However, a small proportion of the holes is trapped at lattice oxygen sites and may react with  $\text{TiO}_2$  itself,

which weakens the bonds between the lattice titanium and oxygen ions. Water molecules can then interrupt these bonds, forming new hydroxyl groups (Figure 2-2) (Fujishima et al., 2000; Nakata & Fujishima, 2012). The singly coordinated OH groups produced by UV light irradiation are thermodynamically less stable and have high surface energy, which results in the formation of a superhydrophilic surface.

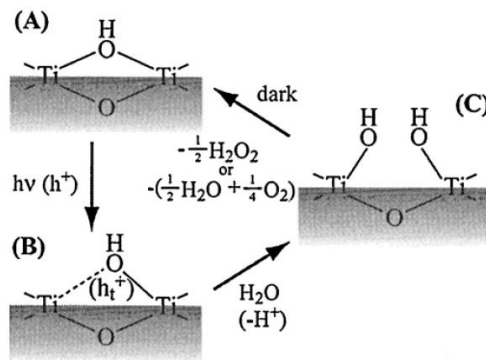
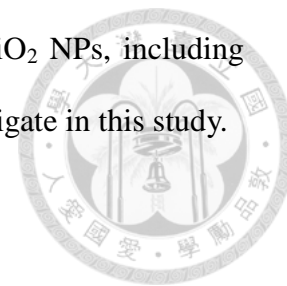


Figure 2-2. Mechanism of photoinduced hydrophilicity (Fujishima et al., 2000).

The widespread use of TiO<sub>2</sub> is to some extent limited by its wide band gap, which requires UV irradiation for photocatalytic activation, giving rise to a very low energy efficiency in utilizing solar light (Shu et al., 2003). Because UV light accounts for only a small fraction (5%) of the sun's energy compared to visible light (45%), the shift in the optical response of TiO<sub>2</sub> from UV to visible light spectral range will have a profound improvement on the practical applications. Besides the inefficient irradiation of visible light, the practical applications are also constrained due to the following limitations: (1) low adsorption capacity to hydrophobic contaminants; (2) high aggregation tendency; and (3) difficulty of separation and recovery. Moreover, in natural water systems, TiO<sub>2</sub> may be subject to the deactivation by the presence of inorganic ions (Wang et al., 2000), such as halide anions. Ions and pH affect the aggregation, sedimentation and dissolution of TiO<sub>2</sub>. Natural organic matter (NOM), in natural water system, also has influence on the photodegradation efficiency of TiO<sub>2</sub>



NPs. Various parameters affect the photocatalytic properties of TiO<sub>2</sub> NPs, including particle size, surface area, ions, pH and NOM, which will be investigated in this study.

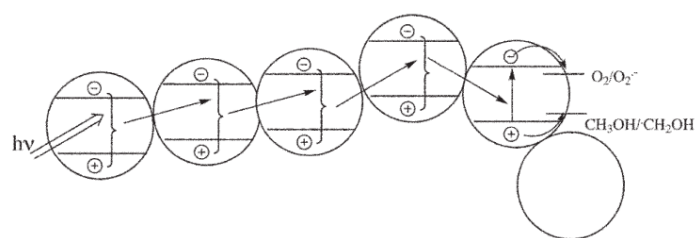


### 2.2.2.1 Effect of particle size

It is generally considered that a good photocatalyst must have high photon conversion efficiency in addition to high specific surface area. In fact, the particle size of photocatalysts determines both the specific surface area and the photon conversion efficiency. Therefore, the particle size can affect the photocatalytic reactivity (Lin et al., 2006). Smaller particles with larger surface area are likely to result in better photocatalytic activity because it provides more active sites. Zhang et al. (1998) reported that TiO<sub>2</sub> particles at 11 nm presented the highest photocatalytic activity on the oxidation of CHCl<sub>3</sub>. Jang et al. (2001) also presented that a higher degree of decomposition of methylene blue by the TiO<sub>2</sub> nanoparticles was observed as the particle size decreased and as the mass fraction of anatase increased. Hao et al. (2002) compared different sizes of TiO<sub>2</sub> particles in the photodegradation of rhodanide B, indicating that the smaller the size of the catalyst, the higher the efficiency and activity as compared with the larger particles. Maira et al. (2000) found the smaller crystals of TiO<sub>2</sub> offer a larger surface area and exhibit higher trichloroethene (TCE) degradation efficiency.

However, some photocatalytic reactions could be accelerated by large TiO<sub>2</sub> particles. Wang et al. (2003) proposed a novel mechanism based on the observation that three-dimensional TiO<sub>2</sub> networks indeed exist in aqueous suspensions. The novel energy transfer mechanism, which is called “antenna mechanism”, is defined as the energetic coupling throughout a long chain of TiO<sub>2</sub> nanoparticles that enables energy or charge-carrier transfer from a particle where the initial photon absorption takes place to another particle where the charge transfer finally occurs. The

three-dimensional networks can act as antenna systems that improve photocatalytic activities of aggregated nanoparticles. As shown in Scheme 2-2, even if the target molecule is adsorbed on a photocatalyst particle at a certain distance from the light-absorbing particle, the latter can transfer the energy from particle to particle provided these particles are aggregated and possess the same crystallographic orientation. Once the energy has reached the particle with the adsorbed target molecule like methanol, the latter will act as a hole trap thus inducing the separation of the original exciton. Thus, a long chain of TiO<sub>2</sub>-particles aligned as shown in Scheme 2-2 will act as an antenna system transferring the photon energy from the location of absorption to the location of reaction. The physical and energetic interconnection among TiO<sub>2</sub> nanoparticles ensures an enhanced charge separation and a reduced recombination, which increases the charge carrier diffusion length.



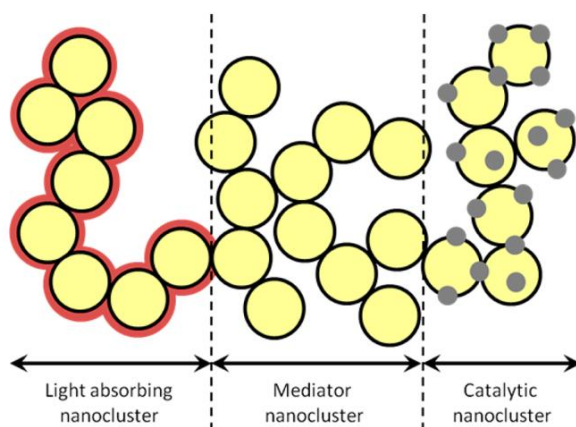
Scheme 2-2. Increased photocatalytic activity through energy/exciton transfer in aggregated photocatalyst particles (antenna effect) (Wang et al., 2003).

This mechanism has been repeatedly invoked in the literature for justifying the observed results, such as the oxidation of methanol with mesoporous Au-TiO<sub>2</sub> (Ismail, Bahnemann, Bannat, et al., 2009) and Pd-TiO<sub>2</sub> (Ismail & Bahnemann, 2011), the hydrogen production by TiO<sub>2</sub> (Lakshminarasimhan et al., 2008) and the degradation of dichloroacetic acid (DCA) with Pt-TiO<sub>2</sub> (Ismail, Bahnemann, Robben, et al., 2009).

Despite the numerous antenna phenomena evidence, the mechanism itself has not been appropriately tested. Park et al. (2013) investigated the interparticle charge

transfer in the agglomerates of NPs, and found that the presence of bare  $\text{TiO}_2$  as a mediator that connects Dye/ $\text{TiO}_2$  and Pt/ $\text{TiO}_2$  NPs markedly enhanced the dye-sensitized production of hydrogen by facilitating the charge separation through multiple grain boundaries within the agglomerates (Scheme 2-3). The charge recombination between the oxidized dye and the injected electron was retarded when  $\text{TiO}_2$  NPs were additionally included within the aggregates. As a result, the photoexcitation site and the photocatalytic site can be spatially remote.

Antenna effect provides different aspect of the influence resulting from the particle size on the photocatalytic degradation. Therefore, it is essential to investigate the effect of particle size on the photodegradation performance of SMZ.



Scheme 2-3. Illustration of  $\text{TiO}_2$  Nanoparticles Aggregate Assembly Employed for the Dye-Sensitized Production of  $\text{H}_2$  (Park et al., 2013).

#### 2.2.2.2 Effect of pH

Both acidic (Ramjaun et al., 2011; Zhang et al., 2011) and alkaline (Jia et al., 2012) conditions have been reported to improve degradation efficiencies of different organic compounds. The pH is an important factor in the photocatalytic reactions as it influences surface charge and agglomeration of catalyst suspension, speciation of organic compounds, and degradation pathway. (Šojić et al., 2009; Su et al., 2016).

SMZ, the target organic compound in this study, contains one basic amine group ( $-NH_2$ ) and one acidic amide group ( $-NH-$ ) and therefore it has two  $pK_a$  values, namely  $pK_{a1} = 1.83$  and  $pK_{a2} = 5.57$ . The acid-base dissociation equilibrium of SMZ is illustrated in Figure 2-3. As shown in Figure 2-3,  $K_{a1}$  is the dissociation constant for the equilibrium between the positively charged, protonated amino group of SMZ and its electrically neutral conjugate base, while  $K_{a2}$  refers to the equilibrium involving the loss of the sulfonamide proton to yield its negatively charged conjugate base (Dodd & Huang, 2004; Lin et al., 1997). Therefore, at pH values below  $pK_{a1}$  and above  $pK_{a2}$  the positively and negatively charged forms of SMZ prevail, respectively, while at pH values between  $pK_{a1}$  and  $pK_{a2}$  SMZ exists predominately in its neutral form.

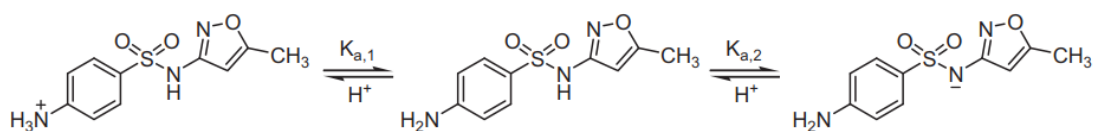
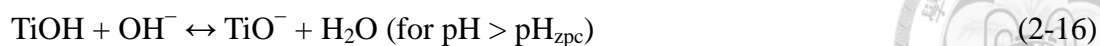


Figure 2-3. Acid–base dissociation equilibrium of SMZ (Xekoukoulotakis et al., 2011).

Due to amphoteric behavior of  $TiO_2$  nanoparticles suspended in aqueous solution, the effect of solution pH on degradation rate of the compound depends on the acid-base properties of the particle surface and can be explained on the basis of the point of zero charge ( $pH_{zpc}$ ) (Sin et al., 2012).  $TiO_2$  has a  $pH_{zpc}$  between 5.6 and 6.8 (Kosmulski, 2011). When the pH is lower than its  $pH_{zpc}$ , the  $TiO_2$  surface gets a positive charge due to protonation, which is conducive for  $e^-_{cb}$  to transfer to the  $TiO_2$  surface. When the pH is higher than its  $pH_{zpc}$ , the surface of  $TiO_2$  is negatively charged, which is conducive for  $h^+_{vb}$  to move to  $TiO_2$  surface. In other words, the highest photocatalytic reaction rate could occur in the solution with lower or higher pH that inhibits  $e^-_{cb}$  and  $h^+_{vb}$  from recombination (Jia et al., 2012).



For some organic compounds, the acidic conditions were favorable for the photocatalytic degradation reaction. As for the photodegradation of phenol with immobilized  $\text{TiO}_2$ , the rate constant was low in the basic region of pH 10; however, it increased in the acidic region of pH 3. Lee et al. (2004) suggested that the concentration of  $\bullet\text{OH}$  increases as the concentration of  $\text{H}^+$  increases:



$$K_e \text{ (equilibrium constant)} = [\bullet\text{OH}]^3 / ([\bullet\text{OH}][\text{H}^+]^2[\bullet\text{O}_2^-]) \quad (2-18)$$

$$[\text{OH}^-][\text{H}^+] = K_w = 1 \times 10^{-14} \quad (2-19)$$

$$[\bullet\text{OH}]^3 = K_e K_w [\text{H}^+][\bullet\text{O}_2^-] \quad (2-20)$$

Xekoukoulotakis et al. (2011) reported that the photodegradation of 10 mg/L SMZ by 500 mg/L P25 was faster at around pH 4 than at around pH 7.5 in ultra-pure water under UV-A light irradiation. Su et al. (2016) also indicated that enhanced photoelectrocatalytic degradation rate of SMZ by  $\text{TiO}_2/\text{Ti}$  photoanode at acidic pH may be due to a greater adsorption of SMZ at the  $\text{TiO}_2$  surface. In general, the influence of pH and salt depends on the nature of the molecules (Yuan et al., 2012).

On the other hand, several studies demonstrated that alkaline conditions were favorable for the photocatalytic degradation of phenol and phenol removal efficiency, and the photocatalysis kinetics increased with increasing initial pH (Jia et al., 2012). At alkaline pH, phenol is not well adsorbed and has less chance to react with the photogenerated holes. In this case, phenol is more favorable to react through the homogeneous pathway, i.e. to react with the diffused hydroxyl radicals. The study of Chiang et al. (2004) showed that for other organic compounds, at higher  $\text{OH}^-$  concentrations, a significant increase of the reaction rate of clopyralid was observed, which can be explained by the increased  $\bullet\text{OH}$  production due to a higher

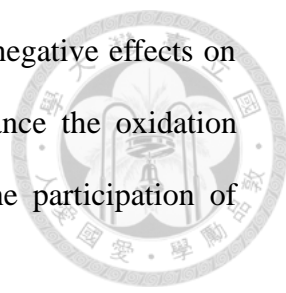
concentration of  $\text{OH}^-$  ions in the solution (Marotta et al., 2012; Šojić et al., 2009). From studies above, it can be concluded that solution pH plays a significant role in controlling of photocatalytic degradation mechanisms of organic compounds.



### 2.2.2.3 Effect of halide ions

Majority of the literatures illustrated that the ions in wastewater such as chloride, nitrate and sulfate could depress the photocatalytic activity due to their compete effect against  $\bullet\text{OH}$  for  $h^+_{\text{vb}}$ . Inorganic halides including fluoride, chloride, bromide, and iodide are ubiquitous in natural water, and their influences on photolysis may be associated with several contrasting mechanisms, such as radical formation, radical inhibition, and product effect (i.e., thermodynamically a phenomenon in which a product inhibits a forward reaction). As for the effect of  $\text{Cl}^-$ , studies among others by Caregnato et al. (2013) on the effect of  $\text{Cl}^-$  on AOP and by Yang et al. (2005) on the involvement of  $\text{Cl}^-$  in the photocatalytic process showed that  $\text{Cl}^-$  presented in polluted waters under certain conditions are able to scavenge active radicals and slow down the photodegradation rate. The results from Liang et al. (2008) indicated that the rate of 2,3-DCP photodegradation by  $\text{TiO}_2$  nanotube arrays decreased with an increased  $\text{Cl}^-$  concentration significantly, which could be attributed to the competitive adsorption and the formation of less reactive radicals during the photocatalytic reaction. Previous studies also elucidated that the presence of  $\text{Br}^-$  could inhibit the photodegradation of organic compounds. Luca et al. (2017) indicated that the competition of  $\text{Br}^-$  for the radicals, like  $\bullet\text{OH}$  and  $\bullet\text{SO}_4^-$  led to a reduced benzophenone-4 (BZA) removal effectiveness in the UV/persulfate/ $\text{Fe}^{2+}$  system. Bu et al. (2018) also showed that adding bromide into the system apparently decreased the degradation rates of monochloroacetic acid (MCAA). According to the study by Li et al. (2017), bromide ion had significant inhibitory effects against ibuprofen

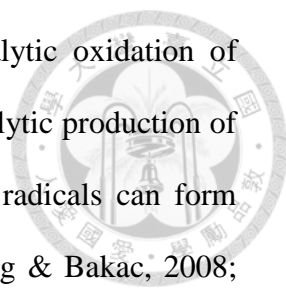
photodegradation. However, whether halide ions have positive or negative effects on the photoreaction still remains controversial. Chloride may enhance the oxidation process under conditions of high anions concentration due to the participation of chloride radicals.



Iguchi et al. (2015) reported the applications of  $\text{Cl}^-$  in photocatalytic systems being used to scavenge  $h^+_{\text{vb}}$  and improve performance. The addition of NaCl to their system enhanced photodegradation significantly, and it was also noted that other chloride salts such as KCl, CsCl,  $\text{MgCl}_2$  and  $\text{CaCl}_2$  imparted positive influence. Another study by Krivec et al. (2014) reported that  $\text{Cl}^-$  that are formed as by-products in the photocatalytic process can react with photogenerated holes and influence oxidation. Khuzwayo et al. (2017) reported that the exclusive presence of halides in the absence of an electron acceptor adequately facilitated the photo-oxidation process of PCP below critical levels of anion concentration ( $20 \text{ mg L}^{-1}$  NaCl, NaBr and NaF), where beyond the critical point the process was significantly hindered. As for  $\text{Br}^-$ , Jia et al. (2015) reported synergetic effect enhanced photoelectrocatalysis, in which  $\text{Fe}^{3+}$  and  $\text{Br}^-$  were used as the acceptors of photogenerated charges on  $\text{TiO}_2$  nanoparticles. During the reaction,  $\text{Br}_2$  was generated as  $\text{Br}^-$  reacted with  $h^+_{\text{vb}}$ .



Antimicrobial  $\text{TiO}_2$  photocatalysis can be significantly potentiated by addition of non-toxic halide salts (Li et al., 2011). It is well known that halogen radicals are

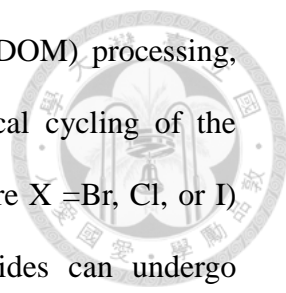


effective bactericides and can be readily produced by photocatalytic oxidation of halide ions at illuminated TiO<sub>2</sub> (Selcuk et al., 2006). The photocatalytic production of high concentration of halogen radicals is possible because these radicals can form stable di-halide radical anions ( $\bullet X_2^-$ ) in the presence of  $X^-$  (Cheng & Bakac, 2008; Merenyi & Lind, 1994). Since the effectiveness of a bactericide is highly dependent on its killing mechanisms, the bactericidal efficiency may be benefited from the different killing mechanisms offered by halide radicals. Wu et al. (2016) reported that the addition of NaBr to photoactivated TiO<sub>2</sub> (P25) potentiates the killing of Gram-positive, Gram-negative bacteria and fungi by up to three logs due to due to generation of both short and long-lived oxidized bromine species including hypobromite. Ng et al. (2016) also observed that at a high bromide concentration (65 mg/L, equivalent to the concentration of natural sea water), the bacterial inactivation rate increased 2 times at pH 5 and more than 5 times at pH 8 in TiO<sub>2</sub>-UVA system. Moreover, the bacterial inactivation pattern was shifted from the “shoulder-log” to the “log-tail” under different bromide concentrations, suggesting the existence of bromide altered the bacterial inactivation mechanisms.

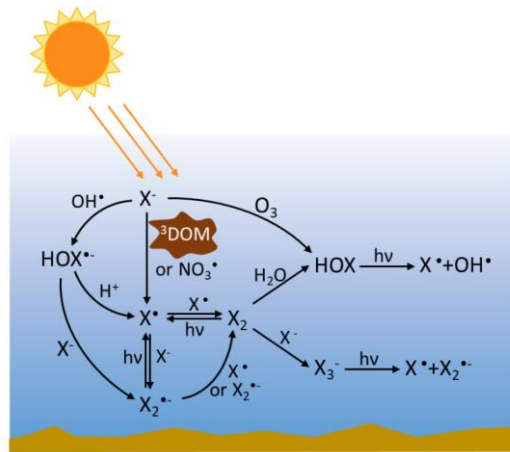
### **2.3 Introduction of reactive halogen species (RHS)**

Halide ions are ubiquitous in natural waters. Ordinary levels of halides in seawater are 540 mM chloride, 0.8 mM bromide, and 100–200 nM iodide (Grebel et al., 2010; Luther et al., 1988). Halide levels range downward in estuaries and upward in saltier water bodies relative to typical seawater levels. Surface fresh water and groundwater may contain up to 21 mM chloride and 0.05 mM bromide (Grebel et al., 2010), with higher levels in some places. Even though the halides themselves do not absorb light in the solar region, in nature they provide far more than just background electrolytes—they participate in a rich, aqueous-phase chemistry initiated by sunlight





that has many implications for dissolved natural organic matter (DOM) processing, fate and toxicity of organic pollutants, and global biogeochemical cycling of the halogens. Gaseous and aqueous reactive halogen species ( $X^*$ , where  $X = \text{Br}, \text{Cl}, \text{or I}$ ) play important roles in the chemistry of marine regions. Halides can undergo sensitized photolysis and react with many secondary photoproducts to produce reactive halogen species (RHS) ( $X^*_{(aq)} = \bullet X, \bullet X_2^-, X_2$  and HOX), as shown in Scheme 2-4, that can participate in a variety of reactions with DOM and anthropogenic compounds, including oxidation and incorporation of halogen. A number of important reactions that take place on snow, ice, and solid microparticles actually occur on or within a surface liquid layer that is often rich in salts (Pratt et al., 2013). It has also been suggested that the photo-oxidation of halides can lead to the abiotic formation of halogenated organic compounds in seawater and in polar snowpacks (Pratt et al., 2013). Research on the photochemical transformation of organic compounds in seawater has focused on freshwater-relevant pathways, including direct photolysis and dissolved organic matter (DOM)-sensitized indirect photodegradation by triplet-excited DOM ( ${}^3\text{DOM}^*$ ) or reactive oxygen species (e.g.,  $\bullet\text{OH}$ ,  $\bullet\text{O}_2^-$  and  $\bullet\text{OOH}$ ). Glover and Rosario-Ortiz (2013) elucidated that halide ions increased the steady state concentration of  ${}^3\text{DOM}^*$  by enhancing the inter-system crossing of DOM from the singlet state to the triplet state. Parker et al. (2013) found that halide ions decreased the quenching rate of  ${}^3\text{DOM}^*$ , which led to an increase of steady state concentration of  ${}^3\text{DOM}^*$ . The underlying mechanisms for the effects of halide ions on the photochemical processes are intricate, which needs to be further clarified. Therefore, it is important to understand the reactions that form RHS.



Scheme 2-4. Generation of RHS in waters through the action of sunlight (Yang & Pignatello, 2017).

### 2.3.1 The formation of halogen molecules from TiO<sub>2</sub> powder

Reichman et al. (1981) used pure TiO<sub>2</sub> and platinized semiconducting n-TiO<sub>2</sub> powder to produce halogen molecules, Cl<sub>2</sub>, Br<sub>2</sub>, and I<sub>2</sub> in oxygen-saturated aqueous solutions containing the respective halide ion under UV irradiation. Their results showed several points: (a) Halogen can be produced by irradiating solutions containing pure TiO<sub>2</sub> powder catalyst, but the production rates are greatly enhanced by using the platinized TiO<sub>2</sub> powder. (b) The rate of halogen production is in the order I<sub>2</sub> > Br<sub>2</sub> > Cl<sub>2</sub>. (c) The production rate of the halogens is dependent on the solution pH. The chemical reactions of halogen molecules are expressed in eq. 2-28 ~ 2-30. The half-reactions assumed are



at the illuminated TiO<sub>2</sub> site, and



at the platinized site, giving the overall reaction:



### 2.3.2 The formation of RHS from hydroxyl radicals

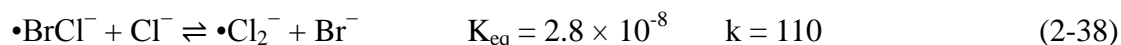
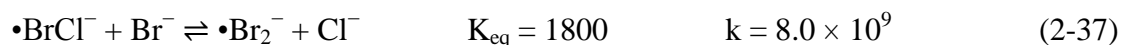
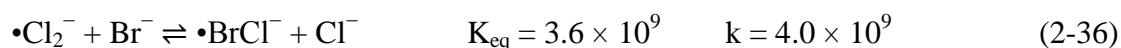
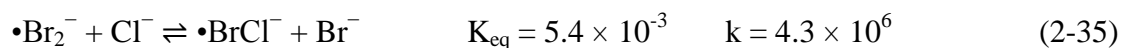
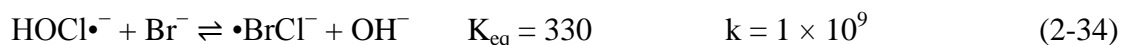
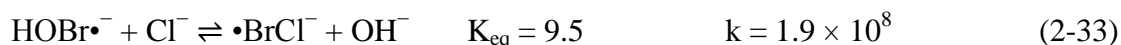
Regarding  $\bullet\text{OH}$  processing of marine DOM, it is recognized that halide ions ( $[\text{Cl}^-] \sim 0.54 \text{ M}$ ,  $[\text{Br}^-] \sim 0.8 \text{ mM}$ ), especially  $\text{Br}^-$ , are the most important  $\bullet\text{OH}$  scavengers in seawater, scavenging as much as  $\sim 93\%$  of  $\bullet\text{OH}$  (reaction 31) (Zafiriou, 1974; Zhou & Mopper, 1990).



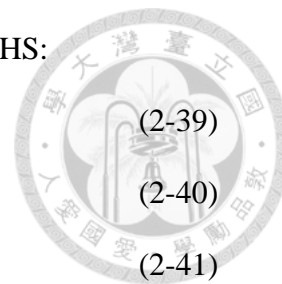
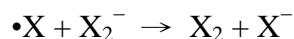
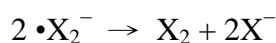
Previous studies indicated that halide ions can react with  $\bullet\text{OH}$  producing halogen radicals, like  $\bullet\text{Br}$ , leading to the formation of halogenated products (Grebel et al., 2010). Reactions of  $\bullet\text{OH}$  with halide ions ( $\text{X}^-$ ) form RHS that include radical RHS ( $\bullet\text{X}$  and  $\bullet\text{X}_2^-$ ) and non-radical RHS ( $\text{HOX}$ ,  $\text{X}_2$ ,  $\text{X}_3^-$ ) produced as termination products of radical RHS (Anastasio & Matthew, 2006; B. Matthew & C. Anastasio, 2006). Halogen atoms react rapidly and reversibly with halide ion to form the dihalogen radical anion:



Interconversion of halogen is possible among the reactive RHS. Some pertinent reactions and their equilibrium constants ( $K_{\text{eq}}$ ) and rate constants ( $k$ ) are given in Reactions 2-33 to 2-38:



Radical RHS dimerize or disproportionate to give the non-radical RHS:



Hydroxyl radicals react with halides via the adduct  $HOX\bullet^-$  to form the corresponding halogen and dihalogen radicals:



Reactions 2-42~2-44 are fast, reversible, and dependent on  $[X^-]$  and  $[H^+]$  (G. Jayson et al., 1973). Reactions with bromide and iodide lie far to the right at any normal environmental pH, while the oxidation of chloride to  $\bullet Cl$  and  $\bullet Cl_2^-$  is favorable only under acidic conditions and comparatively high halide concentrations. For example, at pH 3, oxidation of chloride is significant whenever  $[Cl^-]$  is much above a few millimolar (Pignatello, 1992). However, oxidation of chloride can be important in aerosols, where the pH can be as low as 2. Bromide and iodide are important  $\bullet OH$  scavengers in seawater (Mopper & Zhou, 1990). Scavenging of  $\bullet OH$  does not necessarily protect other solute molecules from oxidation, as the resulting RHS are themselves strong oxidants, albeit more selective.

The order of reactivity can be easily juxtaposed with the reduction potentials of one-electron inorganic couples which are listed below (Isse et al., 2010):

Table 2-1. Reduction potentials of one-electron inorganic couples (Isse et al., 2010).

Inorganic couples	Reduction potentials (V)
$\bullet\text{OH} / \text{OH}^-$	2.31
$\bullet\text{F} / \text{F}^-$	3.66
$\bullet\text{Cl} / \text{Cl}^-$	2.59
$\bullet\text{Br} / \text{Br}^-$	2.04
$\bullet\text{I} / \text{I}^-$	1.37

### 2.3.3 Photocatalytic transformation of organic compounds with halide ions

Previous studies showed that halide ions were important participants in photocatalytic transformation of organic compounds, leading to the formation of halogenated byproducts. Understanding the halogenation mechanisms of organic pollutants is helpful for the risk assessment of halogenated compounds due to their higher toxicity than parent compounds (Grebel et al., 2010; Liu et al., 2009). Liu et al. (2009) observed the formation of chlorinated intermediates in surface saline water mostly due to the formation of  $\bullet\text{Cl}_2^-$  radical as a consequence of Fe (III) irradiation. Triplet-excited state is an important reactive intermediate in the photo-transformation of organic pollutants due to its longer life than that of singlet-excited state (Klán & Wirz, 2009). Jammoul et al. (2009) reported that the triplet-excited state of benzophenone, as a proxy for an aromatic carbonyl compound in the natural sea surface microlayer, could oxidize halide ions to produce halogen radicals. Méndez-Díaz et al. (2014) found that reactions of DOM with photochemically generated RHS may represent an important abiotic natural source of organobromine and organoiodine in seawater. Calza et al. (2008, 2012) observed that photoinduced RHS can react with phenols leading to the halogenation of phenols in seawater. Li et

al. (2016) also reported that triplet excited sulfamethazine oxidized halide ions and triggered the halogenation of sulfamethazine, which was confirmed by the characterization of chlorinated and brominated intermediates.

The previous study has shown that in photoelectrochemical system, bromide ion would be oxidized by photogenerated hole of TiO<sub>2</sub> and produced bromine (reaction 2-47). Furthermore, the tribromide ion (Br<sub>3</sub><sup>-</sup>) may produce from the combination with bromine and bromide ion or the hole oxidation of bromide ion (reaction 2-48 and 2-49). At pH ≥ 9, Br<sub>3</sub><sup>-</sup> was not found in the solution, but a small amount of BrO<sup>-</sup> could be detected at pH 9 (reaction 2-50 and 2-51). Other aqueous phase reactions of bromine species are listed in Table 2-2.



## 2.4 Introduction of natural organic matter (NOM)

Natural organic matter (NOM) consists of a heterogeneous mixture of humic substances, hydrophilic acids, proteins, lipids, carbohydrates, carboxylic acids, amino acids and hydrocarbons (Westerhoff et al., 2004). In NOM, 50% of dissolved organic carbon is consisted of humic substances which are a complex of various functional groups roughly divided two parts: carboxylic groups and phenolic groups. Based on the different ratio of these two functional groups, humic substances can be classified to three types: humin (not dissolved in weak acid and base), humic acid (not dissolved in weak acid, but dissolved in weak base), and fulvic acid (dissolved in weak acid, but

not dissolved in weak base). Humic acid contains more phenolic groups compared to fulvic acid, and its molecule weight is also larger than fulvic acid. On the other hand, fulvic acid has more carboxylic group, and its solubility is higher than humic acid. The different ratio of carboxylic and phenolic groups affects the behavior and fate of the humic substances.

In natural waters, NOM can act as a scavenger of reactive halogen species, including HOBr and HOCl (Westerhoff et al., 2004). Because different components of NOM may exhibit different reactivity with oxidants, it is necessary to better understand the reaction of these NOM components with aqueous chlorine and bromine. The literature lacks sufficient direct comparisons between bromine versus chlorine reactivity with NOM. While it is generally accepted that bromine reacts faster than chlorine with NOM, little direct evidence of these reactions exist. For example, hypobromite was found to be a more complete oxidant and a faster substituting agent than hypochlorite with resorcinol and its derivatives (Rook et al., 1978). Most of the literature available on the formation mechanisms of halogenated compounds was developed by adding chlorine to waters in the presence of  $\text{Br}^-$  (Nokes et al., 1999). Further investigation on the respective reactivity of NOM with aqueous bromine separate from aqueous chlorine is needed to better understand individual reaction mechanisms.

Table 2-2. Aqueous phase bromine reactions (B. M. Matthew &amp; C. Anastasio, 2006).

Rxn #	Reaction	Rate constant (M <sup>-1</sup> s <sup>-1</sup> or s <sup>-1</sup> )	Reference
1	$\text{Br}^- + \bullet\text{OH} \rightarrow \bullet\text{BrOH}^-$	$1.1 \times 10^{10}$	Ross et al. (1998)
2	$\text{Br}^- + \bullet\text{BrOH}^- \rightarrow \bullet\text{Br}_2^- + \text{OH}^-$	$1.9 \times 10^8$	Zehavi & Rabani (1972)
3	$\text{Br}^- + \bullet\text{Br} \rightarrow \bullet\text{Br}_2^-$	$1.5 \times 10^{10}$	Ross et al. (1998)
4	$\text{Br}^- + \text{Br}_2 \rightarrow \text{Br}_3^-$	$9.6 \times 10^8$	Ershov (2004)
5	$\text{Br}^- + \text{HOBr} \rightarrow \text{Br}_2\text{OH}^-$	$5 \times 10^9$	Eigen & Kustin (1962)
6	$\bullet\text{BrOH}^- + \text{H}^+ \rightarrow \bullet\text{Br} + \text{H}_2\text{O}$	$4.4 \times 10^{10}$	Zehavi & Rabani (1972)
7	$\bullet\text{Br} + \text{H}_2\text{O}_2 \rightarrow \text{HBr} + \text{HO}_2\bullet$	$4 \times 10^9$	Sutton et al. (1965)
8	$\bullet\text{Br} + \text{OH}^- \rightarrow \bullet\text{BrOH}^-$	$1.3 \times 10^{10}$	Ross et al. (1998)
9	$\bullet\text{Br} + \bullet\text{Br} \rightarrow \text{Br}_2$	$1 \times 10^9$	Kläning & Wolff (1985)
10	$\bullet\text{Br} + \text{HO}_2\bullet \rightarrow \text{HBr} + \text{O}_2$	$1.6 \times 10^8$	Ross et al. (1998)
11	$\bullet\text{Br}_2^- + \text{HO}_2\bullet \rightarrow \text{Br}_2 + \text{HO}_2^-$	$4.4 \times 10^9$	Matthew et al. (2003)
12	$\bullet\text{Br}_2^- + \bullet\text{OH} \rightarrow \text{HOBr} + \text{Br}^-$	$1 \times 10^9$	Wagner & Strehlow (1987)
13	$\bullet\text{Br}_2^- + \bullet\text{O}_2^- \rightarrow 2 \text{Br}^- + \text{O}_2$	$1.7 \times 10^8$	Ross et al. (1998)
14	$\bullet\text{Br}_2^- + \bullet\text{Br}_2^- \rightarrow \text{Br}_2 + 2 \text{Br}^-$	$3.0 \times 10^9$	Ershov (2004)
15	$\text{Br}_3^- + \text{HO}_2\bullet \rightarrow \bullet\text{Br}_2^- + \text{HBr} + \text{O}_2$	$1 \times 10^7$	Ross et al. (1998)
16	$\text{Br}_3^- + \bullet\text{O}_2^- \rightarrow \bullet\text{Br}_2^- + \text{Br}^- + \text{O}_2$	$3.8 \times 10^9$	Ross et al. (1998)
17	$\text{Br}_2 + \bullet\text{O}_2^- \rightarrow \bullet\text{Br}_2^- + \text{O}_2$	$5.6 \times 10^9$	Ross et al. (1998)
18	$\text{Br}_2 + \text{HO}_2\bullet \rightarrow \bullet\text{Br}_2^- + \text{H}^+ + \text{O}_2$	$1.1 \times 10^8$	Ross et al. (1998)
19	$\text{Br}_2\text{OH}^- + \text{H}^+ \rightarrow \text{Br}_2 + \text{H}_2\text{O}$	$2 \times 10^{10}$	Eigen & Kustin (1962)
20	$\text{Br}_2\text{OH}^- \rightarrow \text{HOBr} + \text{Br}^-$	$5 \times 10^9$	Eigen & Kustin (1962)
21	$\text{HOBr} + \bullet\text{OH} \rightarrow \bullet\text{BrO} + \text{H}_2\text{O}$	$2.0 \times 10^9$	Ross et al. (1998)
22	$\text{HOBr} + \bullet\text{O}_2^- \rightarrow \text{BrOH}^-$	$3.5 \times 10^9$	Ross et al. (1998)
23	$\text{BrO}^- + \bullet\text{OH} \rightarrow \bullet\text{BrO} + \text{OH}^-$	$4.5 \times 10^9$	Ross et al. (1998)
24	$\text{BrO}^- + \bullet\text{O}_2^- + \text{H}_2\text{O} \rightarrow \bullet\text{Br} + 2 \text{OH}^- + \text{O}_2$	$2 \times 10^8$	Ross et al. (1998)



## Chapter 3 Materials and methods



### 3.1 Chemicals

Aeroxide<sup>®</sup> TiO<sub>2</sub> Degussa P25 and Sulfamethoxazole (SMZ) were purchased from Evonik Industries, Germany and MP Biomedicals, LLC, France, respectively. The commercial TiO<sub>2</sub> powder (Degussa P25) was selected in this study for its wide popularity as a photocatalyst and because there is plenty of published data on its photocatalytic behaviors. Sodium bromide (NaBr, 99.5%) and sodium chloride (NaCl, 99.5%) were obtained from Sigma-Aldrich. Leonardite humic acid (LHA) (IHSS code: 1S104H) and Suwannee river humic acid (SRHA) (IHSS code: 2S101H) were purchased from International Humic Substance Society (IHSS). Double deionized (DI) water was used for all experiments. Stock solutions of SMZ, LHA and SRHA were stored at 4°C in the dark, and let them reach to room temperature before use. All the experiments were performed at room temperature (25 ± 2 °C).

### 3.2 Synthesis of HBr-P25, HCl-P25, NaBr-P25 and NaCl-P25

The catalyst pretreatment method employed is based upon the technique used by Lewandowski and Ollis (2003). Surface brominated TiO<sub>2</sub> was obtained by impregnation of 0.3 g of P25 into 1 mL of 1 M HBr or NaBr, followed by a drying process at room temperature in the hood for about 4 hr, and with a further 60 °C drying in the oven for 5 days. Once the drying was completed, the catalyst samples were ground using a mortar and pestle to break up agglomerates and to prepare the titania for use in photocatalytic experiments. As for surface chlorination of TiO<sub>2</sub>, HCl and NaCl were used in the same process.

### 3.3 Characterization

#### 3.3.1 Dynamic light scattering (DLS)

Dynamic light scattering (DLS) (Zetasizer, NanoZS, Malvern Instruments) experiments were performed to analyze the hydrodynamic diameter, size distribution, and zeta potential of TiO<sub>2</sub>. DLS instrument utilized a laser beam at 633 nm to determine the size by measuring the particles' Brownian motion of the sample, and the measurements were conducted at an angle of 173° and at 25 °C. The viscosity of water was 0.08872 and refraction index was 1.330, while the refraction index of TiO<sub>2</sub> was 2.50 and the adsorption was 0.01. DLS measurements were conducted by adding 1.5 mL of sample into a plastic cell. On the other hand, zeta potential measurements were also conducted at 25 °C. TiO<sub>2</sub> suspensions were injected in folded capillary cells, and the electrophoretic mobility was measured using a combination of electrophoresis and laser Doppler velocimetry techniques.

#### 3.3.2 Transmission electron microscope (TEM)

Morphologies of the samples were examined using a transmission electron microscope (TEM, JEOL Corp. JEM2010, Japan). TEM specimens were made by evaporating one drop of solution that dissolved TiO<sub>2</sub> in methanol onto Formvar/Carbon film-coated 200 mesh copper grids. The average particle size ( $d_{\text{TEM}}$ ) and particle size distribution were determined by TEM images with counting more than 100 particles.

#### 3.3.3 Field-emission scanning electron microscope (SEM)

The morphologies and the elemental composition of the samples were investigated by using a field-emission scanning electron microscope (SEM, JEOL Corp. JSM-7600F, Japan) equipped with an energy dispersive X-ray spectrometer

(EDX) for semiquantitative chemical analysis. The powder of TiO<sub>2</sub> nanoparticles was washed by ethanol and water for three times, and then dried at 200 °C in the oven for 2 hr. The samples were stuck on the carbon conductive tape.



### **3.3.4 Brunauer-Emmett-Teuller (BET) surface area**

The specific surface area and pore size distribution was analyzed by using Brunauer-Emmett-Teuller (BET) N<sub>2</sub> adsorption method (Micromeritics ASAP-2020). Samples were degassed and calcined at 373 K for 24 h before adsorption experiments using N<sub>2</sub> as the adsorbate. The relative pressure (P/P<sub>0</sub>) was within the range of 0.05 - 0.35. The average pore radius was also recorded.

### **3.3.5 X-ray diffraction (XRD)**

The crystal structure of the particles was determined by X-ray diffraction (XRD) synchrotron radiation at the 13A1 beam line of SRRC, Taiwan, R.O.C., using bicron diffractometer with a wavelength of 1.02 Å adjusted with Si (111) monochromator. The samples were scanned from 10° to 60° (2θ) with step increments of 0.05° and time per step of 1 s. Because the synchrotron radiation wavelength is different from the common Cu Kα radiation, in order to compare with the database, XRD results in this study are presented in the wavelength of 1.54 Å.

### **3.3.6 Fourier transform infrared spectroscopy (FTIR)**

FTIR spectra were recorded by a FTIR spectrometer (Magna 860, Thermo-Nicolet Instruments, Madison, WI, USA) at the 14A1 beam line of SRRC, Taiwan, R.O.C. The spectra were collected in the mid-infrared range of 4000 – 400 cm<sup>-1</sup> with the co-addition of 256 scans. The samples (0.2 g KBr and 0.001 g TiO<sub>2</sub>) were ground using a mortar and pestle to mix well, and then hydraulically pressed

into tablets for use of FTIR experiments.



### **3.3.7 Raman spectroscopy**

The home-built confocal Raman microscope is equipped with a monochromator (Shamrock SR 303i-A, Andor Technology, USA), a He-Ne laser (25-LHP-928-249, CVI Melles Griot, USA), a thermos-electric cooling CCD (DU 401-BR-DD-968, Andor, USA) and a microscope (BX51, Olympus, Tokyo, Japan). The sample of Raman spectroscopy was placed on a stainless steel holder and analyzed.

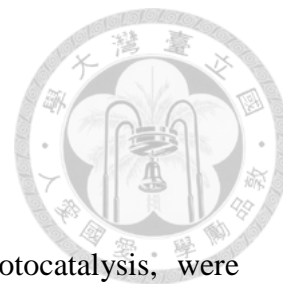
### **3.3.8 X-ray photoelectron spectroscopy (XPS)**

The XPS spectra of TiO<sub>2</sub> NPs were obtained with a VG Scientific ESCALAB 250 spectrometer using Al K $\alpha$  irradiation source operated at 15 kV and 200W of beam size 650~120  $\mu$ m. XPS analysis was performed on TiO<sub>2</sub> NPs, which were dried from TiO<sub>2</sub> NP suspensions. The air pressure in the vacuum chamber was below 10<sup>-8</sup> Pa. Quantitative analysis was carried out using the spherical sector analyzer with a Multi-channeltron array, which theoretical energy resolution was 20 meV~8 eV (CAE mode), 0.02%~2.0% (CRR mode).

## **3.4 Aggregation and sedimentation of TiO<sub>2</sub>**

In this study, the aggregation experiments of TiO<sub>2</sub> NP suspensions were conducted over a wide range of pH and salt concentrations. The batch experiments were performed to investigate the effects of TiO<sub>2</sub> NPs with different salts and different concentration including NaBr and NaCl on the aggregation of TiO<sub>2</sub>. For aggregation experiments, DLS analysis was used to access particle size at various time points. The sedimentation of TiO<sub>2</sub> NPs was determined according to time-resolved optical absorbance by using an ultraviolet-visible spectrophotometer (UV-Vis, CT-2200,

Chrom Tech, Inc., Apple Valley, MN, USA) at 300 nm.



### 3.5 Photodegradation experiments

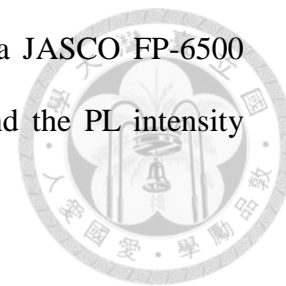
All experiments, including adsorption, photolysis, and photocatalysis, were performed in a photochemical reactor (PR-2000, Panchum) equipped with 4 UV lamps (8W for each lamp) with an UV-A wavelength of 365 nm, a rotator and a cooling fan. In a typical process, 200 mgL<sup>-1</sup> P25 stock solution was ultrasonicated for 30 min at first, and then 1 mL of P25 solution (final concentration: 10 mgL<sup>-1</sup>) was added into 10 mL, 10 mgL<sup>-1</sup> SMZ solution ( $C_0 = 5 \text{ mgL}^{-1}$ ) and 9 mL deionized water, standing for 30 min to reach an adsorption/desorption equilibrium in the dark. After that, the sample solution was exposed to the UV light irradiation at room temperature and ambient pressure. At given time intervals, 1mL of the suspension was taken out, and then analyzed by high-performance liquid chromatography (HPLC) with a UV-vis detector (VWD). Each experiment was conducted in triplicate to assure data quality.

The photocatalytic activity of the as prepared HBr-P25, HCl-P25, NaBr-P25 and NaCl-P25 was also evaluated by the degradation of SMZ under UV light illumination at room temperature and ambient pressure. First, 0.006 g HBr-P25, HCl-P25, NaBr-P25 or NaCl-P25 was added into 10 mL, 10 mgL<sup>-1</sup> SMZ solution ( $C_0 = 5 \text{ mgL}^{-1}$ ) and 10 mL deionized water, standing for 30 min to reach an adsorption/desorption equilibrium in the dark. The photodegradation experiments and analytic process of HBr-P25, HCl-P25, NaBr-P25 and NaCl-P25 were the same as those of P25.

### 3.6 Photoluminescence (PL)

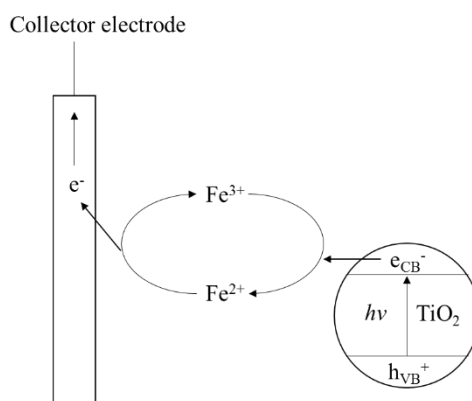
Photoluminescence (PL) is a suitable tool to study the efficiency of charge carrier trapping, migration, and transfer, and to understand the fate of electron-hole

pairs in photocatalyst particles. PL spectra were obtained using a JASCO FP-6500 spectrofluorometer. The samples were excited at  $\lambda = 350$  nm and the PL intensity maximum occurred at  $\lambda = 575$  nm.



### 3.7 Photocurrent

Measurements of the photocurrent collected on an inert electrode (graphite) immersed in aqueous suspension of  $\text{TiO}_2$  were carried out with a CHI614D electrochemical analyzer (CH Instruments, Inc., Shanghai).  $\text{Fe}^{3+}/\text{Fe}^{2+}$  redox couple was used as an electron shuttle that carries the electron from the  $\text{TiO}_2$  particles to the C electrode, and no external electron donor was added (Park & Choi, 2004; Park et al., 2009). A graphite rod, a saturated-KCl Ag/AgCl electrode (SSE), and Pt wire were used as a working, a reference and a counter electrode, respectively. Photocurrents were collected in the suspension by applying a potential (+0.6 V vs SSE) to the working electrode using a potentiostat (CHI614D) connected to a computer.



Scheme 3-1.  $\text{Fe}^{3+}$  mediated current collection on an inert C electrode immersed in UV-illuminated  $\text{TiO}_2$  suspension.

### 3.8 ROS measurements

#### 3.8.1 Trapping experiments of radicals and holes

The trapping experiments will be carried out under the similar experimental

conditions as that for photodegradation of SMZ, except that the specific scavengers will be added into the suspension before UV light irradiation. The main oxidative species detected by the trapping experiments will be free and surface-bound  $\bullet\text{OH}$ , and holes by using tertiary butanol (*t*-buOH), allyl alcohol (AA) and oxalate (e.g. oxalic acid and sodium oxalate), respectively (Barazesh et al., 2016; Rodríguez et al., 2015).

Allyl alcohol (AA; 100 mM) or tertiary butanol (*t*-buOH; 100 mM) were used as selective quenchers to differentiate the importance of reactions involving adsorbed radicals (e.g.,  $\bullet\text{OH}_{\text{ads}}$  and  $\bullet\text{Br}_{\text{ads}}$ ) and dissolved radicals (e.g.,  $\bullet\text{OH}$  and  $\bullet\text{Br}$ ) to SMZ photocatalytic degradation rates, respectively (Barazesh et al., 2016).

Oxalate (e.g. oxalic acid and sodium oxalate) was used as a hole scavenger to investigate the role of photogenerated hole on the surface of catalysts. The concentration of  $\text{C}_2\text{O}_4^{2-}$  was fixed at 10 mM (Lee et al., 2005; Rodríguez et al., 2015).

### 3.8.2 The measurements of hydroxyl radicals

Coumarin and coumarin-3-carboxylic acid (CCA) were employed for the detection of  $\bullet\text{OH}$  in the  $\text{TiO}_2$  suspension and near the  $\text{TiO}_2$  surface, respectively (Nosaka & Nosaka, 2017; Zhang & Nosaka, 2015). Coumarin reacts with  $\bullet\text{OH}$  to form several OH substituted coumarins, including 7-OH coumarin (umbelliferone) which is the only product that emits strong fluorescence (Figure 3-1a). On the other hand, CCA can react with  $\bullet\text{OH}$  near the surface of  $\text{TiO}_2$  to form OH-CCA, shown in Figure 3-1b. Briefly, 0.1 mM coumarin or CCA aqueous solution was added into  $\text{TiO}_2$  solution with or without 10, 100 and 500 mM NaBr. After irradiation, 2 mL of the suspension was taken out, diluted and analyzed by fluorescence spectrometer. The fluorescence spectra were measured using a JASCO FP-6500 spectrofluorometer with the excitation wavelength of 332 or 340 nm for 7-hydroxycoumarin or OH-CCA, respectively. On the other hand, the emission wavelength of 7-hydroxycoumarin and

OH-CCA were 456 and 445 nm, respectively.

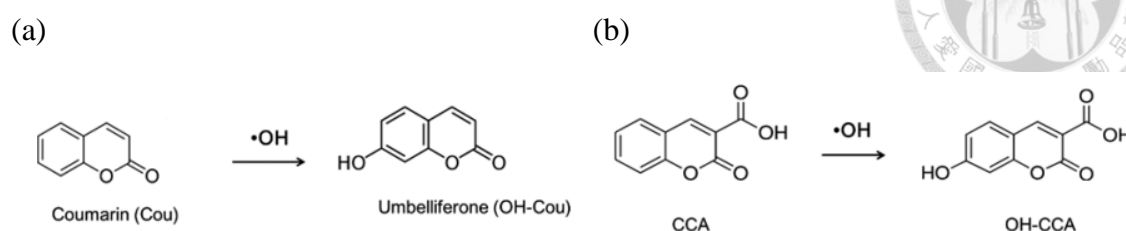


Figure 3-1. Reactions for detection of  $\bullet\text{OH}$  with fluorescence probes, (a) coumarin, and (b) coumarin-3-carboxylic acid (CCA), which become corresponding fluorescent molecules to be measured with a common fluorescence spectrometer. (Nosaka & Nosaka, 2017)

### 3.8.3 The measurement of chlorine and bromine species

The chlorine and bromine concentration can be determined by N,N-diethyl-p-phenylenediamine (DPD) colorimetric method (Emerson, 1994; Gallard et al., 2004; Moberg & Karlberg, 2000; Palin, 1975). This method uses DPD to react with free chlorine (hypochlorous acid and hypochlorite) and free bromine (hypobromous acid and hypobromite). If free chlorine or free bromine is present in the sample, a magenta intermediate forms rapidly and the absorbance is measured at 515 nm (Figure 3-2). The analytically useful range of the calibration graph is 0.05–4  $\text{mgL}^{-1}$  (according to Standard Methods (1985), or equivalently, 0.7–56  $\text{mmolL}^{-1}$ ). The rapidly formed intermediate fades and the end product is colorless (Figure 3-2) (Moore et al., 1984). This fading reaction is slow in comparison with the rapidly occurring intermediate reaction, which only requires some seconds to reach completion. Consequently, it is important that the absorbance reading is done immediately following the addition of the reagent and buffer solutions. Upon further oxidation, when high concentrations of oxidizing species are present, the color at 515



nm will disappear, i.e., the end product of this two-step oxidation is colorless. Samples are diluted when suspected of containing high chlorine or bromine concentrations.

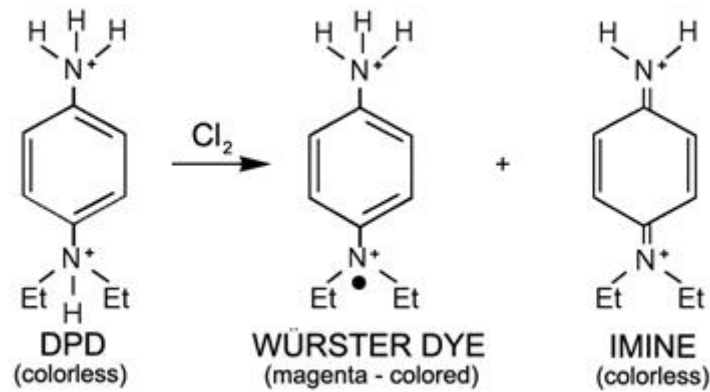


Figure 3-2. The reaction between DPD and chlorine in water (Van London Company, 2015).

The phosphate buffer solution was prepared by dissolving 24 g anhydrous Na<sub>2</sub>HPO<sub>4</sub> and 46 g anhydrous KH<sub>2</sub>PO<sub>4</sub> in distilled water, and then combined with 100 mL distilled water including 800 mg/L disodium ethylenediamine tetraacetate dehydrate (EDTA). DPD solution was prepared by dissolving 0.57 g DPD in distilled water containing 8 mL 1 + 3 H<sub>2</sub>SO<sub>4</sub> and 200 mg disodium EDTA, and then dilute to 1 L. The indicator solution was prepared by mixing 1 mL of DPD solution and 1 mL of phosphate buffer solution. After adding 20 mL of the sample into the indicator solution and mixing, the intensity of the color was measured with the spectrophotometer at 515 nm.

The calibration curve was made by preparing different concentrations of potassium permanganate solutions, uniformly mixing with the indicator solution and measuring by a spectrophotometer. Took the measured solution back into Erlenmeyer flask, and immediately titrated the solution by 0.00282 M ferrous ammonium sulfate solution until the red color disappeared. Calculated the equivalent chlorine

concentration (mg/L) by eq. 3-1. Prepared the calibration curve by corresponding the absorbance with the equivalent chlorine concentration.

$$\text{Equivalent chlorine concentration (mg/L)} = [(\text{FAS conc. (M)} \times \text{FAS volume (mL)})/100 \text{ (mL)}] \times (158/5) \times (1/0.891) \times 1000 \quad (3-1)$$

### 3.8.4 The measurement of bromine by dibromocyclohexane test

To ascertain the role  $\text{TiO}_2$  plays in the oxidation of bromide in aqueous system, the dibromocyclohexane test was conducted. The product of bromination of cyclohexene in water is *trans*-1,2-dibromocyclohexane (Shaw et al., 1997). In this test, 5 mg/L cyclohexene was added into the solution containing 10 mg/L P25 and different concentration of NaBr. Irradiation was carried out in a photochemical reactor (PR-2000, Panchum) equipped with 4 UV lamps (8W for each lamp) with an UV-A wavelength of 365 nm, a rotator and a cooling fan. The sample solution was exposed to the UV light irradiation at room temperature and ambient pressure. At given time intervals, 1mL of the suspension was taken out, and then extracted by 1 mL hexane on a vortex orbital mixer (Genie 2, G560) for 1 hr. The concentration of cyclohexene and *trans*-1,2-dibromocyclohexane was analyzed by gas chromatograph (GC, Agilent 6890) equipped with electron-capture dissociation detector (GC-ECD). The column was DB-5 (30 m  $\times$  0.32 mm) with 0.25 mm film. The carrier gas was ultra-high-purity  $\text{N}_2$  of 99.999 % and its flow rate was 6.7 mL/min. The splitless inlet temperature was 200°C. The initial oven temperature was 60°C, first ramped at 5°C /min to 70°C, holding for 2 minutes, and then ramped at 25°C /min to 200°C, holding for 7.2 minutes. The detector temperature was 340°C. The retention time of cyclohexene and *trans*-1,2-dibromocyclohexane was 4.1 and 2.4 min, respectively.

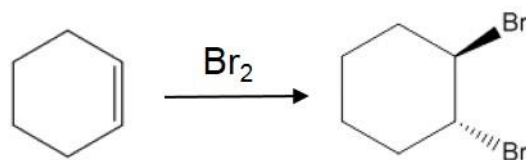


Figure 3-3. The bromination of cyclohexene.



### 3.8.5 The measurement of photocatalytic sites by TBO method

The density of photocatalytic sites for the formation of surface hydroxyl and bromine radical (i.e.,  $\equiv\text{TiOH}$ ) was determined using the toluidine blue O (TBO) colorimetric method (Barazesh et al., 2016; Chua et al., 2005; Ray et al., 2012). First, dropped 5 mL, 200 mg/L  $\text{TiO}_2$  solution on the slide glass and dried the slide glass at 60 °C for 3 days in the oven. Placed the slide glass into 20 mL water containing NaBr or not for 15 min under UV light irradiation. Then, the slide glass was submerged in 20 mL, 0.05 mM TBO at pH 10.0 for 6 h at 30 °C to promote TBO adsorption to surface functional groups (i.e.,  $\equiv\text{TiO}^-$ ). The area of the slide glass submerged in the TBO solution was 2 cm  $\times$  2.5 cm. Excess TBO was rinsed off with 1 mL, 1 M NaOH and adsorbed TBO was subsequently desorbed in 20 mL of 50% acetic acid for 10 min. The TBO concentration was measured by UV-vis spectrometer at 633 nm. To calculate the density of photocatalytic sites, it was assumed that 1 mol TBO had complexed with 1 mol of carboxyl groups.

### 3.8.6 Transient absorption spectra (TAS)

Laser flash photolysis (LFP) experiments were performed using a laser flash photolysis spectrometer (LP980, Edinburgh Instruments Ltd.) equipped with a frequency tripled Q-switched Nd:YAG laser, which provided 355 nm pulse with a duration of 8 ns (Hui Liu et al., 2009). The average laser power was 10 mJ/pulse. Experiments were carried out in a 1-cm quartz cuvette. The transient absorption

spectra (TAS) were measured by an intensified charged-coupled device (ICCD). In this study,  $\Delta OD$  means the transient absorption change.



### 3.8.7 Halide ions

The concentration of bromide ( $\text{Br}^-$ ), bromate ( $\text{BrO}_3^-$ ), chloride ( $\text{Cl}^-$ ) and chlorate ( $\text{ClO}_3^-$ ) will be determined by ion chromatography (IC, Metrohm) with a guard column and a Metrosep A Supp 5 column (150 mm x 4.0 mm). Hypobromous acid (HOBr) and hypobromite ( $\text{BrO}^-$ ) were analyzed by a DPD method (standard, 4500-Cl)(Eaton et al., 1995; Gunten & Oliveras, 1998).

In order to detect any production of bromine, we also attempted to detect the presence of tribromide ion ( $\text{Br}_3^-$ ) which is quantitatively formed from the reaction between  $\text{Br}_2$  and  $\text{Br}^-$ . Ultraviolet-visible spectrophotometer (UV-Vis, CT-2200, Chrom Tech, Inc., Apple Valley, MN, USA) was used to analyze  $\text{Br}_3^-$  at 267 nm (Wu et al., 2016).

## 3.9 Analytical methods

### 3.9.1 HPLC

SMZ was analyzed by HPLC (Agilent, 1200 Series) with a UV-vis detector (VWD). The chromatographic separation was performed using C18 column (150 mm x 4.6 mm, 5  $\mu\text{m}$ ). The isocratic mobile phase consisted of methanol and deionized water with the ratio of 50:50 (v/v). The flow rate of the mobile phase was set at 0.6  $\text{mL min}^{-1}$ . The column temperature was maintained at 30  $^\circ\text{C}$  and the detection wavelength was 267 nm. The retention time for SMZ was 4.5 min.

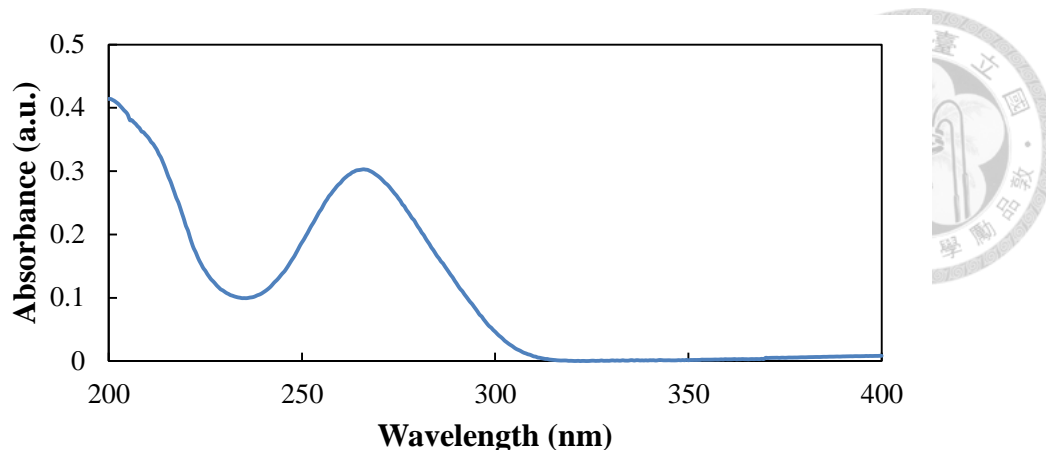


Figure 3-4. The absorbance spectrum of SMZ.

### 3.9.2 Byproducts and mineralization efficiency

High-performance Liquid chromatography/MS (HPLC/MS) was used for the identification of transformation products generated during the photodegradation process. Analysis was conducted on a Bruker microTOF-Q II (ESI-Q-TOF/MS) system outfitted with a Agilent 1200 HPLC system. Separation was accomplished using an Agilent C18 column (Zorbax, TC-C18 (2), 150 × 4.6 mm, 5 μm). Separation of analytes was achieved using a flow rate of 0.5 mL/min and a gradient method with two mobile phases: mobile phase A was 100% methanol; mobile phase B was 100% H<sub>2</sub>O. Mobile phase A was maintained at 50 % for the first 0.01 min, then the percentage of phase A was increased to 90 % for 10 min. MS analyses were conducted in positive mode electrospray ionization (ESI) over a mass range of 50 ~500 m/z.

## 3.10 Calculation

### 3.10.1 SMZ reaction rate constants

The pseudo-first-order model was used to describe the removal of SMZ using TiO<sub>2</sub> NPs.

$$dC/dt = -kC$$

$$\ln (C_t/C_0) = -kt$$

$$C_t = C_0e^{-kt}$$



(3-2)

(3-3)

(3-4)

where  $C_t$  ( $\text{mg L}^{-1}$ ) was the concentration of SMZ at time  $t$ ,  $C_0$  ( $\text{mg L}^{-1}$ ) was the initial concentration of SMZ,  $k$  ( $\text{min}^{-1}$ ) is the estimated rate constants, and  $t$  is the reaction time (min).

### 3.10.2 Removal efficiency

The ratio of the concentration difference between the initial concentration of SMZ and its final concentration to its initial concentration was defined as removal efficiency of SMZ reacted with  $\text{TiO}_2$  NPs.

$$\text{Removal efficiency of SMZ} = (C_0 - C_f)/C_0 (\%) \quad (3-5)$$

where  $C_f$  ( $\text{mg L}^{-1}$ ) was the final concentration of SMZ, and  $C_0$  ( $\text{mg L}^{-1}$ ) was the initial concentration of SMZ.

## Chapter 4 Results and Discussion



### 4.1 Characterization of TiO<sub>2</sub>

#### 4.1.1 DLS, zeta potential, TEM, and SEM-EDX

The DLS measurements, as shown in Figures 4-1a~e, revealed that the Z-average hydrodynamic particle diameters of TiO<sub>2</sub> (P25) nanoparticles (NPs), HBr-P25, HCl-P25, NaBr-P25, and NaCl-P25 were around 180 nm, 400 nm, 196 nm, 879 nm, and 582 nm, respectively. According to the result of zeta potential measurements (Figure 4-1f), the  $\text{pH}_{\text{zpc}}$  of P25, HBr-P25 and HCl-P25 were 7.03, 7.10 and 7.38, respectively. The sizes and morphologies of P25 NPs were further examined through TEM images in Figure 4-2a. The TEM images of P25 indicated that P25 consisted of aggregated primary particles, and the primary particles had a mean diameter of approximately 26.5 nm, and they were all in spherical shape. Moreover, HR-TEM results, as shown in Figure 4-2b, depicted the interplanar spacing of 0.352 and 0.248 nm, which were indexed to the (101) plane of anatase TiO<sub>2</sub> and (101) plane of rutile TiO<sub>2</sub>, respectively (Cheng et al., 2018; Y. Li et al., 2017).

SEM-EDX was used for investigating the morphologies and the elemental composition of P25, HBr-P25, HCl-P25, NaBr-P25 and NaCl-P25. The synthesis of HBr-P25, HCl-P25, NaBr-P25 and NaCl-P25 was elucidated in Section 3.2. In preparation, the calculated surface doping ratio of HBr-P25, HCl-P25, NaBr-P25 and NaCl-P25 was 26.97 %, 12.15 %, 34.30 % and 19.48 %, respectively. According to Figures 4-3a~e, HBr-P25, HCl-P25, NaBr-P25 and NaCl-P25 displayed spherical morphologies that formed aggregates, which were similar to P25. The EDX results of HBr-P25 and NaBr-P25 revealed that bromine existed in the sample, as shown in Figures 4-4a and c, respectively. Besides, from Figure 4-4b and d, it was confirmed

that there was chlorine in HCl-P25 and NaCl-P25, respectively.

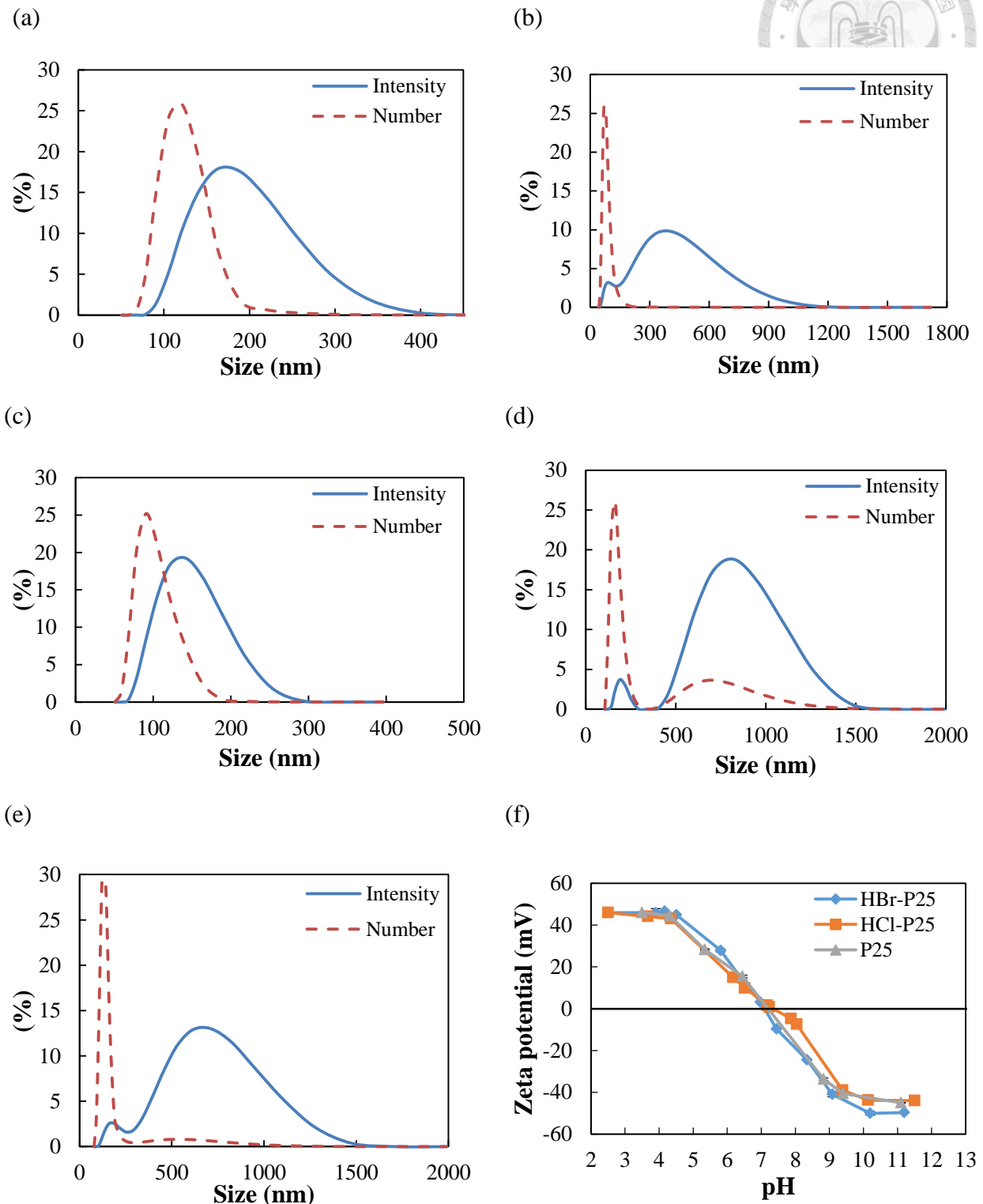


Figure 4-1. The DLS measurements of (a) P25, (b) HBr-P25, (c) HCl-P25, (d) NaBr-P25, (e) NaCl-P25, and (f) zeta potential measurements of P25, HBr-P25 and HCl-P25.



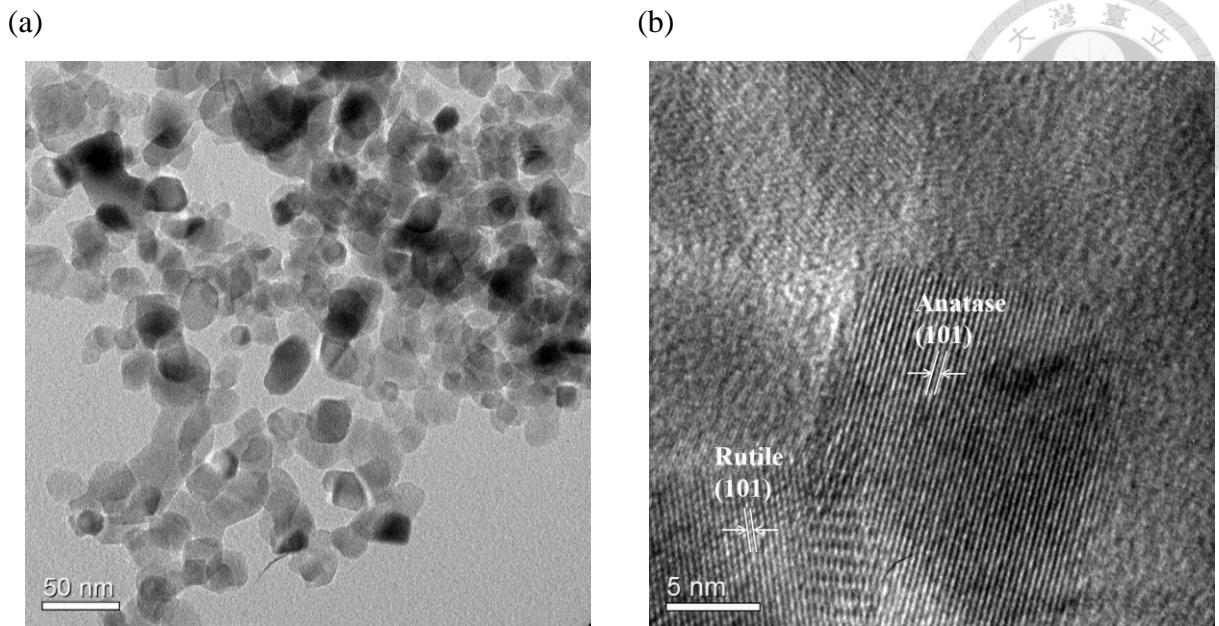


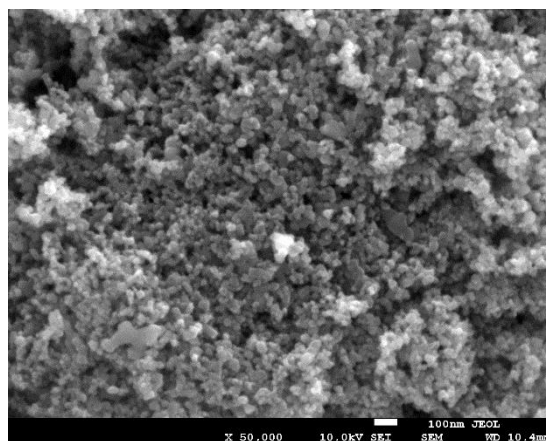
Figure 4-2. (a) The TEM images and (b) HRTEM image of P25 nanoparticles.

#### 4.1.2 BET surface area

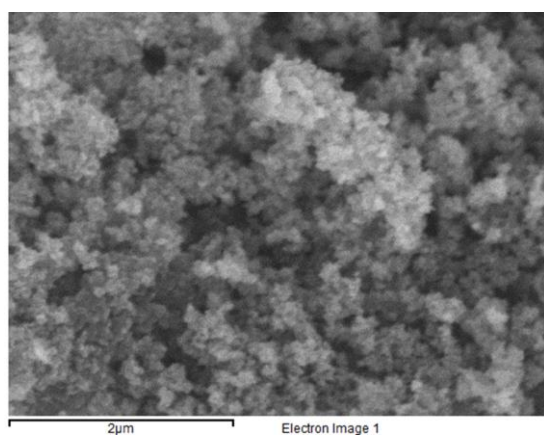
The surface area and pore volume of catalysts dominate the adsorption of target compound and then could affect the degradation rate. The surface area also influences the distribution of active sites on  $\text{TiO}_2$  which are related to the production of photogenerated electron-hole pairs and reactive oxygen species. Table 4-1 lists BET surface area, pore volume, and average pore diameter of P25 with different concentrations of NaBr. Table 4-2 lists BET surface area, pore volume, and average pore diameter of P25 with different concentrations of NaCl. It can be observed that when there were halide salts in the solution, the surface area of P25 particles decreased with the increasing concentration of halide salts. Table 4-3 lists BET surface area, pore volume, and average pore diameter of five samples of HBr-P25, HCl-P25, NaBr-P25 and NaCl-P25. The BET surface area of P25 was  $54.9 \text{ m}^2/\text{g}$ , and HBr-P25 and HCl-P25 had similar surface area, which were  $52.1$  and  $50.3 \text{ m}^2/\text{g}$ , respectively. However, the surface area of NaBr-P25 and NaCl-P25 was smaller than P25, indicating that they may have a poorer photocatalytic activity than P25.



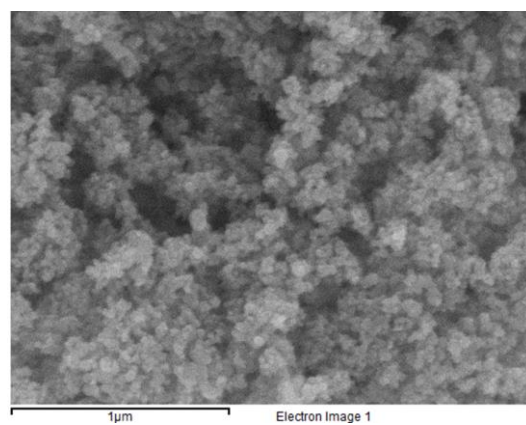
(a)



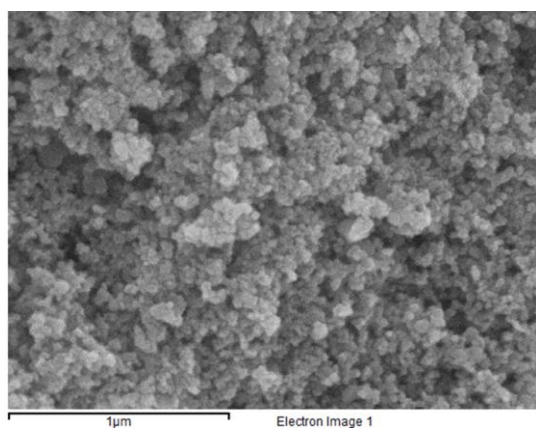
(b)



(c)



(d)



(e)

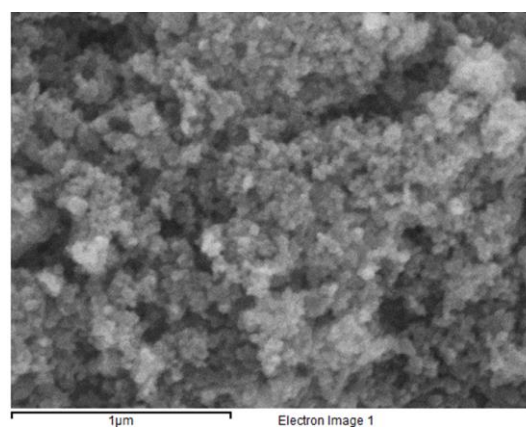


Figure 4-3. The SEM images of (a) P25, (b) HBr-P25, (c) HCl-P25, (d) NaBr-P25 and (e) NaCl-P25.

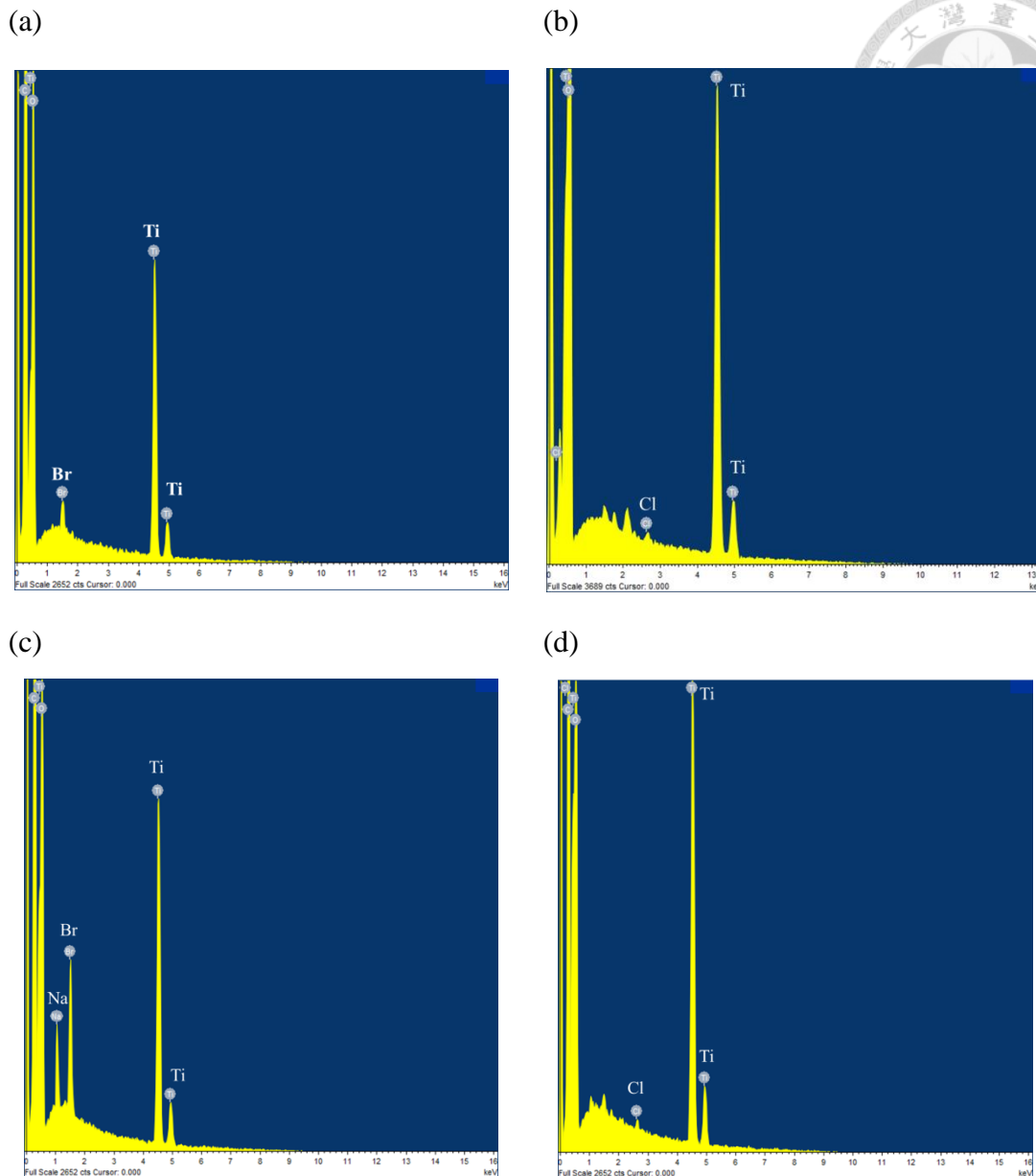


Figure 4-4. The EDX spectra of (a) HBr-P25, (b) HCl-P25, (c) NaBr-P25 and (d) NaCl-P25.

### 4.1.3 XRD

The XRD was used to characterize the purity and crystallinity of  $\text{TiO}_2$  nanoparticles shown in Figure 4-5. The diffraction peaks at  $2\theta$  values of 25.43, 37.99, 48.20, 54.13 and 55.34° can be indexed to (101), (004), (200), (105) and (211) crystal planes of anatase  $\text{TiO}_2$ , respectively (Kuvarega et al., 2013). On the other

hand, characteristic diffraction peaks at 27.57, 36.57 and 41.47° indicate the reflections of (111), (101) and (111) faces of the rutile phases (Kuvarega et al., 2014). All of the samples had obvious peaks of anatase and rutile phases of TiO<sub>2</sub>, except NaCl-P25. The XRD spectrum of NaCl-P25 just showed the (101) planes of anatase TiO<sub>2</sub>, but no other peaks. It could be assumed that the crystallinity of NaCl-P25 was not as good as other samples.

Table 4-1. The surface area, pore diameter and pore hydraulic radius of P25 with different concentrations of NaBr.

Samples	TiO <sub>2</sub> (P25)	P25+10 mM NaBr	P25+50 mM NaBr	P25+100 mM NaBr	P25+500 mM NaBr
BET surface area (m <sup>2</sup> /g)	54.99 ± 0.32	44.49 ± 0.15	39.49 ± 0.08	25.31 ± 0.11	6.73 ± 0.03
Langmuir surface area (m <sup>2</sup> /g)	77.66 ± 2.16	62.09 ± 1.63	55.01 ± 1.27	35.33 ± 0.97	9.26 ± 0.15
BJH adsorption average pore diameter (Å)	292	345	325	324	378
BJH desorption average pore diameter (Å)	275	321	298	298	323
MP-method average pore hydraulic radius (Å)	0	26	20	21	25

Table 4-2. The surface area, pore diameter and pore hydraulic radius of P25 with different concentrations of NaCl.

Samples	TiO <sub>2</sub> (P25)	P25+10 mM NaCl	P25+50 mM NaCl	P25+100 mM NaCl	P25+500 mM NaCl
BET surface area (m <sup>2</sup> /g)	54.99 ± 0.32	49.03 ± 0.22	48.18 ± 0.17	45.73 ± 0.15	33.64 ± 0.16
Langmuir surface area (m <sup>2</sup> /g)	77.66 ± 2.16	68.07 ± 1.90	66.76 ± 1.77	63.23 ± 1.66	47.10 ± 1.33
BJH adsorption average pore diameter (Å)	292	330	344	340	316
BJH desorption average pore diameter (Å)	275	310	318	309	294
MP-method average pore hydraulic radius (Å)	0	25	25	24	25

#### 4.1.4 FTIR

Presence of functionalities on the materials was confirmed by FTIR. In Figure 4-6, peaks at 3424 cm<sup>-1</sup> and 1635 cm<sup>-1</sup> can be ascribed to OH stretching of the surface hydroxyls and the OH bending vibrations of absorbed water molecules on the TiO<sub>2</sub> nanoparticles, respectively (Kuvarega et al., 2014; Panwar et al., 2016). These surface hydroxyl groups play an important role in the photocatalytic process because they act as molecule adsorption centres as well as hole scavenging sites for the generation of hydroxyl radicals with high oxidation capability (Kim et al., 2013). The broad peak in the range 750~520 cm<sup>-1</sup>, observed in all the samples, is due to stretching vibration of Ti–O, which is consistent with previous study (Kuvarega et al.,

2014). HBr and HCl molecules were chemisorbed on the surface of the partially hydroxylated TiO<sub>2</sub> (P25) by a ligand substitution reaction with the surface hydroxyl groups as follows (Minero et al., 2000):



This was confirmed by the FTIR spectra, exhibiting a significant decrease for the band at 3424 cm<sup>-1</sup> corresponding to O-H stretching modes due to the substitution of bromine and chlorine groups for hydroxyl groups, which is consistent with previous study (Yuan et al., 2011). However, this phenomenon could not be observed in NaBr-P25 and NaCl-P25. The samples of NaBr-P25 and NaCl-P25 even had stronger peak than P25 at 3424 cm<sup>-1</sup> ascribed to OH stretching of the surface hydroxyls.

Table 4-3. The surface area, pore diameter and pore hydraulic radius of different types of TiO<sub>2</sub>.

Samples	TiO <sub>2</sub> (P25)	HBr-P25	HCl-P25	NaBr-P25	NaCl -P25
BET surface area (m <sup>2</sup> /g)	54.99 ± 0.32	52.16 ± 0.20	50.33 ± 0.18	34.48 ± 0.11	43.30 ± 0.17
Langmuir surface area (m <sup>2</sup> /g)	77.66 ± 2.16	73.30 ± 2.00	70.13 ± 1.88	47.908 ± 1.25	59.95 ± 1.61
BJH adsorption average pore diameter (Å)	292	245	253	290	294
BJH desorption average pore diameter (Å)	275	232	237	284	278
MP-method average pore hydraulic radius (Å)	0	23	23	26	24

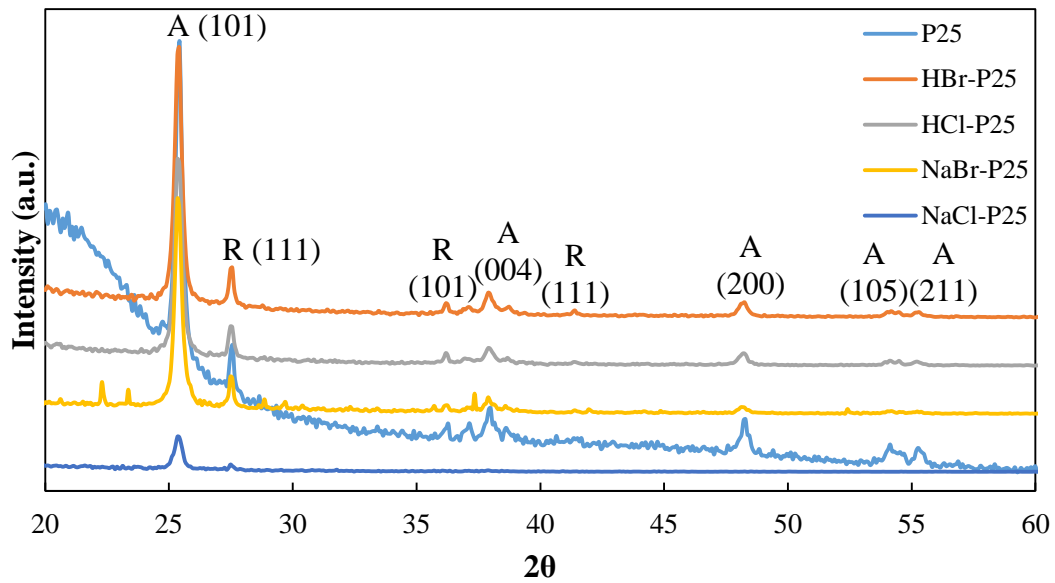


Figure 4-5. XRD patterns of different types of  $\text{TiO}_2$ . (A: anatase phases, R: rutile phases)

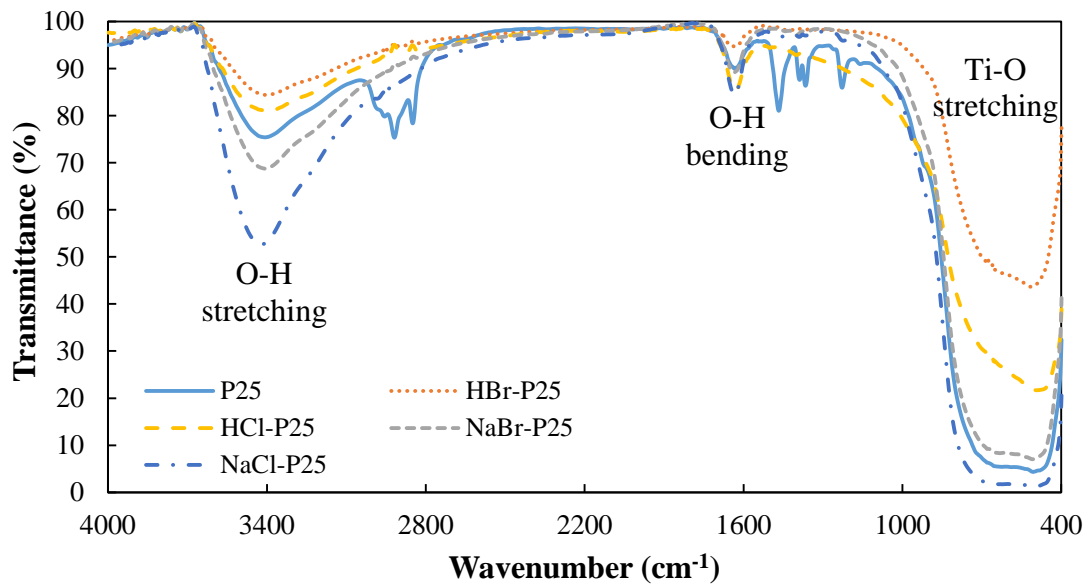


Figure 4-6. FTIR spectra of different types of  $\text{TiO}_2$ .

#### 4.1.5 Raman

Raman spectroscopy is a powerful technique for investigating various phases of crystalline  $\text{TiO}_2$  or its modified forms. The technique is capable of elucidating the photocatalyst structural complexity as phase peaks from each material are clearly

separated in frequency and therefore easily distinguishable. The particle size, defect, and crystallinity are the main factors which influence the Raman shift. Four peaks were observed for all the samples at wavenumbers of 145, 196, 397, 515, and 638  $\text{cm}^{-1}$  and are attributed to the strong  $E_g$ , the medium strength  $B_{1g}$ , the  $A_{1g}$ , and an  $E_g$  Raman mode, respectively (Figure 4-7). These observations are consistent with reported fundamental Raman peaks of anatase  $\text{TiO}_2$  (Dukes et al., 2012; Kuvarega et al., 2014). In contrast, the rutile phase which consists of weak features at 142  $\text{cm}^{-1}$ , 320  $\text{cm}^{-1}$ , 357  $\text{cm}^{-1}$ , and 826  $\text{cm}^{-1}$  and stronger peaks at 447  $\text{cm}^{-1}$  and 612  $\text{cm}^{-1}$  (Kuvarega et al., 2013) could not be clearly detected, though all of the samples were shown to have a certain percentage of the rutile phase through XRD analysis. This can be attributed to the low percentage rutile phase in all the samples, like P25 consisting of about 75% anatase and 25% rutile. No Raman lines due to the Br or Cl modification were observed in the HBr-P25, HCl-P25, NaBr-P25 and NaCl-P25 samples, suggesting that the concentrations of these dopants on the surface of  $\text{TiO}_2$  were too low to be detected in Raman spectra.

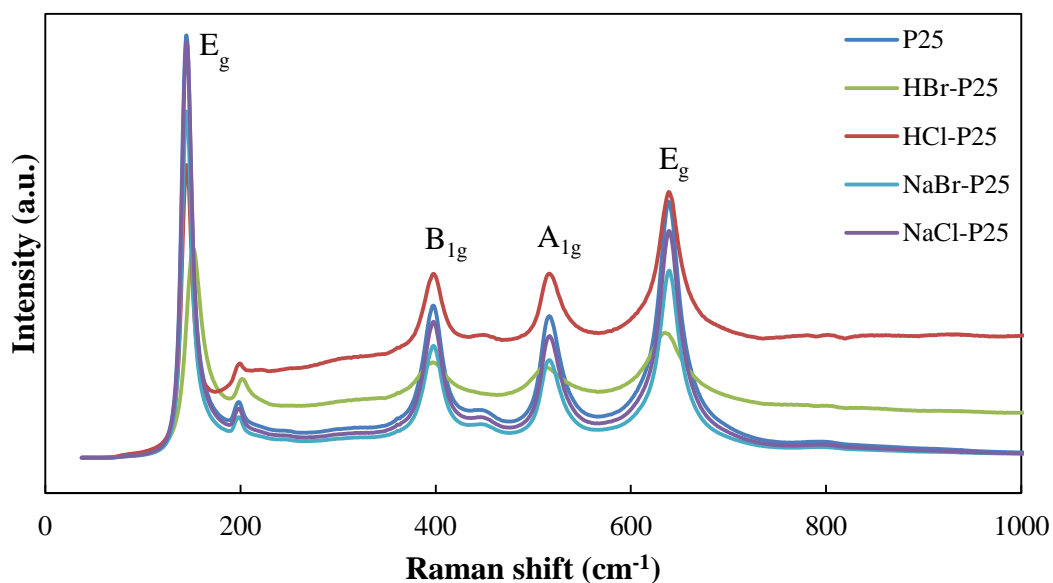
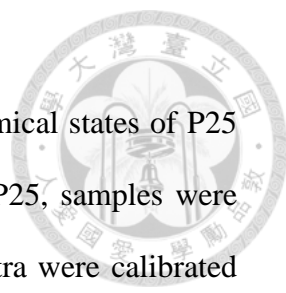


Figure 4-7. Raman spectra of different types of  $\text{TiO}_2$ .

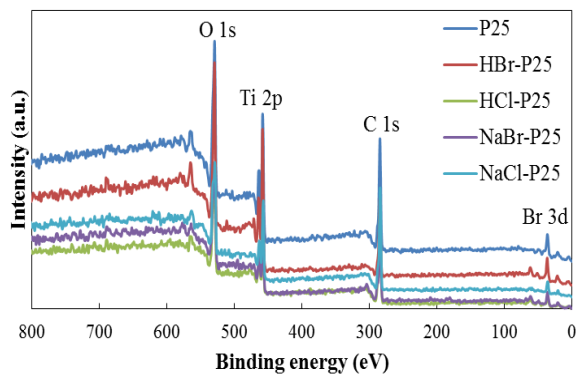


#### 4.1.6 XPS

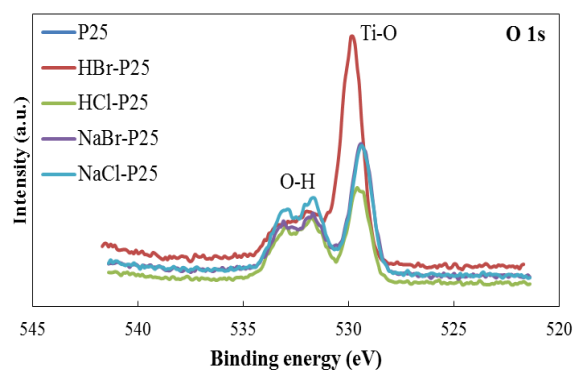


In order to clarify the elemental components and surface chemical states of P25 and the as-synthesized HBr-P25, HCl-P25, NaBr-P25 and NaCl-P25, samples were further analyzed by XPS. The peak positions in all the XPS spectra were calibrated with C 1s at 284.6 eV. As shown in Figure 4-8a, all relevant elements, including O and Ti, are clearly observed in P25, HBr-P25, HCl-P25, NaBr-P25 and NaCl-P25. Moreover, Br can be observed in HBr-P25 and NaBr-P25. The scanned XPS spectra of O 1s and Ti 2p are displayed in Figure 4-8b and c, respectively. Figure 4-8b showed a wide and lightly asymmetrical peak observed in the sample's O 1s signal, which could be divided into two peaks at 529.7eV and 532.6eV resulting from the lattice oxygen and surface hydroxyl oxygen, respectively (Cheng et al., 2018; Deng et al., 2018). From Figure 4-8c, the two major peaks at 458.5 and 464.3 eV corresponded to Ti 2p<sub>3/2</sub> and Ti 2p<sub>1/2</sub> orbits of the Ti<sup>4+</sup> in the sample, respectively (Deng et al., 2018; Geng et al., 2017; Wang, 2017). It could be observed that the Ti 2p<sub>3/2</sub> peak of HBr-P25 shifted to a higher binding energy compared to that of P25. This might result from the Ti-Br bonds on the surface of HBr-P25, affecting the chemical states of Ti. As displayed in Figure 4-8c, a single peak at binding energy of 68.2 eV was detected in the Br 3d, which was assigned to the presence of Br<sup>-</sup> (Cui et al., 2018; Wang, 2017; Zhang et al., 2017). Besides, a single peak at 62.1 eV was detected in Na 2s, which confirmed the presence of Na<sup>+</sup>, according to NIST X-ray Photoelectron Spectroscopy Database and previous study (Tissot et al., 2015). Therefore, XPS results provide good evidence that Br was successfully decorated onto the surface of P25 NPs. On the other hand, there was no Cl detected, which could be due to the low concentration of decorated Cl onto the surface of P25 NPs.

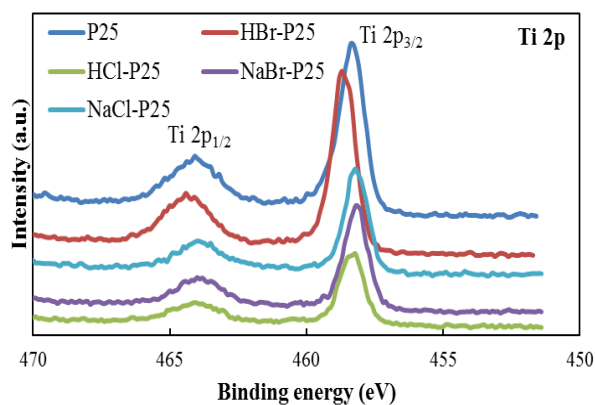
(a)



(b)



(c)



(d)

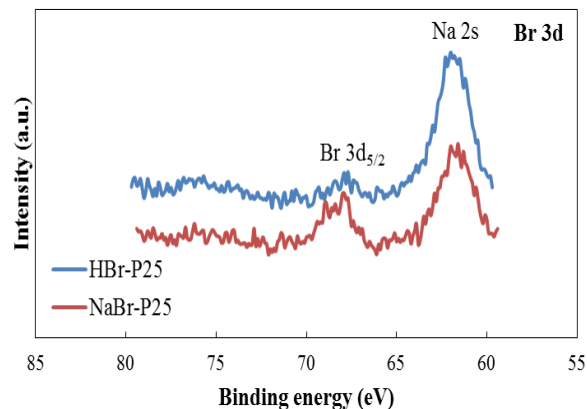
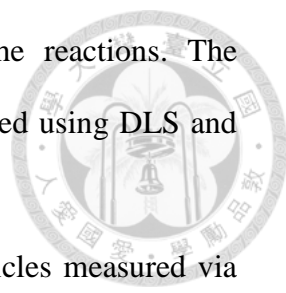


Figure 4-8. XPS full spectra (a), high-resolution XPS spectra of O1s (b) and Ti2p (c) for different TiO<sub>2</sub>. High-resolution XPS spectra of Br 3d (d) for HBr-P25 and NaBr-P25.

## 4.2 Aggregation and sedimentation of TiO<sub>2</sub>

Many reports have confirmed the significant effects of the particle size on the photocatalytic activity (Amano et al., 2013; Lin et al., 2006; Yurdakal et al., 2007). It is inevitable that there will be particle aggregation in aqueous solutions due to some factors such as the charge density/potential of the particle surfaces and van der Waals forces. Therefore, there is a need for studies on the effect of aggregation on the photocatalytic reactions. Sedimentation behavior is also important for TiO<sub>2</sub> because it

impacts on how many particles still exist in solutions for the reactions. The aggregation and sedimentation experiments of TiO<sub>2</sub> were conducted using DLS and UV-vis spectrometer at 300 nm, respectively.



The average hydrodynamic size of suspended TiO<sub>2</sub> nanoparticles measured via DLS can be determined as a function of time. The changes of particle size were measured by DLS and showed in the following paragraph with different conditions of aqueous solution in SMZ photodegradation. On the other hand, the UV-vis data provides the rate of disappearance of TiO<sub>2</sub> in the solution. The method of sedimentation experiment was established by measuring the absorbance of the suspension at 300 nm, and presented as a simple expression of C/C<sub>0</sub>.

#### 4.2.1 The effect of TiO<sub>2</sub> concentration

Figure 4-9 showed that the particle size of P25 did not change with the increase of TiO<sub>2</sub> from 10 ppm to 100 ppm, which meant that P25 NPs were stable in the solutions with SMZ.

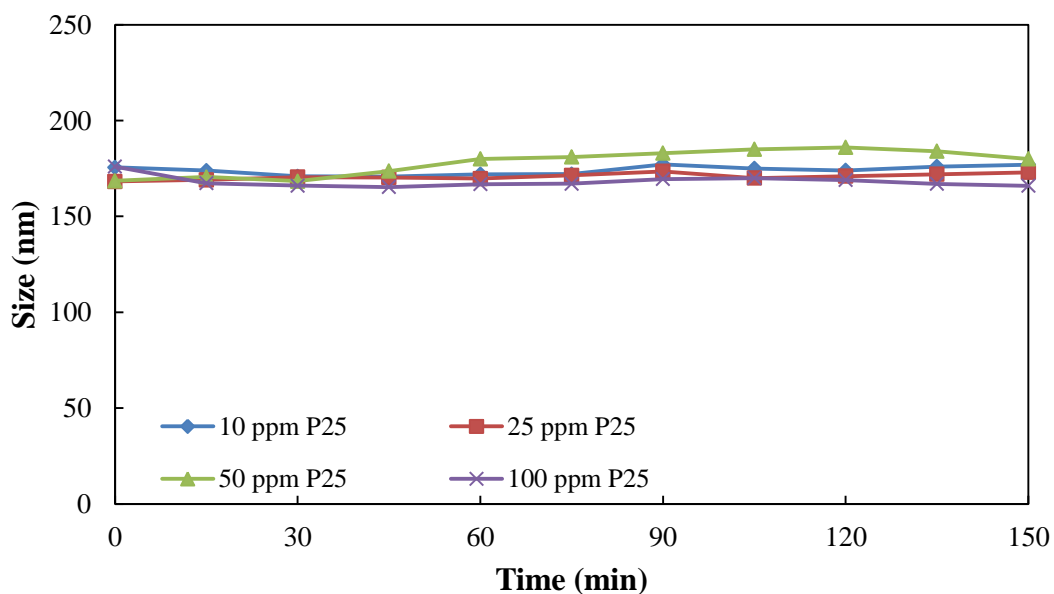


Figure 4-9. Aggregation kinetics of different concentrations of P25 in the solutions with 5 mg/L SMZ.

#### 4.2.2 The effect of sodium halides

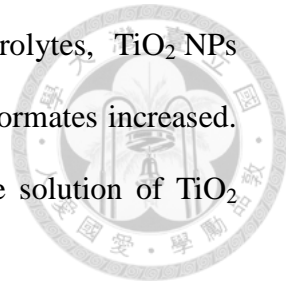
Electrolytes are common in the environment and affect the particle size (Peng et al., 2017; Peng et al., 2015). The degradation kinetic process is affected in a complex way by not only particle size but also aqueous composition. Therefore, it is important to investigate how the electrolytes affect the aggregation and sedimentation of TiO<sub>2</sub>.

Figure 4-10 showed the particle sizes of P25 changed with time as a function of NaCl concentrations. P25 remained in small size (about 180 nm) without NaCl addition and were well-dispersed. With addition of different concentrations of NaCl (10, 50, 100 and 500 mM), the particle sizes of P25 increased quickly within 3 min and exceeded 1000 nm after 15 min. The measured average sizes of P25 increased continuously with time during the experiments. Figure 4-11 showed that some P25 nanoparticles in water slightly settled down but still about 70% TiO<sub>2</sub> evenly dispersed in aqueous solutions within 3 hr.

The effect of NaBr on the aggregation and sedimentation behaviors of TiO<sub>2</sub> NPs was also investigated. Figure 4-12 showed the particle sizes of P25 changed with time as a function of NaBr concentrations. P25 remained in small size (about 180 nm) without NaBr addition and was well-dispersed. With addition of different concentrations of NaBr (10, 50, 100, 250 and 500 mM), the particle sizes of P25 increased quickly within 3 min and exceeded 1000 nm after 15 min. The measured average sizes of P25 increased continuously with time during the experiments. Figure 4-13 showed that the particle concentrations of P25 in water slightly decreased but still about 75% TiO<sub>2</sub> evenly dispersed in aqueous solutions within 150 min.

With the increase of NaBr or NaCl concentration, the particle size increased and particles aggregated obviously during the degradation experiments. The increase in ionic strength resulted in the compression of the electrical double layer (EDL) and therefore EDL repulsive energy decreased, bringing particles to easily aggregate.

Hsiung et al. (2016) indicated that in the presence of electrolytes, TiO<sub>2</sub> NPs aggregated but not settled down instantly until the density of agglomerates increased. Consequently, the aggregation and sedimentation occurred in the solution of TiO<sub>2</sub> with NaBr or NaCl.



#### 4.2.3 HBr, HCl, NaBr and NaCl modified TiO<sub>2</sub>

As shown in Figure 4-14, the initial hydrodynamic diameter of P25, HBr-P25 and HCl-P25 at 300 mg/L in SMZ solution was 300, 250 and 180 nm, respectively. They were stable in solution within 75 min. On the other hand, the initial hydrodynamic diameter of 300 mg/L NaBr-P25 and NaCl-P25 in SMZ solution was 1160 and 590 nm, respectively, as shown in Figure 4-15. NaCl-P25 kept stable within 120 min, NaBr-P25, however, had some change in the hydrodynamic diameter. The particles size of NaBr-P25 decreased from 1160 nm to about 900 nm, and then remained for 60 min.

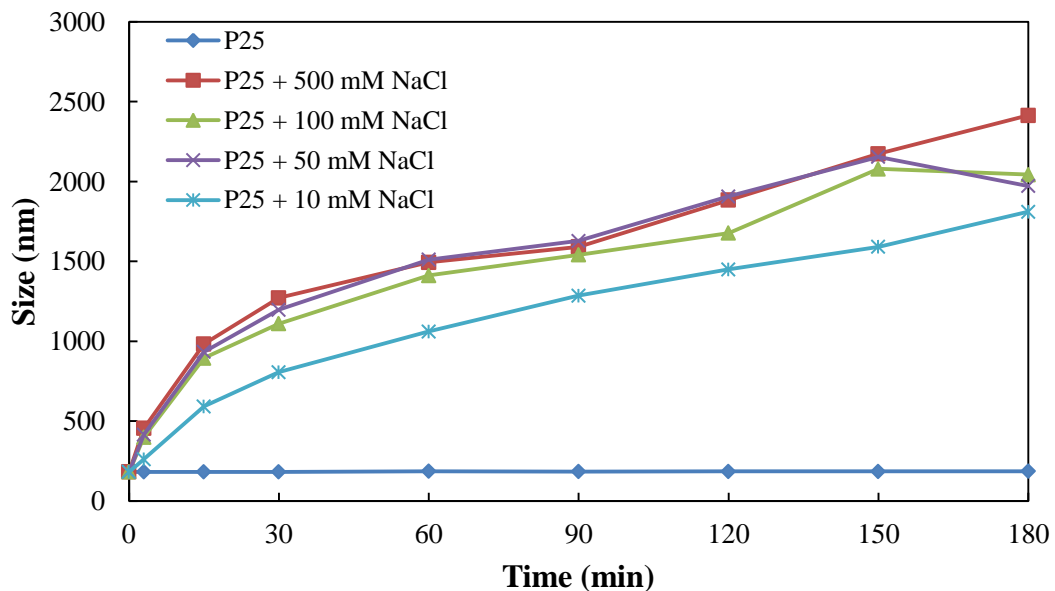


Figure 4-10. Aggregation kinetics of 10 mg/L P25 with different NaCl concentrations in 5 mg/L SMZ solutions.

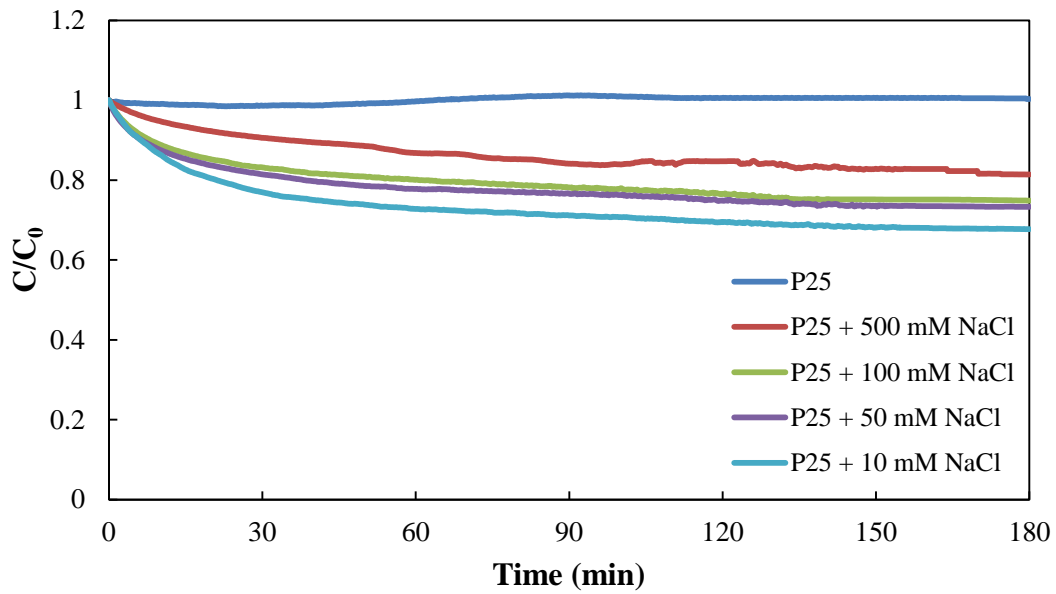


Figure 4-11. Sedimentation kinetics of P25 with different NaCl concentrations in SMZ solutions (P25: 10 mg/L; SMZ: 5mg/L).

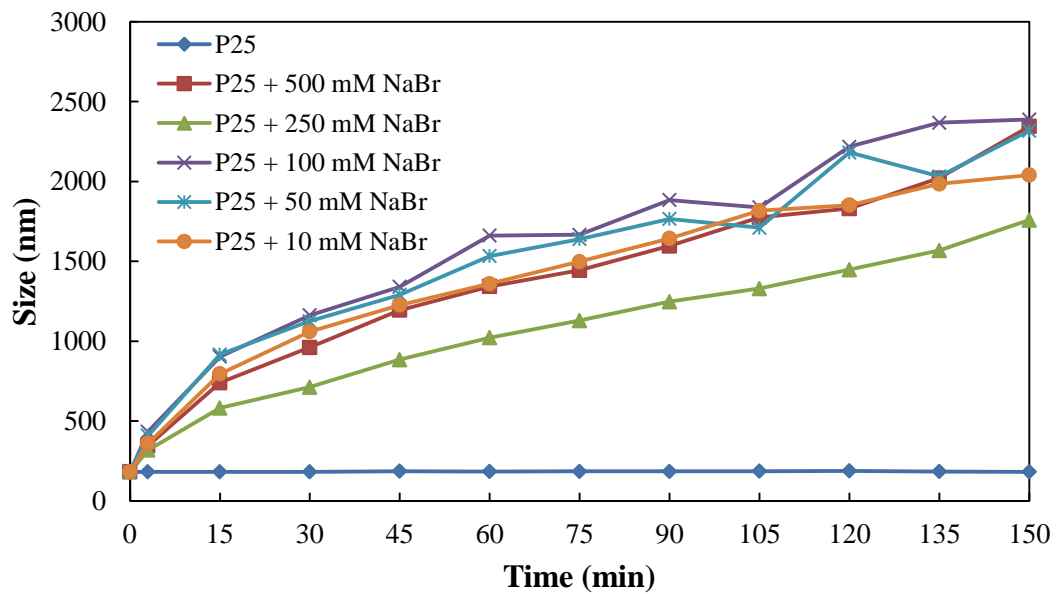


Figure 4-12. Aggregation kinetics of 10 mg/L P25 with different NaBr concentrations in 5 mg/L SMZ solutions.

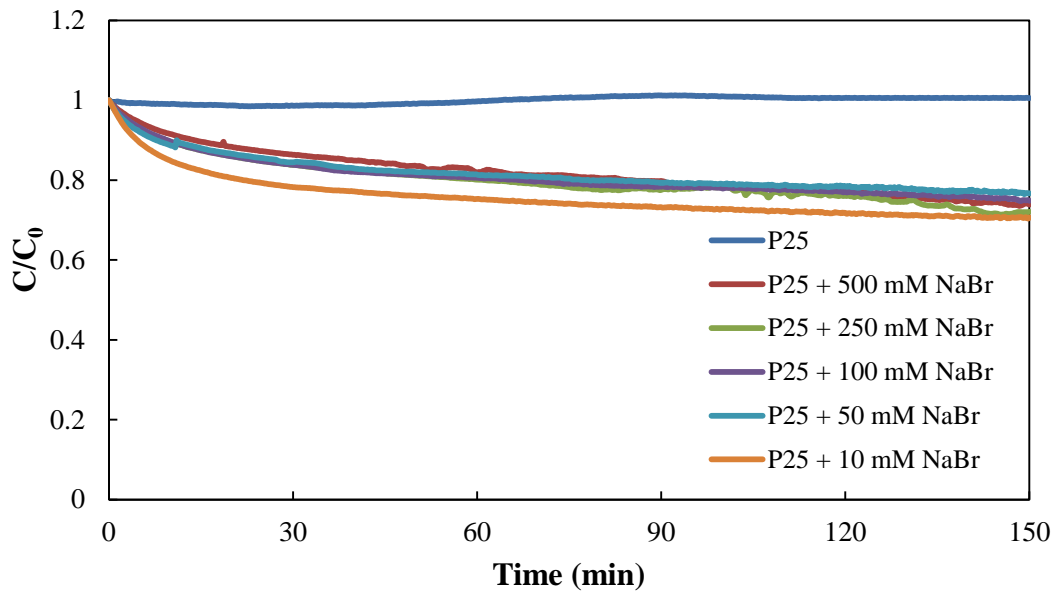


Figure 4-13. Sedimentation kinetics of 10 mg/L P25 with different NaBr concentrations in 5 mg/L SMZ solutions.

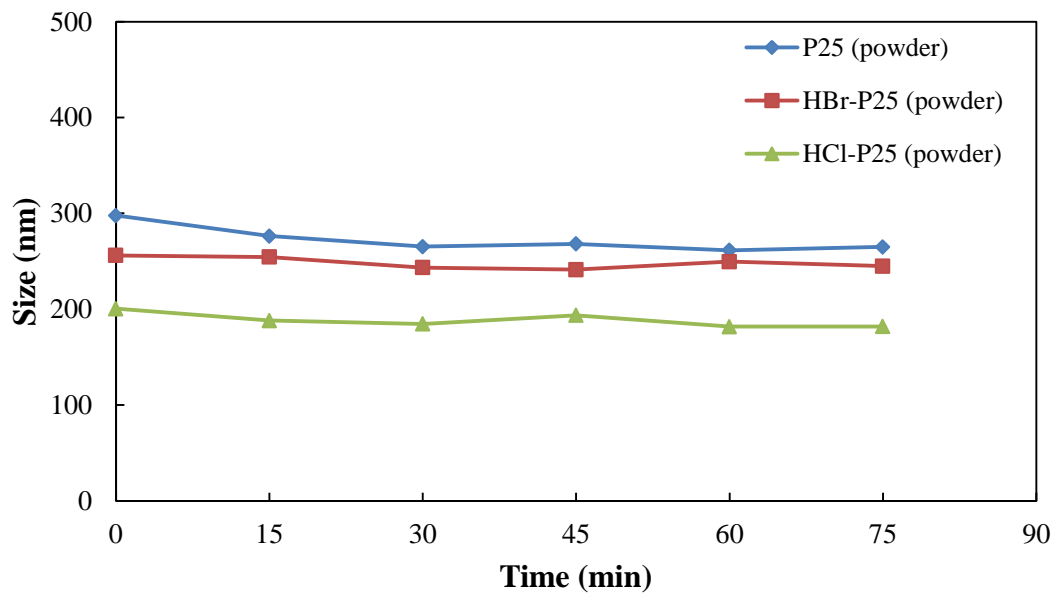


Figure 4-14. Aggregation kinetics of 300 mg/L photocatalysts in 5 mg/L SMZ solutions.

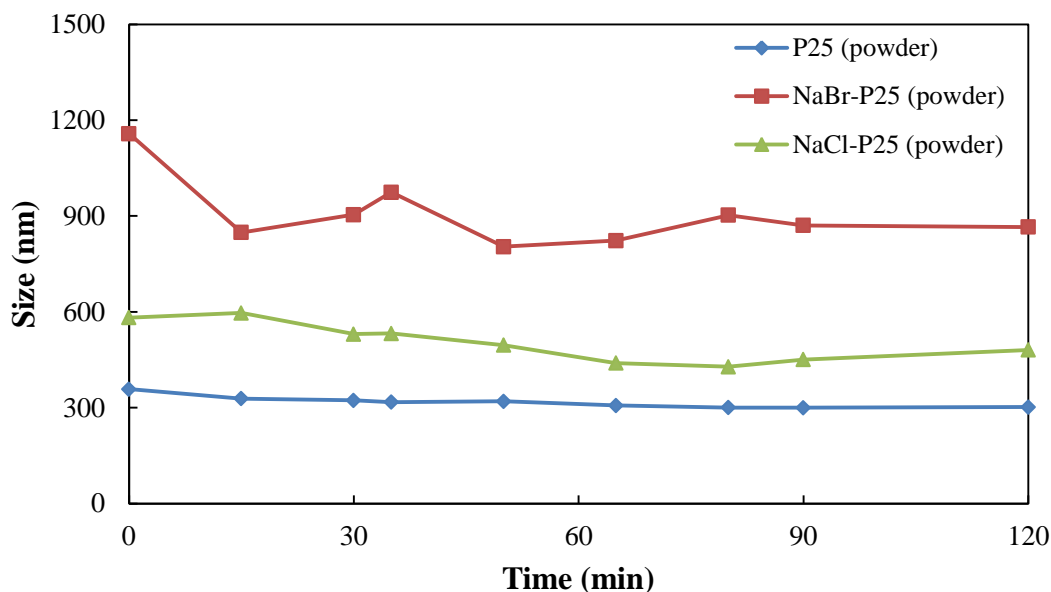


Figure 4-15. Aggregation kinetics of 300 mg/L photocatalysts in 5 mg/L SMZ solutions.

#### 4.2.4 The effect of NOM

Humic acid (HA), a major component of NOM and a typical representative of humic substances, may interact with  $\text{TiO}_2$  NPs via electrostatic attraction and ligand exchange (Yang et al., 2009). Its adsorption would increase the electrostatic repulsion and steric hindrance between individual nanoparticles, thereby enhancing their dispersion and stability (Chen et al., 2012). In this study, two kinds of HA, Leonardite humic acid (LHA) and Suwannee River humic acid (SRHA), were used to investigate the stable dispersion of P25 by HA.

Figure 4-16 and 4-17 showed that P25 exhibited good stability in both LHA and SRHA at tested concentrations, which was illustrated by their aggregate sizes remaining constant over 150 min. LHA and SRHA can drastically increase the stability of  $\text{TiO}_2$  NPs even in the presence of 100 mM NaBr due to the combined effect of increased electrostatic and steric repulsions. Previous study showed that at low pH, the surface charge was increased by the surface-adsorbed SRHA, leading to



increased electrostatic repulsions between TiO<sub>2</sub> NPs (Jayalath et al., 2018). Increased electrostatic repulsions increase stability of the NPs by minimizing the agglomeration. In the case of steric stabilization, HA molecules adsorbed or bound to the particle surface create a protecting network, which could prevent particles from aggregation (Segets et al., 2011).

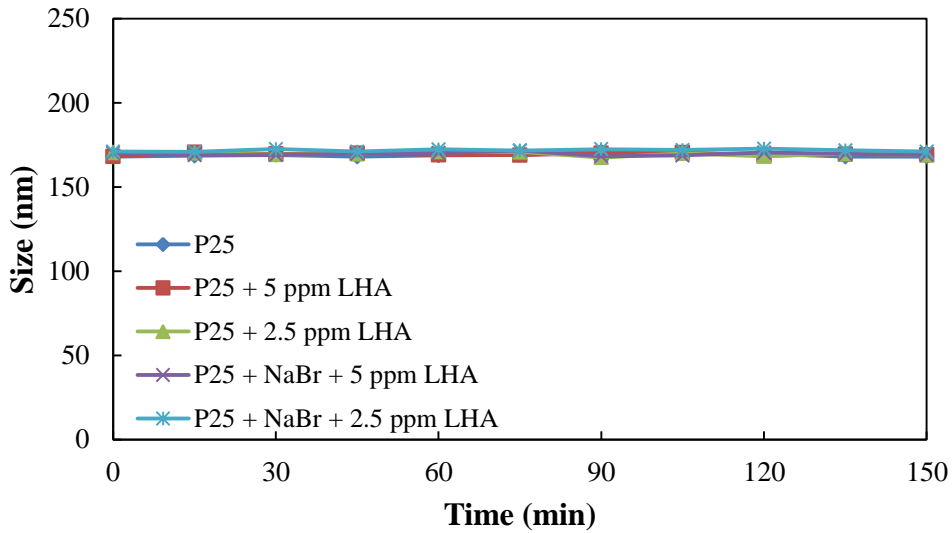


Figure 4-16. Aggregation kinetics of 10 mg/L P25 at 2.5 and 5 mg/L LHA with or without 100 mM NaBr in 5 mg/L SMZ solutions.

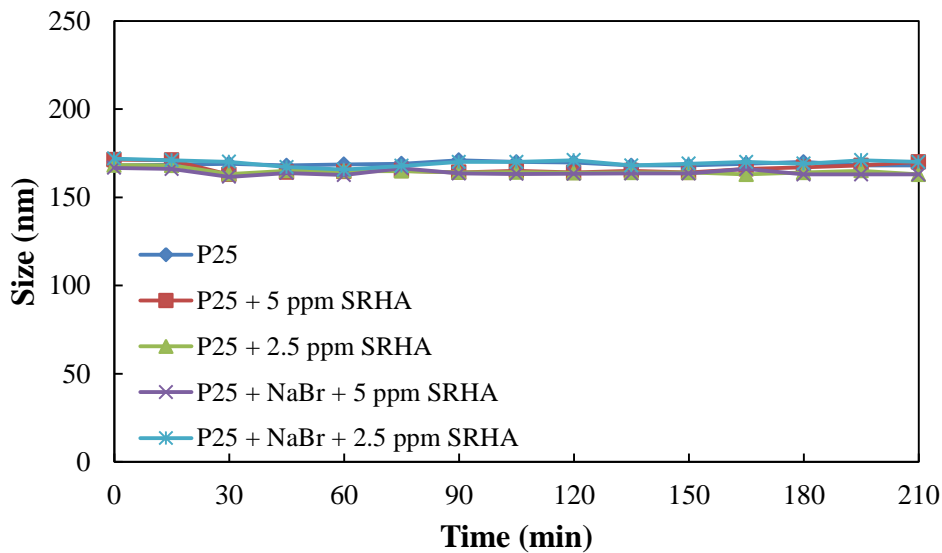


Figure 4-17. Aggregation kinetics of 10 mg/L P25 at 2.5 and 5 mg/L SRHA with or without 100 mM NaBr in 5 mg/L SMZ solutions.

## 4.3 Photocatalytic degradation of SMZ by TiO<sub>2</sub>

### 4.3.1 The effect of TiO<sub>2</sub> dosage on the removal of SMZ

SMZ absorbs light within the range between 240 and 310 nm (Abellán et al., 2009), which means that it cannot be assured if its degradation is due to the photocatalysis or due to the photolysis process, as shown in Figure 4-18. Therefore, for the photocatalytic degradation of SMZ, UV-A light ( $\lambda = 365$  nm) was used in the following experiment. The TiO<sub>2</sub> bandgap energy of 3.2 eV corresponds to photons with  $\lambda \leq 387.5$  nm, which is still longer than the wavelength we used ( $\lambda = 365$  nm).

The adsorption amount of organic compounds on the catalyst surface may influence the removal efficiency (Sojic et al., 2009). However, no adsorption of SMZ on TiO<sub>2</sub> in dark was found (Figure 4-19). The result revealed that the adsorption amount of SMZ was negligibly small after the system was balanced in the dark for 30 minutes.

The heterogeneous photocatalytic degradation usually increases with the photocatalyst concentration towards a limit at high catalyst concentrations. As shown in Figure 4-19, the positive effect of increasing TiO<sub>2</sub> dosage on the percentage of SMZ degradation was clearly indicated. The addition of more TiO<sub>2</sub> enhanced the removal efficiencies of SMZ. This could be attributed to the increasing light absorption by TiO<sub>2</sub> and the higher generation of reactive oxygen species (ROS) on active surface sites of TiO<sub>2</sub> (Abellán et al., 2009; Ding et al., 2013; Hu et al., 2007). Since the main objective was to evaluate the mechanisms of photocatalytic degradations of SMZ by P25 in the presence of NaBr or NaCl. Therefore, 10 mg/L P25 was selected for use in the following experiments.

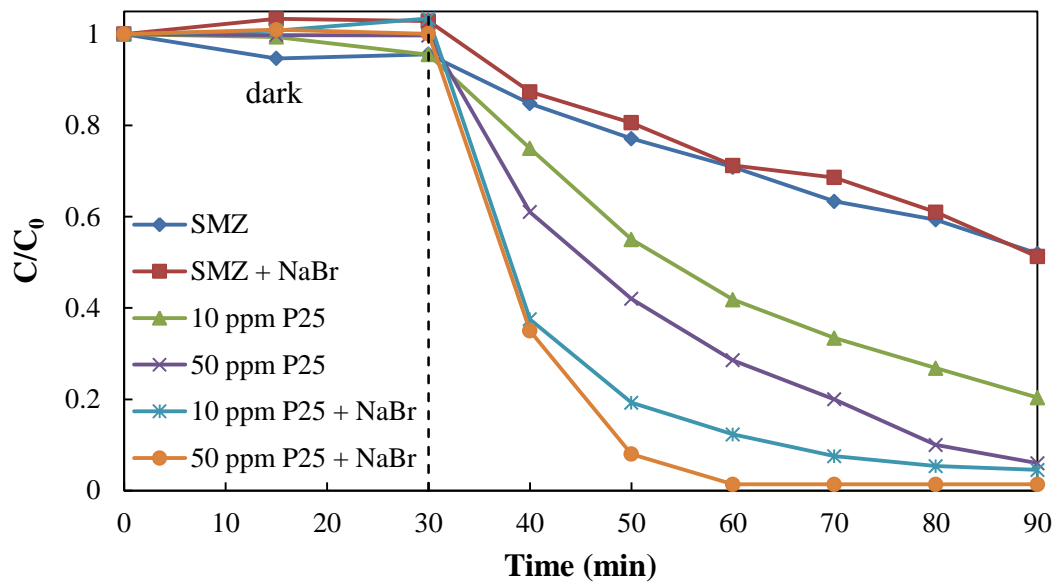


Figure 4-18. The photocatalytic degradation of SMZ by different concentrations of P25 under UV-C light. (UV light:  $\lambda = 253.7$  nm, 32W; SMZ: 5 mg/L)

Table 4-4. The pH and SMZ photodegradation rate constant of different concentrations of P25 under UV-C light.

pH	Before experiment	After experiment	Rate constant ( $\text{min}^{-1}$ )
SMZ	5.56	5.54	0.0103
SMZ + NaBr	5.34	5.10	0.0103
10 ppm P25	5.50	4.89	0.0262
50 ppm P25	5.41	5.24	0.0458
10 ppm P25 + NaBr	5.34	5.55	0.0569
50 ppm P25 + NaBr	5.31	5.05	0.144

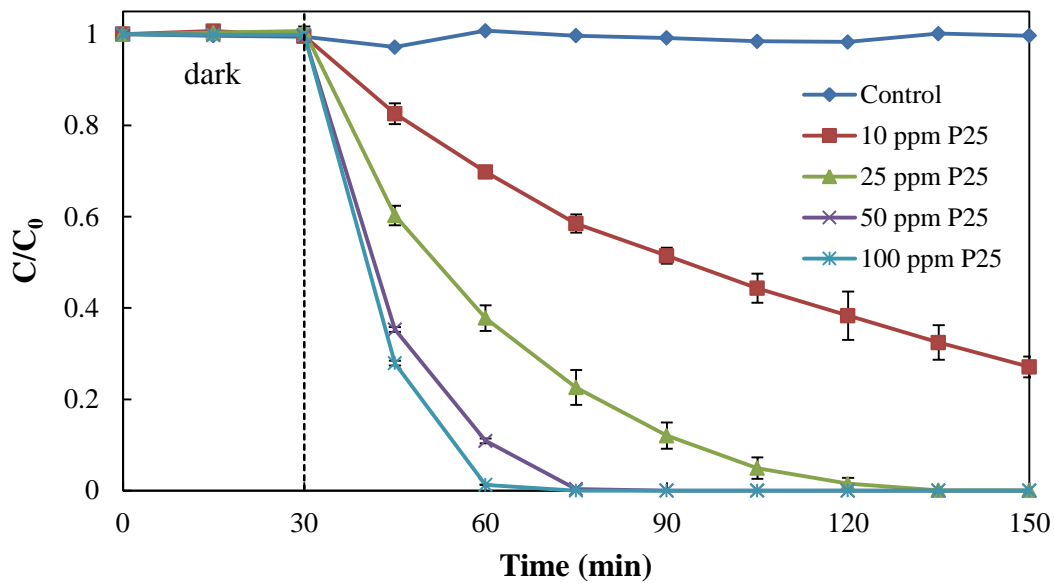


Figure 4-19. The photocatalytic degradation of SMZ by different concentrations of P25 under UV-A light. (UV light:  $\lambda = 365 \text{ nm}$ , 32W; SMZ: 5 mg/L)

Table 4-5. The pH and SMZ photodegradation rate constant of different concentrations of P25 under UV-A light.

pH	Before experiment	After experiment	Rate constant ( $\text{min}^{-1}$ )
SMZ	5.66	5.63	-
10 ppm P25	5.69	4.86	0.0106
25 ppm P25	5.82	4.67	0.0447
50 ppm P25	5.59	4.72	0.161
100 ppm P25	5.30	4.61	0.214

### 4.3.2 The effect of the initial SMZ concentration on photodegradation

The influence of the initial SMZ concentration on the photodegradation was studied with a P25 dosage of 10 mg/L. Figure 4-20 showed that the SMZ concentration had no obvious change when it was not irradiated by UV light. This

result indicates that SMZ would not adsorb to P25 particle surface within 150 min. Consequently, SMZ concentration change caused by adsorbing on TiO<sub>2</sub> particle surface during photodegradation can be ignored.

As observed in Figure 4-20, the degradation rate decreased as the concentration of SMZ increased from 0.5 mg/L to 10 mg/L. At a higher initial concentration, two factors could hinder the degradation of the SMZ. First, an increased amount of SMZ may occupy a greater number of TiO<sub>2</sub> active sites, which subsequently suppresses the generation of the oxidants and results in lower degradation rates. Secondly, a higher concentration of SMZ absorbs more photons, and consequently decreases the photons available to the active TiO<sub>2</sub>. Thus, a shortage of photons at the active TiO<sub>2</sub> surface essentially retards the degradation of SMZ at high initial concentrations. Hence, the overall reaction rate was lower with a higher initial SMZ concentration. This has been observed in many photochemical reactions where activation by photon absorption is typically the first step for the reaction (Guo et al., 2013).

#### **4.3.3 The effect of sodium halide concentration on the removal of SMZ**

Electrolytes are common in the environment and affect the particle size of nanoparticles in many studies. As a result, it is important to explore whether the particle size or salt concentration affects the degradation efficiency of organic compounds. This study aims to investigate the influence on SMZ photodegradation with aggregated TiO<sub>2</sub> NPs in the presence of halide ions.

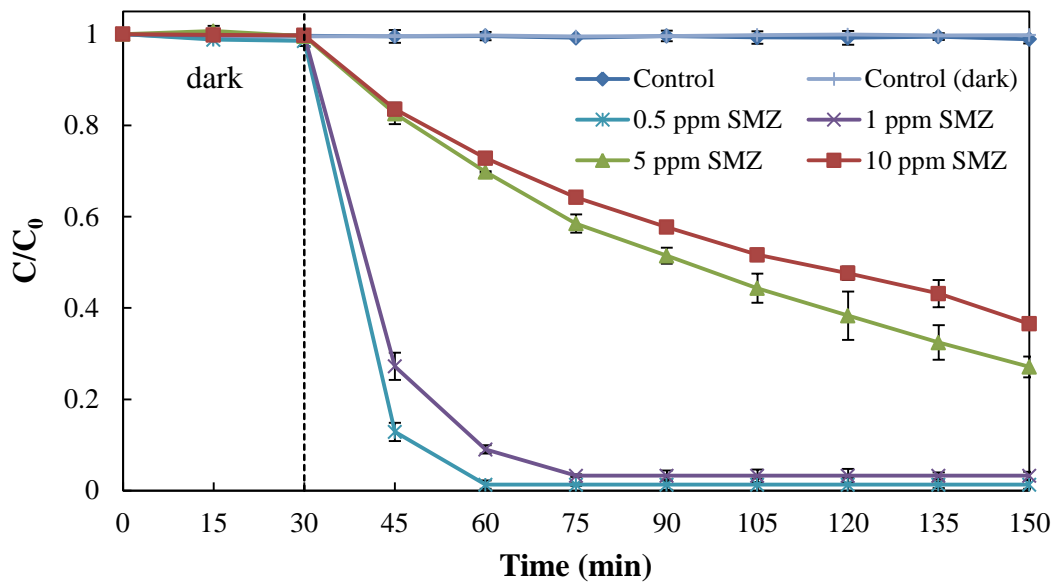


Figure 4-20. The photocatalytic degradation of different concentrations of SMZ by 10 mg/L P25 under UV light. (UV light:  $\lambda = 365 \text{ nm}$ , 32W)

Table 4-6. The pH and SMZ photodegradation rate constant of P25.

pH	Before experiment	After experiment	Rate constant ( $\text{min}^{-1}$ )
SMZ	5.55	5.68	-
SMZ (dark)	5.67	5.10	-
0.5 ppm SMZ + P25	5.80	5.73	0.00791
1 ppm SMZ + P25	5.70	5.31	0.0106
5 ppm SMZ + P25	5.29	4.86	0.0759
10 ppm SMZ + P25	5.35	4.91	0.144

#### 4.3.3.1 The effect of NaCl concentration on the removal of SMZ

The analysis of SMZ concentration in P25 suspensions at different NaCl concentrations in the dark was conducted. Figure 4-21 showed that the SMZ concentration had no significant change when it was not irradiated with UV light. This result indicates that SMZ would not adsorb to P25 particle surface within 30

min. Besides, from Figure 4-20, it is concluded that SMZ concentration change caused by adsorbing on TiO<sub>2</sub> particle surface during photodegradation is negligible.

Photodegradation kinetics of SMZ by 10 mg/L P25 at different NaCl concentrations is shown in Figure 4-21. In the blank experiment, when SMZ was irradiated with UV in the absence of P25, the change in SMZ concentration was found to be insignificant. The photocatalytic degradation efficiency of SMZ by P25 was 77% after UV light irradiation for 3 hr, and the rate constant was 0.0134 min<sup>-1</sup>. The SMZ degradation rate was reduced by the presence of NaCl under UV irradiation. This reduction enlarged as the chloride concentration was increased, which can be observed through comparing the rate constant, as shown in Figure 4-22 and Table 4-7. When there were halide salts in the solution, P25 NPs aggregated and became larger particle agglomerates (Figure 4-10 and 4-11), resulting in the decrease of surface area (Table 4-2) and active site on the surface, which reduced the photocatalytic performance of TiO<sub>2</sub> (Figure 4-23). Yang et al. (2005) reported that under certain conditions Cl<sup>-</sup> are able to scavenge active radicals and slow down the photodegradation. Moreover, Liang et al. (2008) also indicated that the rate of 2,3-DCP photodegradation by TiO<sub>2</sub> nanotube arrays decreased with an increased Cl<sup>-</sup> concentration significantly, which could be attributed to the competitive adsorption and the formation of less reactive radicals during the photocatalytic reaction. In general, aggregation has negative influence on the photocatalytic performance.

Considering the sedimentation of P25 with NaCl (Figure 4-11), the dosage of 7.5 mg/L P25 was performed to avoid the sedimentation effect. With the addition of 10 mM NaCl, the photodegradation kinetic seemed to be slightly faster than 7.5 mg/L P25. Some previous studies showed that the addition of Cl<sup>-</sup> could enhance photodegradation performance significantly (Iguchi et al., 2015; Krivec et al., 2014), but in this study, only the addition of 10 mM NaCl seemed to enhance the

photodegradation. Yuan et al. (2012) indicated that the chloride ion was found to have a dual effect on both the dye decoloration and mineralization in UV/TiO<sub>2</sub> system due to different mechanisms involved. Chloride ion has a higher affinity for the holes than •OH, and thus further inhibits the electron-hole pair recombination. As a result, the conduction band electrons and valence band holes can then migrate to catalyst surface and react chemisorbed O<sub>2</sub> or OH<sup>-</sup>/H<sub>2</sub>O molecules to generate reactive oxygen species (ROS), which can attack dye molecules and the degradation intermediates. Liu et al. (2009) also found that bisphenol A could be degraded by •Cl<sub>2</sub><sup>-</sup>, which was yielded from Cl<sup>-</sup> under simulated solar light irradiation. In this study, chloride ion has a negative effect on photodegradation of SMZ by P25, except for the addition of 10 mM NaCl.

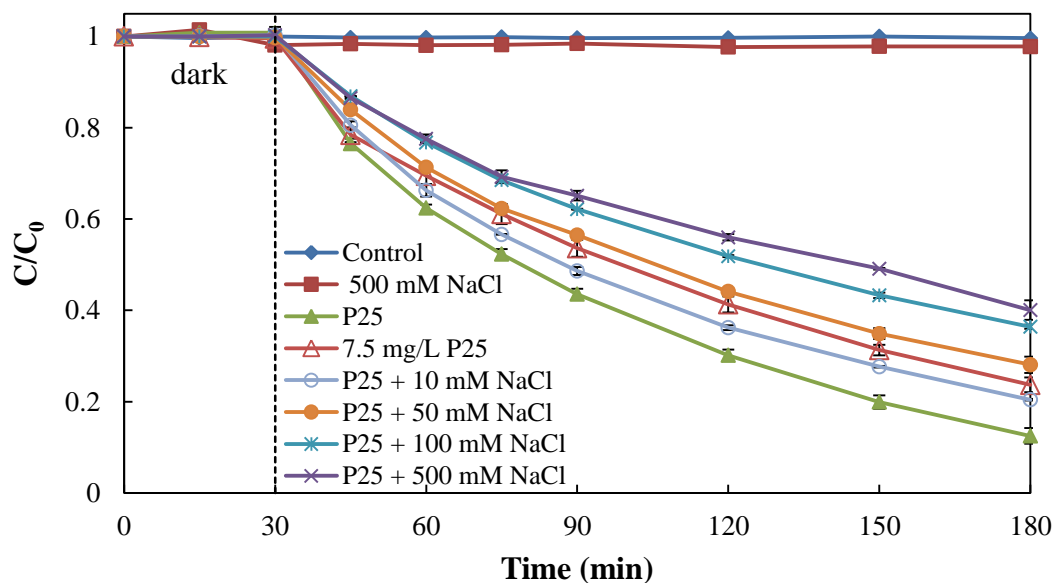


Figure 4-21. The photocatalytic degradation of 5 mg/L SMZ by 10 mg/L P25 at different NaCl concentrations under UV light. (UV light:  $\lambda = 365$  nm, 32W)



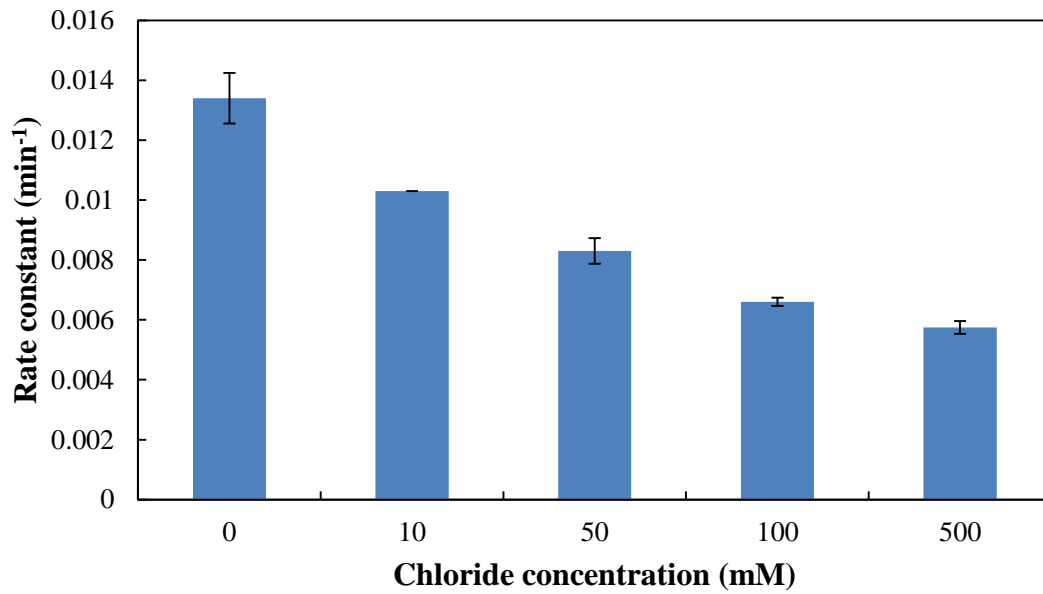


Figure 4-22. The relationship between SMZ degradation rate constant and NaCl concentrations. (SMZ: 5 mg/L; P25: 10 mg/L)

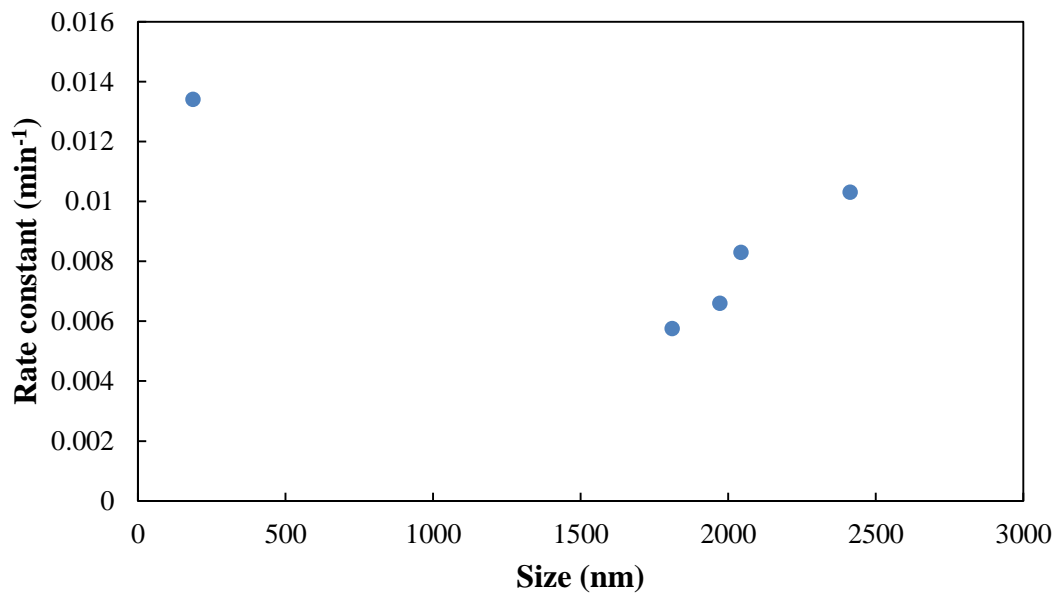


Figure 4-23. The relationship between SMZ degradation rate constant and P25 particle size in the presence of different concentrations of NaCl.

Table 4-7. The pH, SMZ photodegradation rate constant, and final particle size at different concentrations of NaCl.

NaCl concentration (mM)	Initial pH	Final pH	Size (nm)	Rate constant (min <sup>-1</sup> )
Control (w/o P25)	5.66	5.63	-	-
0	5.50	5.10	186	0.0134
0 (7.5 mg/L)	5.08	4.91	173	0.00921
10	5.38	4.81	1810	0.0103
50	5.39	4.89	1972	0.00832
100	5.38	4.97	2043	0.00665
500	4.92	4.89	2413	0.0058

#### 4.3.3.2 The effect of NaBr concentration on the removal of SMZ

The effect of NaBr concentration on the degradation of SMZ solution by P25 was investigated under UV irradiation (Figure 4-24). In the control experiment, when SMZ was irradiated with UV light in the absence of P25, the changes in SMZ concentration was insignificant, indicating that no adsorption of SMZ on TiO<sub>2</sub> in dark. The photocatalytic degradation efficiency of SMZ by P25 was 72% after UV light irradiation for 2 hr, and the rate constant was 0.0104 min<sup>-1</sup>.

When there was NaBr in the solution, TiO<sub>2</sub> aggregated and became larger particle agglomerates (Figure 4-12 and 4-13), resulting in the decrease of surface area (Table 4-1) and active site on the surface. However, the photodegradation rate of SMZ by TiO<sub>2</sub> with the addition of NaBr increased instead of decreasing. Figure 4-24 illustrated that the SMZ degradation rate was accelerated by the presence of NaBr under UV irradiation. This enhancement enlarged as the bromide concentration was increased, but lessened when the bromide concentration exceeded 100 mM. With the addition of 100 mM NaBr, the photodegradation efficiency was 95% after 45 min, and reached equilibrium of 99% removal efficiency at 75 min. The photodegradation rate

constant of P25 was  $0.0104 \text{ min}^{-1}$ , increasing to  $0.0636 \text{ min}^{-1}$  with the addition of 100 mM NaBr, as shown in Figure 4-25 and Table 4-8.

The relationship between SMZ degradation rate constant and P25 particle size is shown in Figure 4-26. It can be observed that there is no good correlation between SMZ degradation rate constant and P25 agglomerate particle size, implying that the antenna effect has insignificant influence on SMZ degradation in the presence of different concentrations of bromide ions. The SMZ degradation rate constants at different NaBr concentrations with different P25 particle sizes are compared in Table 4-8. In view of this, the main factor affecting SMZ degradation rate constant may be NaBr concentration instead of  $\text{TiO}_2$  particle size. Moreover, Figure 4-24 showed that the increase of SMZ degradation rate was significant even in low concentration of NaBr (10 mM) with 96% removal at 2 hr. Therefore, it may be possible that the increase of SMZ degradation rate was related to the presence of bromide ions. The enhanced degradation of SMZ in the UV/ $\text{TiO}_2$  process could be achieved by reactive bromine species generated from bromide ions. According to previous studies, the photocatalytic production of high concentration of bromide radicals is possible because these radicals can form stable di-halide radical anions ( $\text{Br}_2^-$ ) in the presence of  $\text{Br}^-$  (Cheng & Bakac, 2008; Merenyi & Lind, 1994). Wu et al. (2016) also reported that the addition of NaBr to photoactivated  $\text{TiO}_2$  (P25) potentiates the killing of Gram-positive, Gram-negative bacteria and fungi by up to three logs due to the formation of reactive bromine species from  $\text{Br}^-$  oxidation.

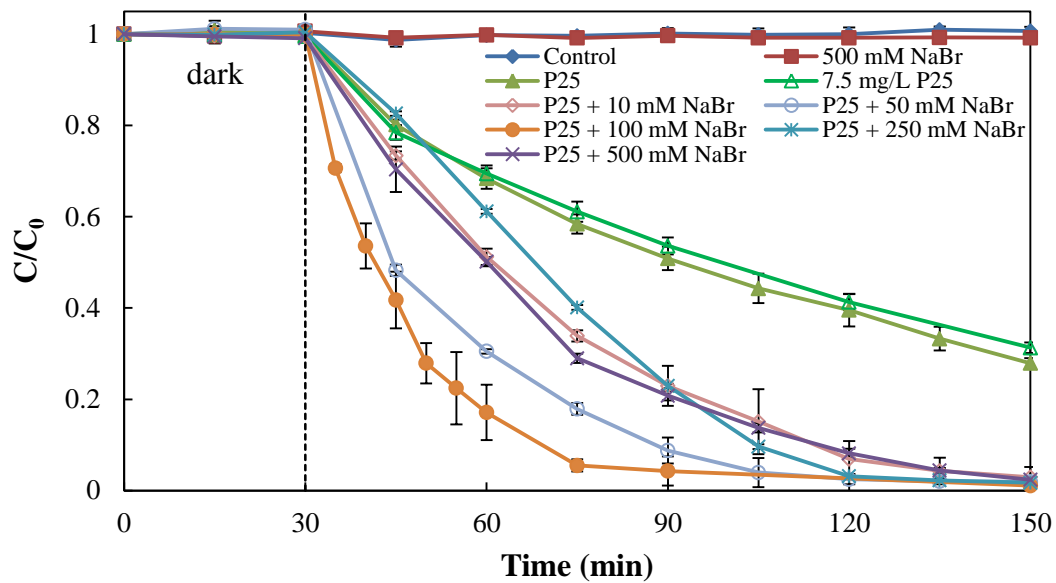


Figure 4-24. The photocatalytic degradation of 5 mg/L SMZ by 10 mg/L P25 at different NaBr concentrations under UV light. (UV light:  $\lambda = 365 \text{ nm}$ , 32W)

Vikesland et al. (2013) indicated that free bromine species are a much more effective halogenating agent than free chlorine species. Moreover, the oxidation potential of chloride ion is higher than bromide ion, indicating that reactive chlorine species is more difficultly formed than reactive bromine species. That may be the reason why bromide ion has more significant enhancement effect than chloride ion on photocatalytic degradation of SMZ. Although in theory the reaction of  $\bullet\text{OH}$  with chloride may also generate chlorine radicals during UV processes (G. G. Jayson et al., 1973; Liao et al., 2001), such effects generate less reactive chlorine species and appear to be not strong enough to increase SMZ photodegradation rates under the conditions of this study.

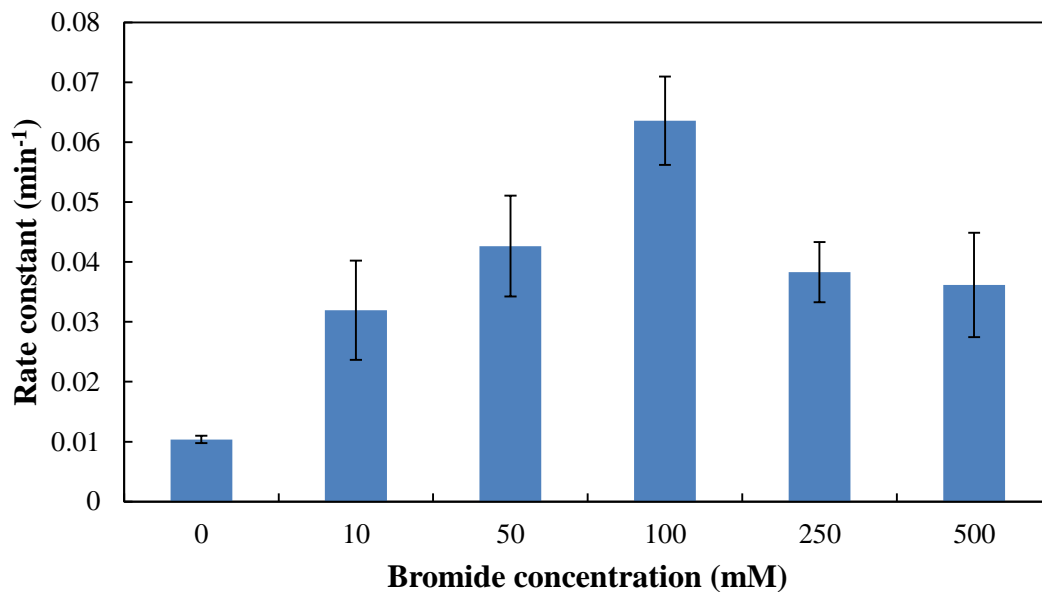


Figure 4-25. The relationship between SMZ degradation rate constant and NaBr concentration with 5 mg/L SMZ and 10 mg/L P25.

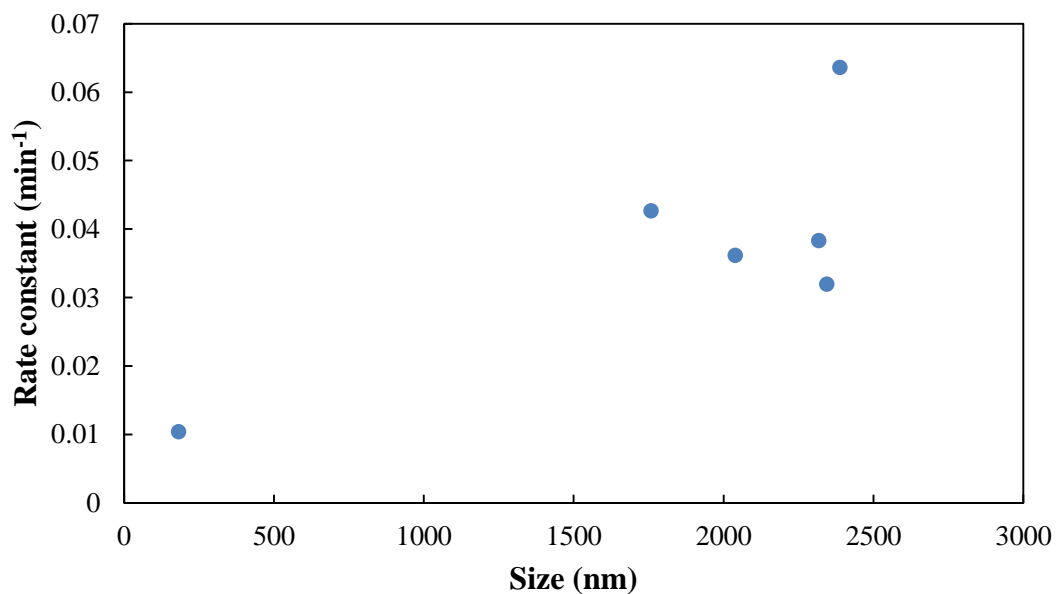


Figure 4-26. The relationship between SMZ degradation rate constant and P25 particle size in the presence of different concentrations of NaBr.

Table 4-8. The pH, SMZ photodegradation rate constant and final particle size at different concentrations of NaBr.

NaBr concentration (mM)	Initial pH	Final pH	Size (nm)	Rate constant (min <sup>-1</sup> )
Control (w/o P25)	5.66	5.63	-	-
0	5.50	5.10	182	0.0104
10	5.37	5.61	2040	0.0320
50	5.37	5.52	2318	0.0426
100	5.31	5.55	2388	0.0636
250	5.45	5.60	1758	0.0383
500	5.52	5.72	2345	0.0362

#### 4.3.3.3 The effect of pH on the removal of SMZ in the presence of 100 mM Br<sup>-</sup>

The degradation rate may vary with the pH due to the ionic nature of the target compound, the surface properties of the photocatalyst, and the type of intermediates arisen along the reaction. SMZ, the target compound in this study, has got two protonated states, varying with pH. The different ionic states of the substances have a remarkable effect on its reactivity, and the values of the corresponding  $pK_a$ 's are important for the elucidation of their photochemical behavior according to the pH. The  $pK_a$  values of SMZ are:  $pK_{a1} = 1.83$  and  $pK_{a2} = 5.57$ , which means that the sulfamethoxazole has a cationic form at  $pH < 1.83$ , and an anionic form at  $pH > 5.57$  (Dodd & Huang, 2004; Lin et al., 1997). These forms can be related to the positive charge of  $TiO_2$  at  $pH < 6$  and negative at  $pH > 6$ . Since the  $TiO_2$  has amphoteric nature, it has a point of zero charge between 5.6 and 6.8 (Kosmulski, 2011). Xekoukoulotakis et al. (2011) studied the effect of pH on the degradation of SMZ with P25, and reported that the photodegradation of 10 mg/L SMZ by 500 mg/L P25 was faster at around pH 4 than at around pH 7.5 in ultra-pure water under UVA light

irradiation. Therefore, a series of experiments were carried out to study the influence of the pH on the process in the presence of 100 mM Br<sup>-</sup>. The initial pH was adjusted with 0.05 N NaOH and 0.1 N HBr, and the rest of parameters remained constant.

Figure 4-27 showed the photocatalytic degradation of 5 mg/L SMZ by 10 mg/L P25 with NaBr at acidic pH under UV light. Acidic pH was adjusted by HBr, and the concentration of Br<sup>-</sup> (NaBr and HBr) was fixed at 100 mM. It could be observed that the degradation rate at pH 4 was as fast as original pH (pH 5.5). When the reaction solution became more acidic (pH 3 and 2.5), the degradation kinetics became slower, but still faster than pure P25. It could be assumed that at acidic pH, Br<sub>2</sub> generated from Br<sup>-</sup> in the UV/TiO<sub>2</sub> system would vaporize, and thus the enhancement lessened compared to the degradation at original pH.

On the other hand, in neutral and alkaline system, the photocatalytic degradation of SMZ was slightly inhibited with increasing pH, as shown in Figure 4-28. However, the degradation of SMZ by P25 with 100 mM Br<sup>-</sup> at alkaline pH was still faster than pure P25. At neutral and alkaline pH, both SMZ and P25 surface are negatively charged, resulting in the enhanced repulsion between them. Therefore, the photo-adsorption of SMZ onto P25 surface is expected to be reduced (Xekoukoulotakis et al., 2011). This may explain the decreased photocatalytic activity, compared to original pH, observed at neutral and alkaline pH.

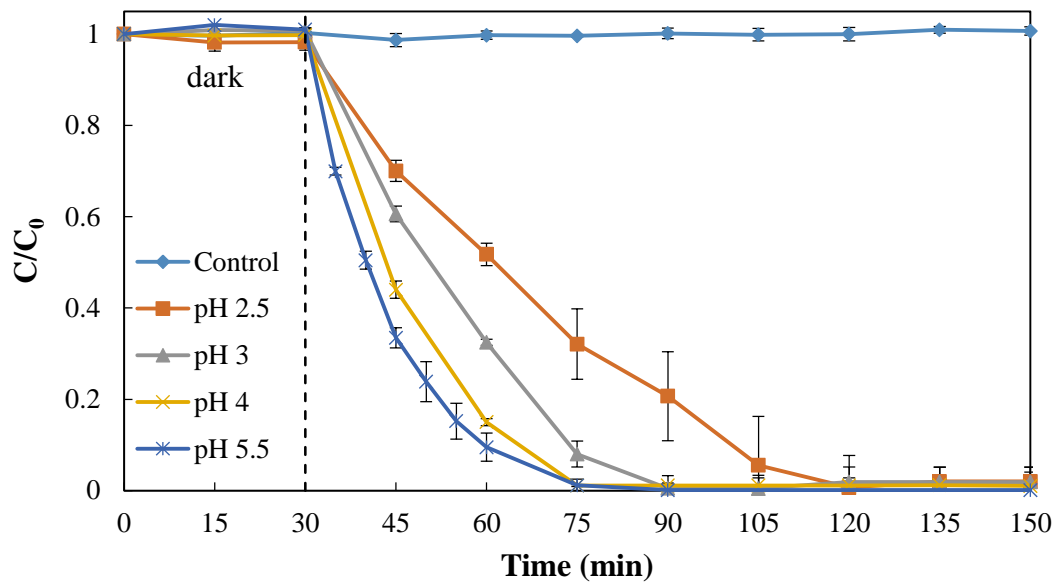


Figure 4-27. The photocatalytic degradation of 5 mg/L SMZ by 10 mg/L P25 with NaBr at different pH under UV light. HBr and NaOH are used for adjusting pH, and the concentration of Br<sup>-</sup> ion is fixed at 100 mM. (UV light:  $\lambda = 365$  nm, 32W) (Original pH: 5.5)

Table 4-9. The pH measurements and rate constants of the degradation of SMZ in the presence of 100 mM Br<sup>-</sup> at acidic pH.

pH	Before experiment	After experiment	Rate constant (min <sup>-1</sup> )
SMZ	5.48	5.69	-
pH 2.5	2.48	2.70	0.0271
pH 3	3.09	3.41	0.0553
pH 4	4.16	4.49	0.0671
pH 5.5	5.50	5.15	0.0960



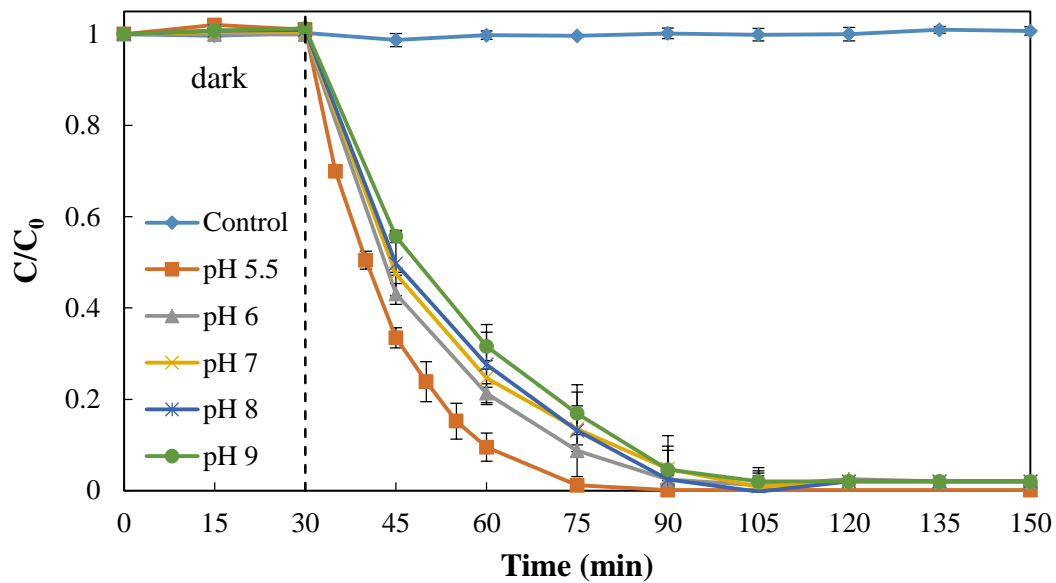


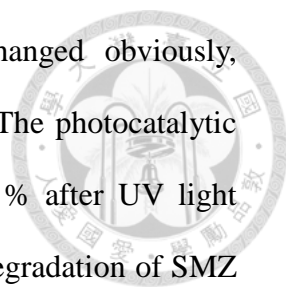
Figure 4-28. The photocatalytic degradation of 5 mg/L SMZ by 10 mg/L P25 with NaBr at different pH under UV light. HBr and NaOH are used for adjusting pH, and the concentration of Br<sup>-</sup> ion is fixed at 100 mM. (UV light:  $\lambda = 365$  nm, 32W) (Original pH: 5.5)

Table 4-10. The pH measurements and rate constants of the degradation of SMZ in the presence of 100 mM Br<sup>-</sup> at alkaline pH.

pH	Before experiment	After experiment	Rate constant (min <sup>-1</sup> )
pH 5.5	5.46	5.62	0.0960
pH 6	5.93	6.02	0.0602
pH 7	7.12	6.95	0.0600
pH 8.5	8.88	7.41	0.0527
pH 9	8.93	7.38	0.0504

#### 4.3.4 Photocatalytic degradation of SMZ by surface modified TiO<sub>2</sub>

The effect of surface modified P25 on the degradation of SMZ solution was investigated under UV irradiation. The results were shown in Figure 4-29. In the



absence of photocatalysts, the SMZ concentration was not changed obviously, indicating that no adsorption of SMZ on P25 in dark was found. The photocatalytic degradation efficiency of 5 mg/L SMZ by 0.3 g/L P25 was 99 % after UV light irradiation for 30 min. Compared to pure P25, the photocatalytic degradation of SMZ with HCl-P25 was slightly inhibited. As for the effect of HBr-P25, the photodegradation rate constant increased to  $0.511 \text{ min}^{-1}$ , which was about 3 times greater than that of P25, as shown in Figure 4-29 and Table 4-11. This could indicate that surface bromination of P25 can enhance the photodegradation process under an acidic condition. The pretreatment introduced bromide anion groups into P25 surface structure. Under photocatalytic conditions, these bromide groups could be converted, via photogenerated hole ( $h^+$ ) attack, into bromine radicals, which could then react with adsorbed hydrocarbon species (e.g., via hydrogen abstraction), potentially producing rate enhancements. The increase of photodegradation rate by HBr-P25 also implied that the surface reaction has significant effect on the enhancement resulting from the addition of NaBr (Figure 4-24).

As for NaBr-P25 and NaCl-P25, they both had reduced effect on the photodegradation of SMZ, as shown in Figure 4-30 and Table 4-12. This could be explained that Br and Cl may not decorate on the surface very well. Seen from Table 4-13, the IC results showed that the initial released  $\text{Br}^-$  and  $\text{Cl}^-$  concentration of NaBr-P25 and NaCl-P25 were much greater than those of HBr-P25 and HCl-P25, respectively. If all the solutions, including HBr, HCl, NaBr and NaCl, we added to P25 powder introduced all Br or Cl onto P25 surface in the pretreatment process, the residual Br or Cl on the surface of HBr-P25, HCl-P25, NaBr or NaCl was 26.89%, 12.12 %, 33.84%, and 19.14 %, respectively, after abstracting the released ions. However, these were calculated residual contents. In fact, the real ratio of Br or Cl decorated on the surface still remained unclear. Moreover, after photocatalytic

degradation process, the concentrations of  $\text{Br}^-$  and  $\text{Cl}^-$  in the solution were almost the same for all the samples, indicating that the residual Br or Cl was firmly decorated on the surface. On the other hand, from Table 4-3, it could be observed that the BET surface area values of HBr-P25 and HCl-P25 were  $52.16 \text{ m}^2/\text{g}$  and  $50.33 \text{ m}^2/\text{g}$ , respectively, which were similar to that of P25 ( $54.99 \text{ m}^2/\text{g}$ ). As for NaBr-P25 and NaCl-P25, their BET surface area values were  $34.48 \text{ m}^2/\text{g}$  and  $43.30 \text{ m}^2/\text{g}$ , respectively, which were lower than HBr-P25 and HCl-P25. Therefore, NaBr-P25 and NaCl-P25 had reduced photocatalytic performances than HBr-P25 and HCl-P25.

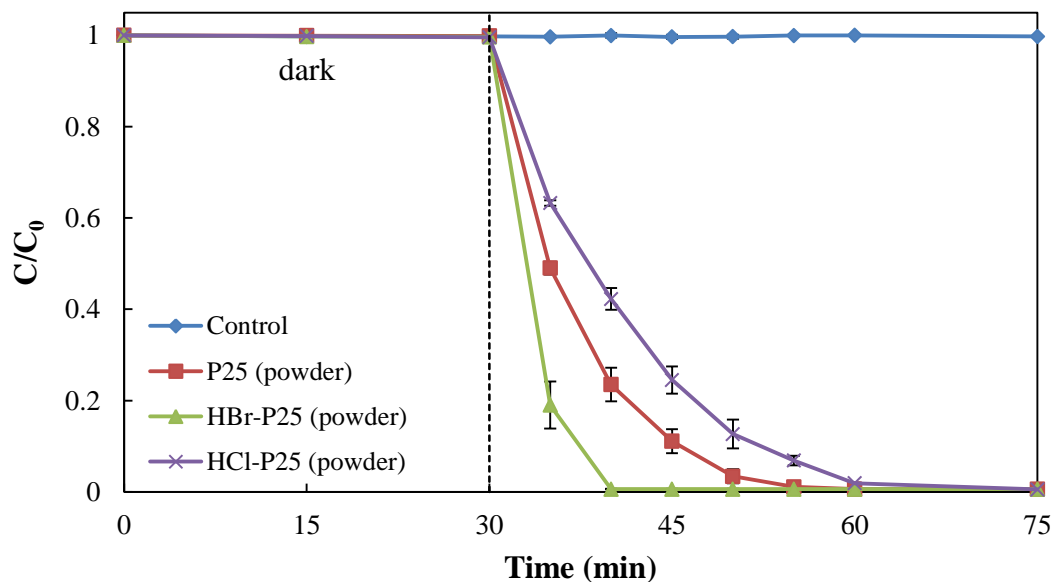


Figure 4-29. The photocatalytic degradation of 5 mg/L SMZ by 0.3 g/L P25, HBr-P25 and HCl-P25 under UV light.

Table 4-11. The pH and SMZ photodegradation rate constant of P25, HBr-P25 and HCl-P25 powder.

pH	Before experiment	After experiment	Rate constant ( $\text{min}^{-1}$ )
SMZ	5.60	5.64	-
P25 (powder)	5.16	4.76	0.178
HBr-P25 (powder)	3.92	3.90	0.511
HCl-P25 (powder)	4.52	4.40	0.125

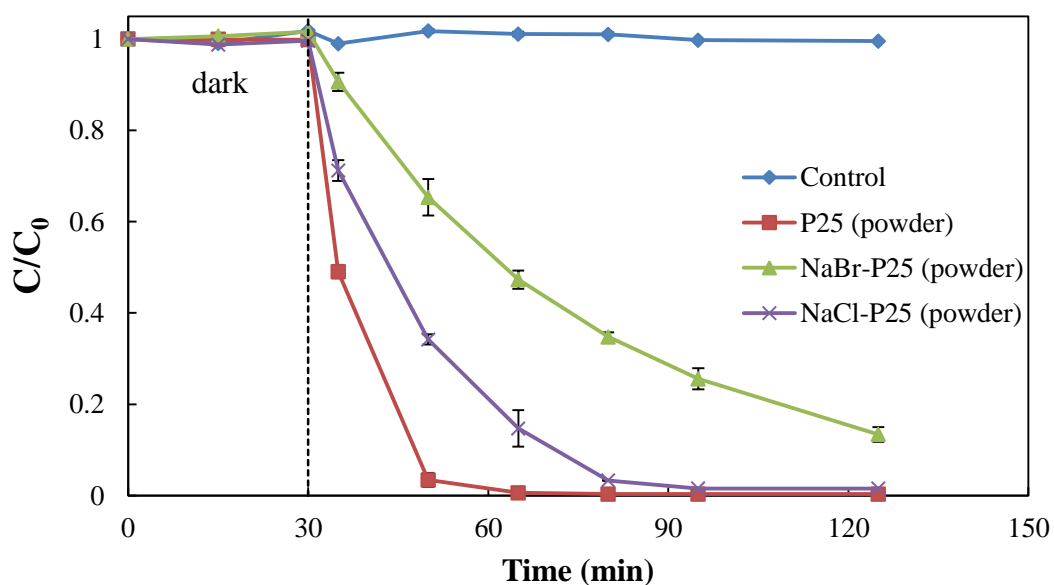


Figure 4-30. The photocatalytic degradation of 5 mg/L SMZ by 0.3 g/L P25, NaBr-P25 and NaCl-P25 under UV light.

Table 4-12. The pH and SMZ photodegradation rate constant of P25, NaBr-P25 and NaCl-P25 powder.

pH	Before experiment	After experiment	Rate constant ( $\text{min}^{-1}$ )
SMZ	5.46	5.52	
P25 (powder)	5.18	4.65	0.178
NaBr-P25 (powder)	5.27	5.24	0.0211
NaCl-P25 (powder)	5.81	6.15	0.0650

Table 4-13. The released halide ions in solutions from HBr-P25, HCl-P25, NaBr-P25 and NaCl-P25 powder before and after photodegradation experiments detected by IC. ( $[\text{Br}^-]_0$  and  $[\text{Cl}^-]_0$ : the concentrations of halide ions before the photodegradation experiments)

	$[\text{Br}^-]_0$ (mg/L)	$[\text{Br}^-]$ (mg/L)		$[\text{Cl}^-]_0$ (mg/L)	$[\text{Cl}^-]$ (mg/L)
HBr-P25	12.70	13.37	HCl-P25	4.75	5.59
NaBr-P25	68.06	64.30	NaCl-P25	50.73	48.23

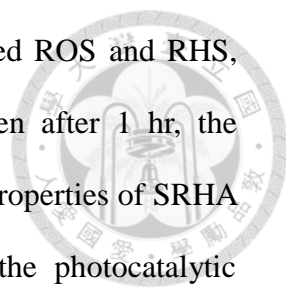
#### 4.3.5 The effect of NOM on the removal of SMZ

Natural organic matter (NOM) is often considered to be the most important non-target water constituent that affects photocatalytic processes because of its capacity to interfere with adsorption of the target compounds to  $\text{TiO}_2$  surfaces, absorb photons, scavenge  $\cdot\text{OH}$  and other reactive species including  $\text{Br}_2$  and  $\text{HOBr}$ , and generate photochemical reactive intermediates which can also react with the target pollutants. As an important fraction of NOM, humic acid (HA) is ubiquitously present in both surface water sources and wastewater treatment plant secondary effluent.

Therefore, we investigated the effect of two different HA, Leonardite humic acid (LHA) and Suwannee river humic acid (SRHA), on the removal of SMZ by P25 with or without 100 mM NaBr.

As shown in Figure 4-31, with the addition of 2.5 and 5 mg/L LHA, the photodegradation of SMZ by P25 was obviously inhibited. However, in the system of P25 containing 100 mM NaBr with the addition of LHA, the degradation rate of SMZ was still faster than pure P25 although it decreased with the addition of LHA as compared to that with P25 and NaBr. HA can play two contrasting roles during the photochemical reaction process. On the one hand, HA may inhibit the photodegradation of target compounds due to competition for the light energy and reactive species, and shielding target compounds from irradiation and reactive species. On the other hand, HA can act as a photosensitizer to induce generation of radical species and promote the degradation of target compounds. A plausible explanation of the inhibition in this experiment would be that the inhibitory effects of LHA outweighed the promoting effects, and thus the reaction rate decreased. The evidence is that the inhibition increased with the increase of LHA (Figure 4-31).

Figure 4-32 presented the photocatalytic degradation of 5 mg/L SMZ by 10 mg/L P25 with 100 mM NaBr and SRHA under UV light. With the addition of increasing concentration of SRHA (2.5 and 5 mg/L), the photodegradation rate of SMZ by P25 was decreased, consistent with previous study (Hu et al., 2007). Besides, the degradation kinetic pattern shifted from “log-tail” to “shoulder-log”, suggesting that there was a time requirement for the degradation of SMZ due the competition of reactive oxygen species (ROS) by SRHA. In the system of P25 containing 100 mM NaBr with the addition of SRHA, the photodegradation of SMZ was at first inhibited, and then increased compared to the P25 only system. The degradation kinetic pattern also shifted from “log-tail” to “shoulder-log”. This phenomenon could be assumed



that during the photocatalytic degradation, SRHA at first consumed ROS and RBS, resulting in the decrease of the SMZ photodegradation, and then after 1 hr, the weakened inhibition of SRHA resulting from the changed surface properties of SRHA made the enhancement by reactive bromine species dominate the photocatalytic reaction. Westerhoff et al. (2004) reported that bromine reacted with NOM on the order of seconds, and the halogen consumption exhibited two reaction stages: (1) rapid initial consumption followed by (2) slower consumption. They also indicated that the cross-over between reaction stages occurred  $< 15$  s for bromine. With the increase of SRHA to 5 mg/L (Figure 4-32), the cross-over time extended to 2 hr.

The different effects on photocatalytic performance resulting from LHA and SRHA may cause by the difference of HA structures. In Table 4-13, some selected characteristic of LHA and SRHA was listed. According to Table 4-13, LHA has fewer carboxylic and phenolic groups than SRHA but much more aromatic carbon (Hakim & Kobayashi, 2018; Ritchie & Perdue, 2003). Hakim and Kobayashi (2018) also reported that LHA is more hydrophobic than SRHA. Under UV light irradiation,  $\text{Br}^-$  reacts with photogenerated holes and  $\bullet\text{OH}$  on P25 surface, and forms reactive bromine species (RBS) which have been reported to preferentially react with electron-rich moieties. Therefore, LHA, which has higher electron-rich moieties than SRHA, could be attacked more by RBS and then result in a larger inhibition on SMZ degradation. This is consistent with the result reported by Criquet et al.(2015), indicating that the electrophilic aromatic substitution (% Br-incorporation) for the reaction of bromine with LHA was slightly higher than SRHA.

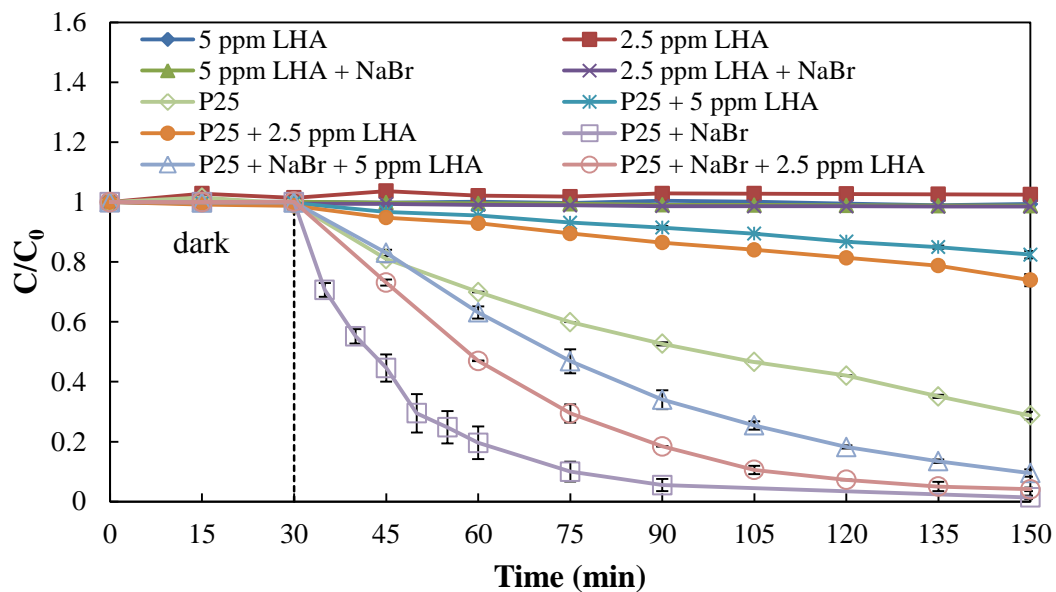


Figure 4-31. The photocatalytic degradation of 5 mg/L SMZ by 10 mg/L P25 with 100 mM NaBr and LHA under UV light. (UV light:  $\lambda = 365$  nm, 32W)

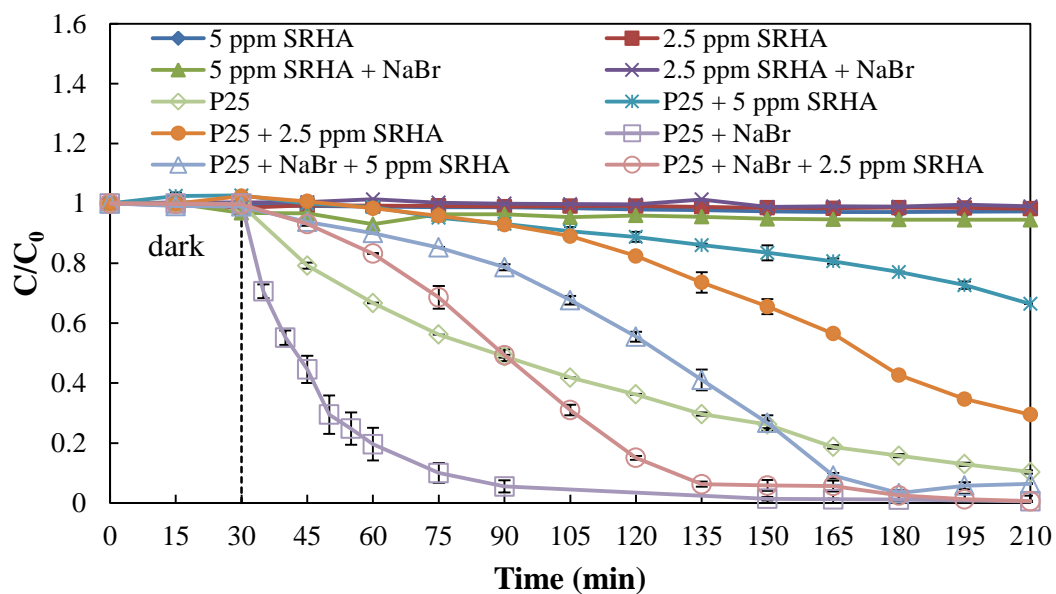


Figure 4-32. The photocatalytic degradation of 5 mg/L SMZ by 10 mg/L P25 with 100 mM NaBr and SRHA under UV light. (UV light:  $\lambda = 365$  nm, 32W)



Table 4-14. The pH and SMZ photodegradation rate constant of P25 with different concentrations of LHA in the presence of 100 mM NaBr.

pH	Before experiment	After experiment	Rate constant (min <sup>-1</sup> )
5ppm LHA	5.64	5.65	-
P25	5.22	5.02	0.00970
P25 + 2.5ppm LHA	5.42	5.08	0.00231
P25 + 5ppm LHA	5.50	5.10	0.00152
P25 + NaBr	5.46	5.61	0.0510
P25 + NaBr + 2.5 ppm LHA	5.32	5.38	0.0284
P25 + NaBr + 5 ppm LHA	5.36	5.30	0.0200

Table 4-15. The pH and SMZ photodegradation rate constant of P25 with different concentrations of SRHA in the presence of 100 mM NaBr.

pH	Before experiment	After experiment	Rate constant (min <sup>-1</sup> )
5ppm SRHA	5.64	5.83	-
P25	5.32	5.13	0.0122
P25 + 2.5ppm SRHA	5.56	5.57	0.00681
P25 + 5ppm SRHA	5.70	5.44	0.00200
P25 + NaBr	5.46	5.62	0.0511
P25 + NaBr + 2.5 ppm SRHA	5.37	5.64	0.0294
P25 + NaBr + 5 ppm SRHA	5.48	5.51	0.0194

Table 4-16. Some selected characteristics of LHA and SRHA reported by IHSS.

(Criquet et al., 2015; Hakim & Kobayashi, 2018; Ritchie & Perdue, 2003)

HA from IHSS	Carbon content (%) (w/w)	Carboxylic groups (meq/g-C)	Phenolic groups (meq/g-C)	Aromatic carbon (%)
LHA	63.81	7.46	2.31	58
SRHA	52.63	9.13	3.72	31

## 4.4 The Mechanism of photocatalytic degradation

### 4.4.1 The effect of different scavengers on the removal of SMZ

#### 4.4.1.1 The effect of oxidants' scavengers on the removal of SMZ by TiO<sub>2</sub>

The role of •OH scavengers during the photocatalytic degradation of SMZ was studied. Allyl alcohol (3-propenol, AA; 100 mM) or tertiary butanol (*t*-buOH; 100 mM) were used as selective quenchers to differentiate the importance of reactions involving adsorbed radicals (e.g., •Br<sub>ads</sub> and •OH<sub>ads</sub>) and dissolved radicals (e.g., •OH, •Br) to photocatalytic degradation rates, respectively (Barazesh et al., 2016; Nosaka & Nosaka, 2017). Allyl alcohol was useful for probing surface-bound oxidants ( $k_{AA/•OH} = 7.5 \times 10^9 \text{ M}^{-1} \text{ s}^{-1}$  (B. M. Matthew & C. Anastasio, 2006; Ross, Bielski, et al., 1998),  $k_{AA/•Br} = 3.4 \times 10^9 \text{ M}^{-1} \text{ s}^{-1}$  (Guha et al., 1993; B. M. Matthew & C. Anastasio, 2006)) because the interaction of its  $\pi$ -orbitals with the positively charged surface and the high reactivity of the allylic carbon with oxidants allows it to react at the surface. In contrast, saturated alcohols (i.e., *t*-buOH) do not react near the surface, yet react rapidly with dissolved oxidants (•OH and •Br). The *t*-buOH reacts rapidly with powerful one electron oxidants such as •OH and •Cl ( $k_{t\text{-buOH}/•OH} = 6 \times 10^8 \text{ M}^{-1} \text{ s}^{-1}$  (Buxton et al., 1988),  $k_{t\text{-buOH}/•Cl} = 7 \times 10^8 \text{ M}^{-1} \text{ s}^{-1}$  (Gilbert et al., 1988)) (Wu et al., 2017; Yu et al., 2014). Although the rate constant for reaction of bromine free radicals and *t*-buOH ( $k_{t\text{-buOH}/•Br}$ ) is not known, it is likely to be large when  $k_{t\text{-buOH}/•Cl}$  is considered.

As shown in Figure 4-33, the addition of AA and *t*-buOH almost inhibited the degradation of SMZ by illuminated P25, suggesting that in the pure P25 system, both adsorbed and dissolved •OH radicals were important for the SMZ photodegradation. In the system of P25 with 100 mM NaBr, the degradation rates of SMZ were significantly decreased by AA but were slightly decreased in the presence of *t*-buOH, thus confirming the importance of surface-bound oxidants (i.e., •Br<sub>ads</sub>). Barazesh et al.

(2016) showed that surface-bound reactive bromine species (i.e.,  $\bullet\text{Br}_{\text{ads}}$ ) possibly contributed to oxidation of SMZ by electrolysis with the addition of chloride and bromide ions.

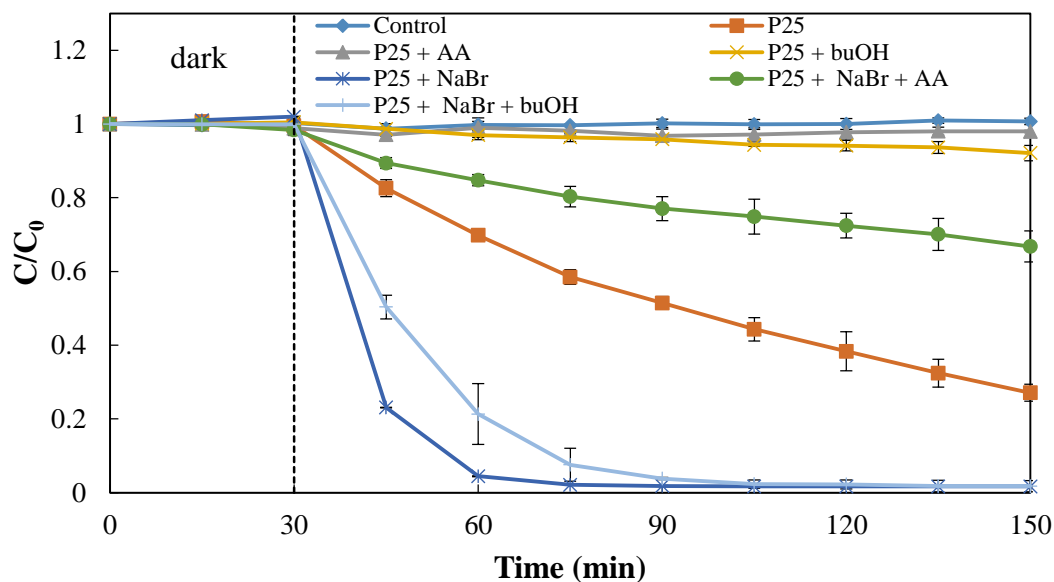
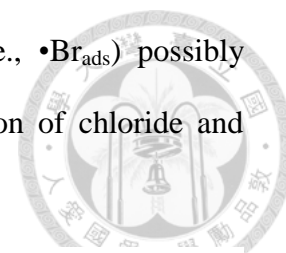


Figure 4-33. The photocatalytic degradation of 5 mg/L SMZ by 10 mg/L P25 with 100 mM scavengers (AA and *t*-buOH) under UV light. (UV light:  $\lambda = 365$  nm, 32W)

(Allyl alcohol (AA): scavenger of surface-bound OH and Br radicals.

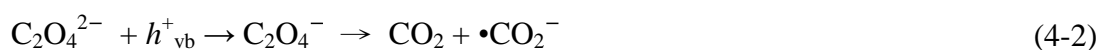
Tertiary butanol (*t*-buOH): scavenger of dissolved OH and Br radicals.)

Table 4-17. The pH and SMZ photodegradation rate constant of P25 with 100 mM scavengers (AA and *t*-buOH) in the presence of 100 mM NaBr.

pH	Before experiment	After experiment	Rate constant ( $\text{min}^{-1}$ )
Control	5.50	5.62	-
P25	5.33	5.12	0.0106
P25 + AA	4.98	4.70	-
P25 + <i>t</i> -buOH	5.43	5.40	-
P25 + NaBr	5.37	5.58	0.0693
P25 + NaBr + AA	4.95	5.70	0.00300
P25 + NaBr + <i>t</i> -buOH	5.34	5.63	0.0421

#### 4.4.1.2 The effect of photogenerated hole scavengers on the removal of SMZ by TiO<sub>2</sub>

Many studies have used oxalate (e.g. oxalic acid and sodium oxalate) as a hole scavenger to investigate the role of photogenerated hole on the surface of catalysts (Lee et al., 2005; Savory et al., 2010). While oxalate reacts relatively slowly with both hydroxyl radicals and hydrated electrons ( $k = 1.5 \times 10^7 \text{ M}^{-1}\text{s}^{-1}$  and  $k = 3.5 \times 10^7 \text{ M}^{-1}\text{s}^{-1}$ ), once adsorbed on TiO<sub>2</sub>, it is oxidation by  $h^+_{\text{vb}}$  to CO<sub>2</sub> through the following reactions (Rodríguez et al., 2015):



Because the reactivity and specificity of oxalate toward hydroxyl radical is relatively low, oxalate could be utilized as a good hole scavenger in the solution containing TiO<sub>2</sub>.

SMZ degradation kinetics by TiO<sub>2</sub> with 100 mM NaBr and different concentration of sodium oxalate is shown in Figure 4-34. The addition of Na<sub>2</sub>C<sub>2</sub>O<sub>4</sub> slightly reduced the degradation of SMZ in the pure P25 system. As the previous results (Figure 4-24), when the solution contained 100 mM NaBr, the degradation of SMZ was obviously accelerated. However, when the solution contained 100 mM NaBr and 10 mM Na<sub>2</sub>C<sub>2</sub>O<sub>4</sub>, the degradation of SMZ was inhibited.

The addition of Na<sub>2</sub>C<sub>2</sub>O<sub>4</sub>, however, slightly changed the pH condition of the photocatalytic system. To eliminate the effect of the difference of pH, Na<sub>2</sub>C<sub>2</sub>O<sub>4</sub> was mixed with H<sub>2</sub>C<sub>2</sub>O<sub>4</sub> to be used as the hole scavenger, and the concentration of C<sub>2</sub>O<sub>4</sub><sup>2-</sup> was fixed at 10 mM. Figure 4-35 depicted that the addition of 10 mM C<sub>2</sub>O<sub>4</sub><sup>2-</sup> significantly reduced the degradation of SMZ in the pure P25 system. On the other hand, the degradation of SMZ was totally inhibited by the addition of 10 mM C<sub>2</sub>O<sub>4</sub><sup>2-</sup> in the system containing P25 and 100 mM NaBr.

The inhibition of the photodegradation by addition of oxalate was because the photogenerated holes on the surface of TiO<sub>2</sub> particles were consumed by C<sub>2</sub>O<sub>4</sub><sup>2-</sup>, and there were a little •OH and •Br left to provide degradation ability. From another perspective, since the reaction in the system of P25 with 100 mM NaBr was inhibited more significantly than that of P25, the photogenerated hole may have significant effect on bromide oxidation (eq. 4-4~4-6).

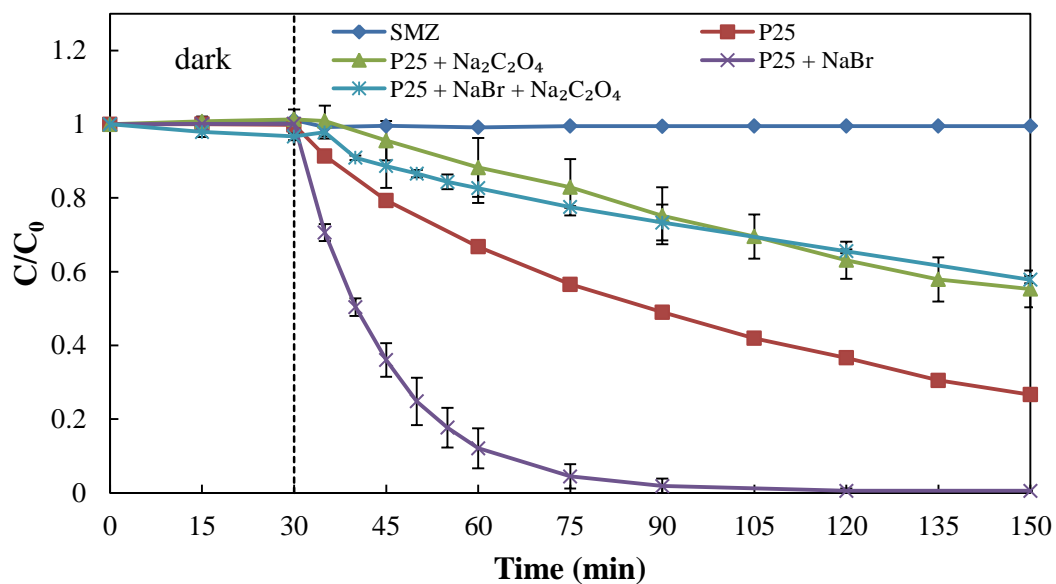


Figure 4-34. The photocatalytic degradation of 5 mg/L SMZ by 10 mg/L P25 with 100 mM NaBr and 10 mM Na<sub>2</sub>C<sub>2</sub>O<sub>4</sub> (hole scavenger) under UV light.

Table 4-18. The pH and SMZ photodegradation rate constant of P25 with 10 mM  $\text{Na}_2\text{C}_2\text{O}_4$  (hole scavenger) in the presence of 100 mM NaBr.

pH	Before experiment	After experiment	Rate constant ( $\text{min}^{-1}$ )
Control	5.44	5.48	-
P25	5.31	4.73	0.0107
P25 + $\text{Na}_2\text{C}_2\text{O}_4$	7.18	7.53	0.00520
P25 + NaBr	5.26	5.46	0.0694
P25 + NaBr + $\text{Na}_2\text{C}_2\text{O}_4$	7.12	7.44	0.00390

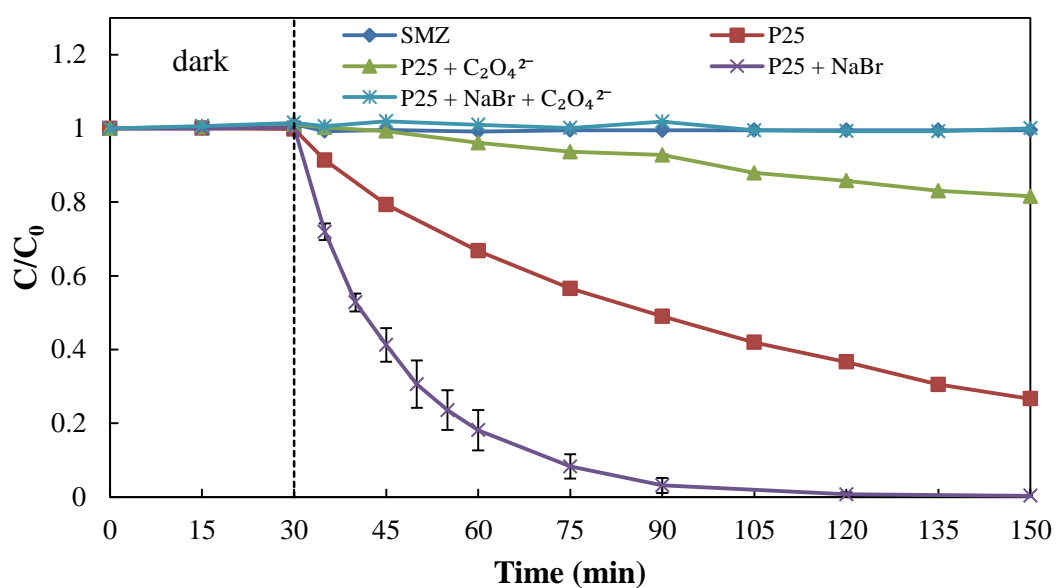


Figure 4-35. The photocatalytic degradation of 5 mg/L SMZ by 10 mg/L P25 with 100 mM NaBr and  $\text{Na}_2\text{C}_2\text{O}_4$  mixed with  $\text{H}_2\text{C}_2\text{O}_4$  (as hole scavengers and the concentration of  $\text{C}_2\text{O}_4^{2-}$  was fixed at 10 mM) under UV light. (UV light:  $\lambda = 365$  nm, 32W)

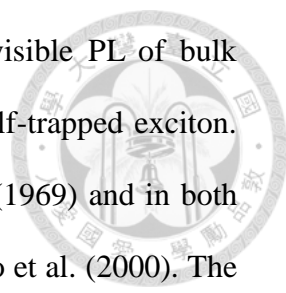
Table 4-19. The pH and SMZ photodegradation rate constant of P25 with 10 mM  $C_2O_4^{2-}$  (hole scavenger) in the presence of 100 mM NaBr.

pH	Before experiment	After experiment	Rate constant ( $min^{-1}$ )
Control	5.34	5.02	-
P25	5.28	4.81	0.0107
P25 + $C_2O_4^{2-}$	4.93	5.20	0.00180
P25 + NaBr	5.18	4.46	0.0583
P25 + NaBr + $C_2O_4^{2-}$	4.81	5.08	-

#### 4.4.2 Photoluminescence of $TiO_2$

Understanding the charge recombination process of a photocatalyst is crucial because it significantly influences the photochemical properties and photodegradation performance. Photoluminescence (PL) is a suitable tool to study the efficiency of charge carrier trapping, migration, and transfer, and to understand the fate of electron-hole pairs in photocatalyst particles because PL emissions result from the recombination of free carriers.  $TiO_2$  will absorb the incident photons with sufficient energy equal to or higher than the band-gap energy, which produces photoinduced charge carriers. In addition, the recombination of photoinduced electrons and holes releases energy in the form of PL emission spectra. Hence, a lower PL intensity indicates less charge recombination (Lim et al., 2015). According to the “antenna effect” proposed by Wang et al.(2003), the interparticle charge transfer takes place in the agglomerates of  $TiO_2$  NPs, which ensures an enhanced charge separation and a reduced recombination. Therefore, PL spectra were investigated.

The PL spectra of anatase and rutile  $TiO_2$  have been previously reported for both



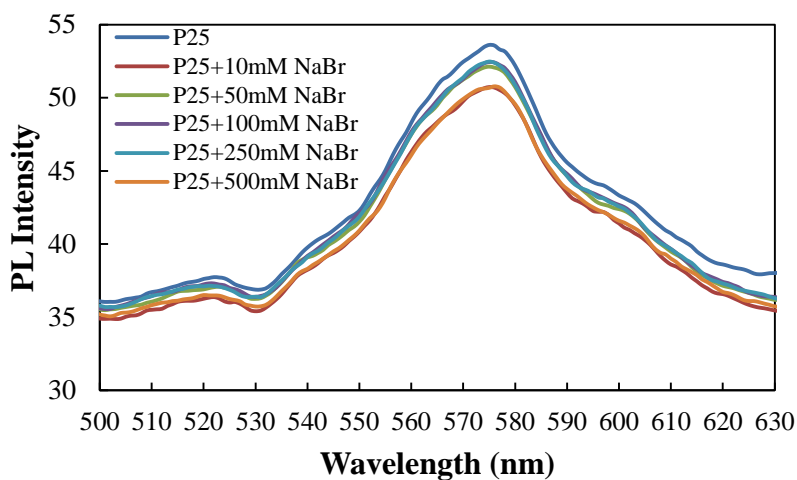
bulk and nanocrystalline samples. Tang et al. (1994) observed visible PL of bulk anatase crystals and assigned it to radiative recombination of a self-trapped exciton. The near-IR emission of bulk rutile was reported by Ghosh et al. (1969) and in both bulk and nanocrystalline phases by Nakato et al. (1983) and Tsujiko et al. (2000). The latter have assigned the rutile PL, which peaks at about 850 nm, to recombination of conduction band electrons with surface-trapped holes localized on triply coordinated oxygen atoms on (100) and (110) surfaces. Despite the ~25% rutile content of P25, no rutile emission is seen in P25. Knorr et al. (2008) speculated that the rutile emission is absent in P25 because the luminescent rutile surfaces (i.e., the (100) and (110) planes) are covered by the anatase phase.

Excitation of TiO<sub>2</sub> at 350 nm creates electrons in the conduction band and holes in the valence band which are rapidly trapped at defect sites. Figures 4-36a and b show the PL spectra of P25 and P25 with different concentrations of NaBr or NaCl, respectively. The samples were excited at  $\lambda = 350$  nm and the PL intensity maximum occurred at  $\lambda = 575$  nm. With the addition of different concentration of NaBr, the decrease in the intensity of peaks compared to P25 can be observed, which depicts the changes in the surface morphology that imparted extended lifetime to the excited states compared to P25. P25 showed a higher PL intensity due to the rapid recombination of photoinduced charge carriers, while the PL intensity decreased with the addition of different concentration of NaCl. As shown in Figure 4-36c, the peak of HBr-P25 was similar to that of P25. HCl-P25, on the other hand, showed visible PL but extending farther to UV-C region.

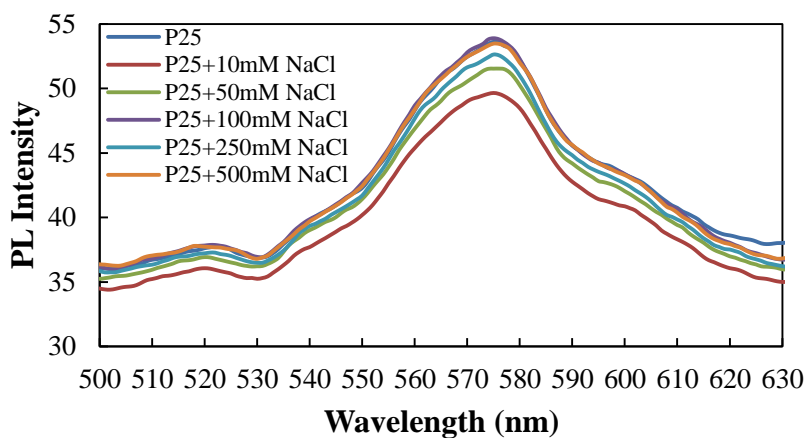




(a)



(b)



(c)

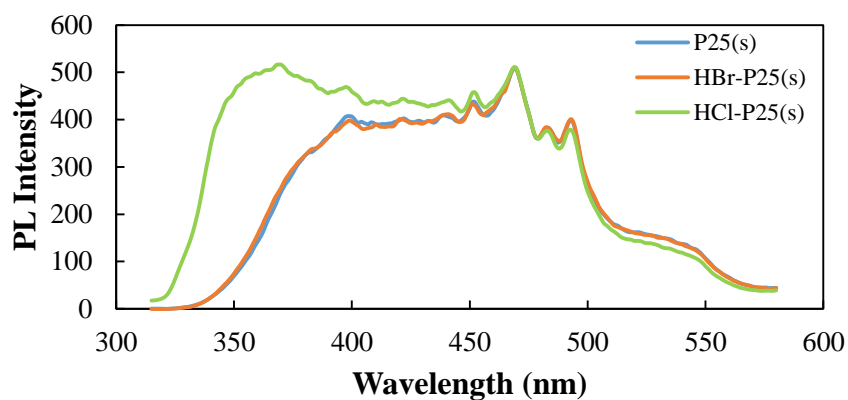


Figure 4-36. The PL spectra of P25 and P25 with different concentration of NaBr (a), NaCl (b), and P25, HBr-P25 and HCl-P25 at 300 mg/L (c). ( $\lambda_{\text{ex}} = 350 \text{ nm}$ )

### 4.4.3 Photocurrent measurements

The above photocatalytic reactions of SMZ and oxalate that mainly involve the hole transfer should be accompanied by the concurrent electron transfer on TiO<sub>2</sub>. To investigate the photogenerated electron transfer behavior on TiO<sub>2</sub> particles and how this behavior is affected by the presence of bromide, the generation of the photocurrent ( $I_{ph}$ ) in UV light irradiated suspensions of P25 was monitored in the presence and absence of bromide. We employed an electrochemical method that utilizes the redox couple of (Fe<sup>3+</sup>/Fe<sup>2+</sup>) as an electron shuttle as illustrated in Scheme 3-1.

Figure 4-37 compares the time profiles of the photocurrent generation in the suspensions of pure P25 and with 100 or 500 mM NaBr. The photocurrent for P25 with 100 and 500 mM NaBr was lower than that observed for pure P25, which indicated that the addition of NaBr inhibits the interfacial electron transfer process. Because Br<sub>2</sub> was generated under UV light irradiation, it could be explained that Br<sub>2</sub> reacted with electrons in the CB by hindering the electron transfer from the CB to the electron acceptor in the solution (i.e., oxygen). Therefore, the recombination of Br<sub>2</sub> with the reduced oxide surface under illumination would result in poorer overall photocurrent efficiencies (eq. 4-7~4-8) (Sheridan et al., 2018). As for P25 with 500 mM NaBr, the photocurrent was higher than P25 with 100 mM NaBr. This could be assumed that in the system of P25 with 500 mM NaBr, higher concentration of Br<sub>2</sub> was generated, and quickly vaporized, resulting in the weakly hindered electron transfer.



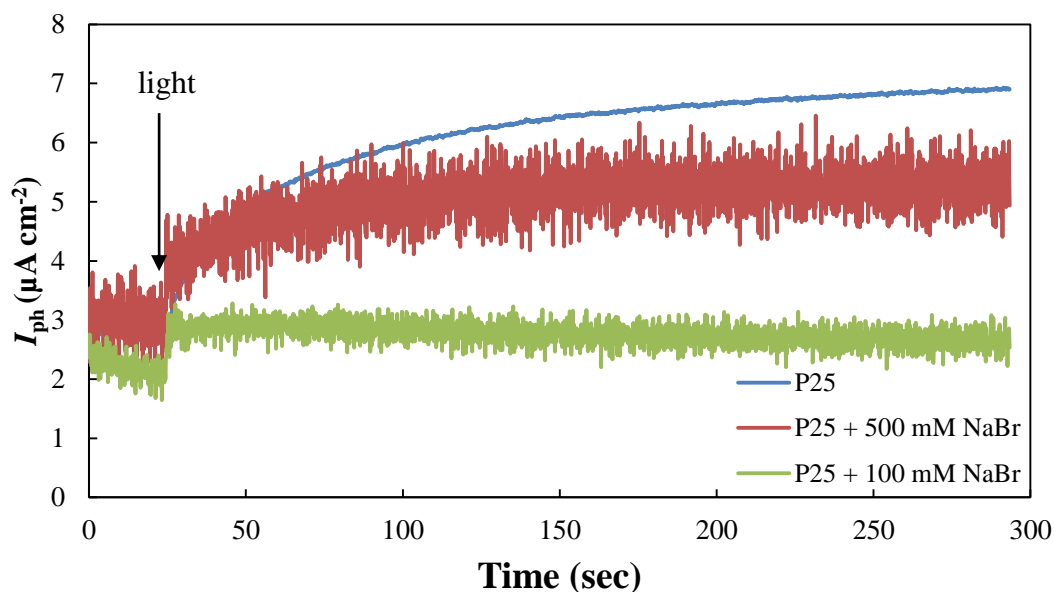


Figure 4-37. Time profiles of the generation of  $\text{Fe}^{3+}$ -mediated photocurrent ( $I_{\text{ph}}$ ) in suspensions of P25 and P25 with different concentration of NaBr. Experimental conditions:  $[\text{P25}] = 0.5 \text{ g L}^{-1}$ ,  $[\text{Fe}^{3+}] = 0.5 \text{ mM}$ ,  $[\text{NaBr}] = 100$  and  $500 \text{ mM}$ ,  $\lambda = 365 \text{ nm}$ , and the applied potential to the working electrode =  $+0.6 \text{ V SCE}$ .

#### 4.4.4 Radical measurements

##### 4.4.4.1 The measurement of hydroxyl radicals by coumarin and CCA method

To study the mechanism, we evaluated the generation of  $\bullet\text{OH}$  and asked whether the enhanced photocatalytic performance of P25 in the presence of  $\text{Br}^-$  could be caused by increasing the concentration of  $\bullet\text{OH}$ . Moreover, whether the oxidation of bromide could result from ROS formed during  $\text{TiO}_2$  photocatalysis, including  $\bullet\text{OH}$ , was also questioned. Coumarin (Zhang & Nosaka, 2013) and coumarin-3-carboxylic acid (CCA) (Zhang & Nosaka, 2014) were used for the detection of hydroxyl radicals ( $\bullet\text{OH}$ ). Coumarin carries no charge and is not adsorbed on the surface of  $\text{TiO}_2$  but can detect dissolved (free)  $\bullet\text{OH}$  in  $\text{TiO}_2$  suspension. It reacts with  $\bullet\text{OH}$  to form several OH substituted coumarins. Among them, only 7-hydroxycoumarin (umbelliferone) emits

strong fluorescence (Zhang & Nosaka, 2013). On the other hand, CCA possesses a -COOH group which adsorbs at the terminal OH of TiO<sub>2</sub>, so can detect •OH near the TiO<sub>2</sub> surface, reacting with •OH to form OH-CCA (Newton & Milligan, 2006).

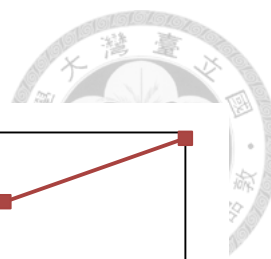
The relationship between TiO<sub>2</sub>, NaBr concentration and the generation amounts of dissolved •OH radicals was investigated using coumarin (Figure 4-38a). No fluorescence was detected in dark. Under UV irradiation, gradual increases in the fluorescence of coumarin were observed with the UV irradiation time in the system of P25 without NaBr. However, with the addition of NaBr, the generation of dissolved •OH radicals was almost totally inhibited.

The relationship between TiO<sub>2</sub>, NaBr concentration and the generation amounts of near-surface •OH radicals was investigated using CCA, as shown in Figure 4-38b. No fluorescence was detected in dark. Under UV irradiation, gradual increases in the fluorescence of CCA were observed with the UV irradiation time in the system of P25 without NaBr. However, with the addition of NaBr, the generation of adsorbed •OH radicals was almost totally inhibited.

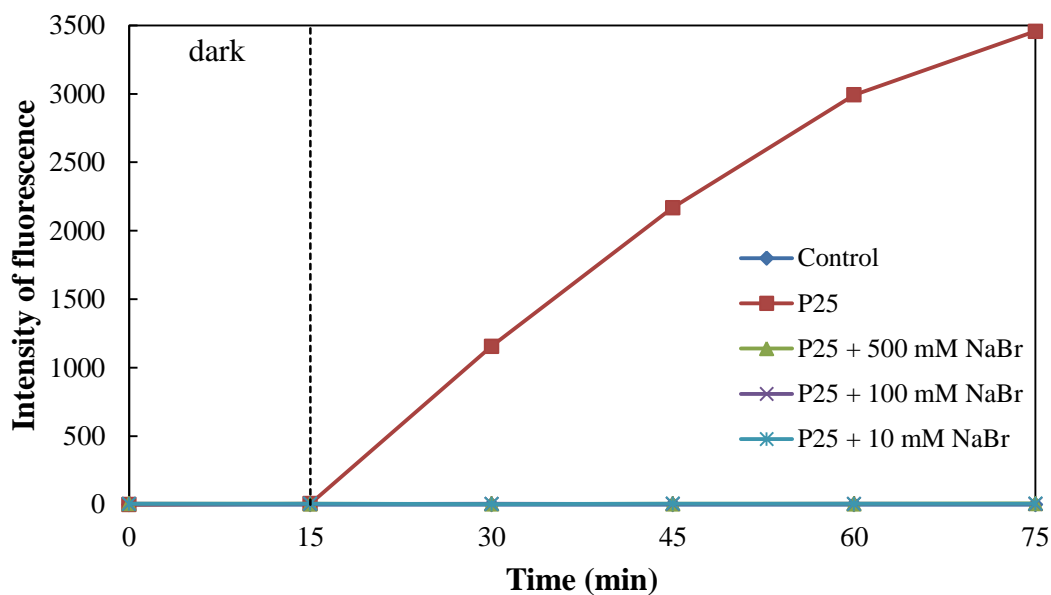
These results were consistent with previous studies showing that larger TiO<sub>2</sub> particles produce less •OH radical due to the lower surface area of the catalyst. From another perspective, since the addition of NaBr significantly inhibited the fluorescence of coumarin and CCA, the bromide oxidation may be caused by •OH. The •OH has a redox potential (+ 2.31 V) that is more than enough to oxidize bromide (- 0.78 V). Therefore, bromide ions would be oxidized by •OH to form other reactive bromine species, which would also react with •OH (eq. 4-9~4-16) (B. M. Matthew & C. Anastasio, 2006). However, Wu et al. (2016) reported that there was no quenching of hydroxyphenyl fluorescein (HPF), a fluorescent probe to detect •OH, and only minor quenching of singlet oxygen sensor green (SOSG), a fluorescent probe to detect <sup>1</sup>O<sub>2</sub>, in the system of 10 mM TiO<sub>2</sub> with 10 mM NaBr irradiated by UVA light,

indicating that the oxidation of bromide was caused by a direct oxidation arising from the photoactivated TiO<sub>2</sub> rather than oxidation by an intermediate ROS, including •OH and <sup>1</sup>O<sub>2</sub>. Jiang et al. (2016) also reported that the loss of para-chlorobenzoic acid (*p*CBA, the probe compound for •OH detection) was not detectable during Fe (VI) oxidation of bromide-containing water in both borate and phosphate buffers, indicating an insignificant role of •OH in bromide oxidation. On the other hand, Huang et al. (2016) reported that there was obvious quenching of HPF and SOSG in the 1 mM TiO<sub>2</sub> with 10 mM KI irradiated by UVA light, showing that the oxidation of iodide was relevant to •OH and <sup>1</sup>O<sub>2</sub>. However, Salimi (2016) reported that CCA had some advantages compared to HPF in detection of •OH radicals in fibroblast cells, including higher measured values, repeatability, and stability of measurements. From studies above, it could be concluded that whether the bromide oxidation could result from •OH generated during TiO<sub>2</sub> photocatalysis was still controversial. Nevertheless, in this study, the bromide oxidation could be caused by •OH, confirmed by the results of coumarin and CCA measurements.





(a)



(b)

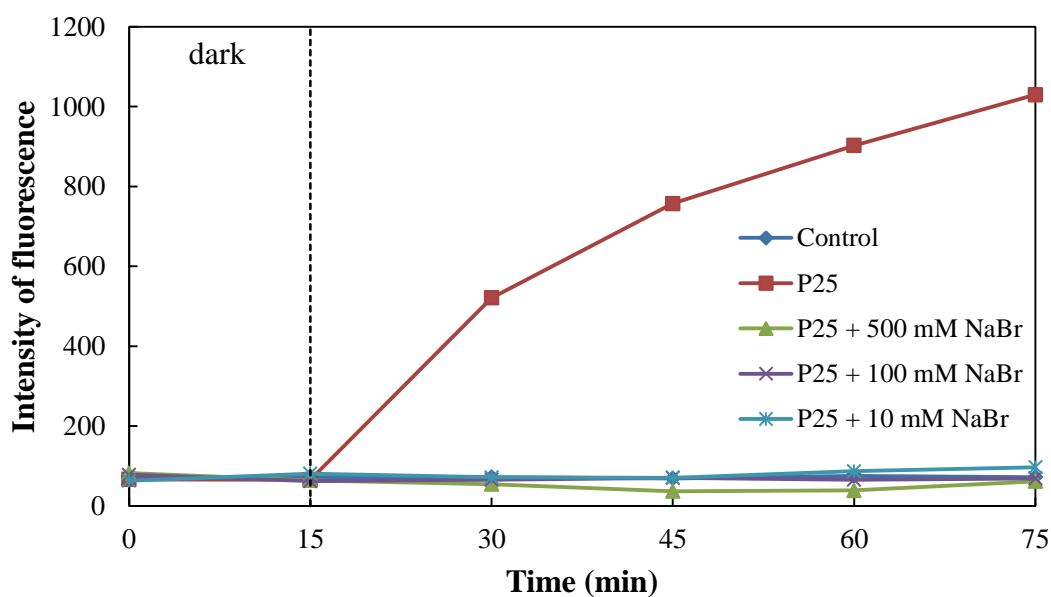


Figure 4-38. The dissolved and near-surface OH radicals measured by fluorescence probe molecule (a) coumarin and (b) coumarin-3-carboxylic acid (CCA), respectively.

(Coumarin and CCA concentration: 0.1 mM)

#### 4.4.4.2 The measurement of reactive bromine species by DPD method

The photocatalytic degradation process results in holes being trapped by  $\text{Br}^-$ , presumably to yield  $\cdot\text{Br}$ , which could conceivably yield  $\text{Br}_2$  and its hydrolysis products  $\text{HBrO}$  and  $\text{BrO}^-$ , known as reactive bromine species (RBS). Therefore, analyses were undertaken for the potentially generated long-lived reactive bromine species using DPD method.

It can be seen from Figure 4-39 that the concentration of total reactive bromine species increased to about 0.3 mg/L in 60 min irradiation for P25 with 500 mM NaBr. After 120 min irradiation, the concentration of total RBS reached to 0.23 mg/L for P25 with 50, 100 and 500 mM NaBr. These results suggested that RBS was generated in the UV/ $\text{TiO}_2$  process in the presence of  $\text{Br}^-$ . Reactive bromine species enhanced the photocatalytic degradation of SMZ by P25 under UV light irradiation.

As shown in Figure 4-40, the concentration of total reactive bromine species of HBr-P25 increased to about 0.69 mg/L during 45 min of irradiation and then gradually declined. On the other hand, the concentration of total reactive chlorine species of HCl-P25 was lower than the concentration of total RBS of HBr-P25, which is consistent with the above more SMZ degradation enhancement by HBr-P25 than HCl-P25. However, free bromine species seem more effective than free chlorine species (Vikesland et al., 2013). Moreover, the production of reactive chlorine species was lower than that of reactive bromine species. These may be the reason why there was also some reactive chlorine species generated in the system, but bromide ion has more significant enhancement effect than chloride ion on photocatalytic degradation of SMZ.

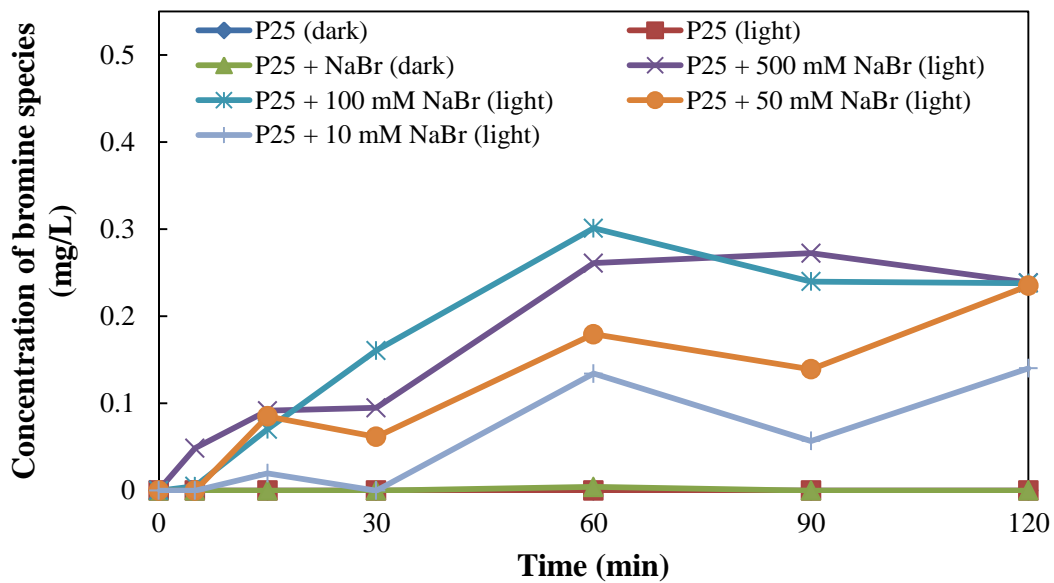


Figure 4-39. The DPD results of P25 with different concentration of NaBr.

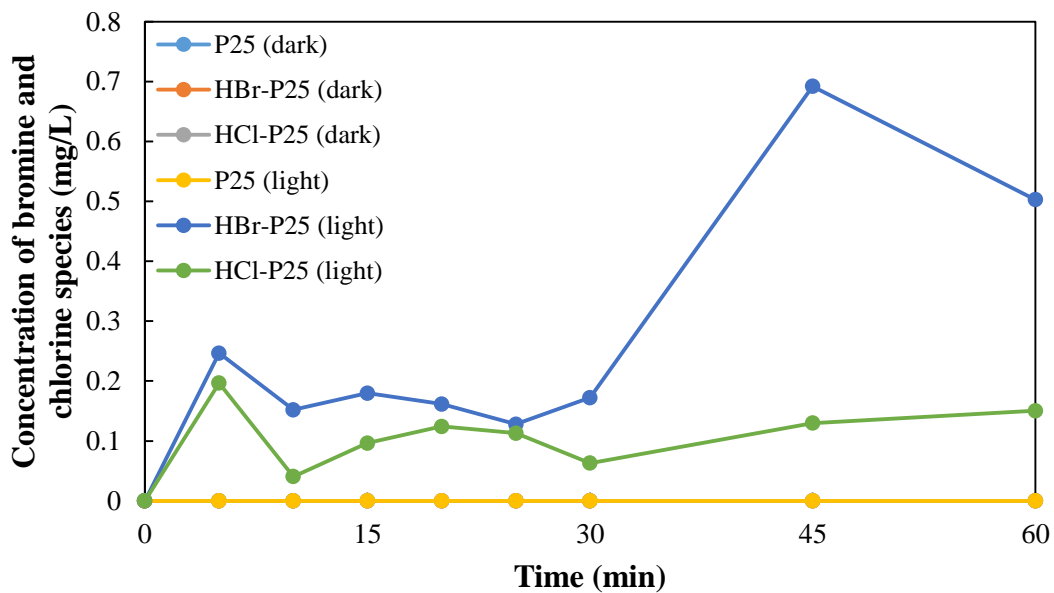
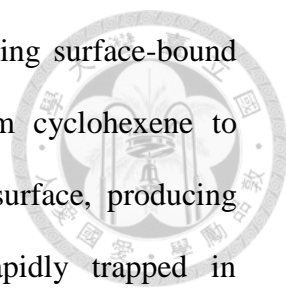


Figure 4-40. The DPD results of HBr-P25 and HCl-P25.

#### 4.4.4.3 The measurement of bromine by dibromocyclohexane test

Fox and Pettit (1985) reported their investigation of the system: the oxidation of bromide on  $\text{TiO}_2$  powder in oxygenated acetonitrile containing cyclohexene. They used cyclohexene as a probe to propose a mechanism in which the photoexcited  $\text{TiO}_2$





carried out a one-electron oxidation of adsorbed bromide, producing surface-bound bromine atoms. These potentially could abstract hydrogen from cyclohexene to initiate autoxidation or could migrate along the semiconductor surface, producing bromine ( $\text{Br}_2$ ), which migrates into solution where it is rapidly trapped in conventional electrophilic addition to form *trans*-1,2-dibromocyclohexane. Zabicky and Nutkovič (1986) also reported that when cyclohexene was added to aqueous bromine solutions, bromohydrin and dibromo adduct would yield, and their ratio in the final product depends on the olefin feed rate. Shaw *et al.* (1997) showed the bromination of cyclohexene in water, too. Therefore, we used cyclohexene as a probe to explore the mechanism of bromide oxidation in UV/TiO<sub>2</sub> aqueous system containing cyclohexene.

For the dibromocyclohexane test, all samples contained 5 mg/L cyclohexene as the reactant. In the dark, there was no dibromocyclohexane generated. As illustrated in Figure 4-41, in the system containing only cyclohexene or P25, there was no dibromocyclohexane generated under irradiation for 2 hr. On the other hand, in the system containing P25 and different concentration of NaBr, especially 500 mM, *trans*-1,2-dibromocyclohexane quickly generated once upon irradiation. Within 1 min of irradiation, the concentration of dibromocyclohexane generated increased rapidly to 20 nM in the system containing P25 and 500 mM NaBr. In the system containing 10 mM NaBr, there was no dibromocyclohexane generated under irradiation for 1 hr, either, indicating that cyclohexene would not react with bromide ions. However, in the system containing 100 mM and 500 mM NaBr, there was a little dibromocyclohexane around 2~3 nM generation during the photocatalytic experiment. Previous study showed that the bromination of cyclohexene in water either in the presence or absence of light produced *trans*-1,2-dibromocyclohexane as the only product (Shaw *et al.*, 1997). As for P25 and HBr-P25, Figure 4-42 indicated that there was no generation of

dibromocyclohexane in the dark by 300 mg/L P25 and HBr-P25. As for P25 under UV light illumination, there was still no dibromocyclohexane generated. However, in the system of HBr-P25, large amounts of dibromocyclohexane formed once upon irradiation, and the concentration of dibromocyclohexane increased with the irradiation time, finally reaching 410 nM at 60 min of irradiation. The generation of *trans*-1,2-dibromocyclohexane implies that at least a quantity of photogenerated bromine atoms become detached from the surface as bromine molecules and can be trapped in normal electrophilic addition sequences although our work does not unambiguously demonstrate whether this desorption occurs as  $\cdot\text{Br}$ ,  $\cdot\text{Br}_2^-$ , or  $\text{Br}_2$ .

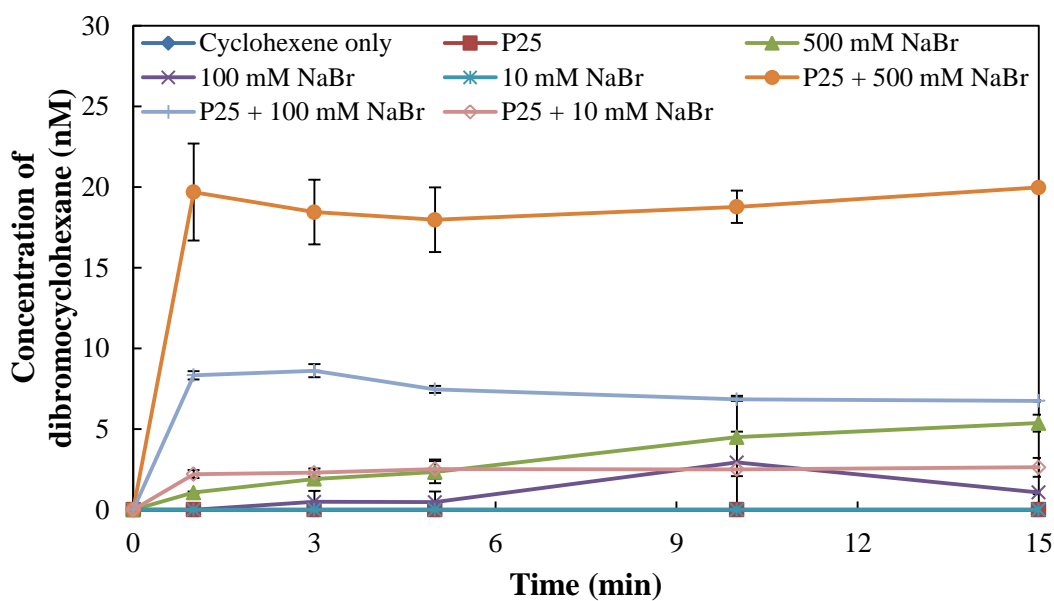


Figure 4-41. The result of dibromocyclohexane test by P25 with different concentrations of NaBr.

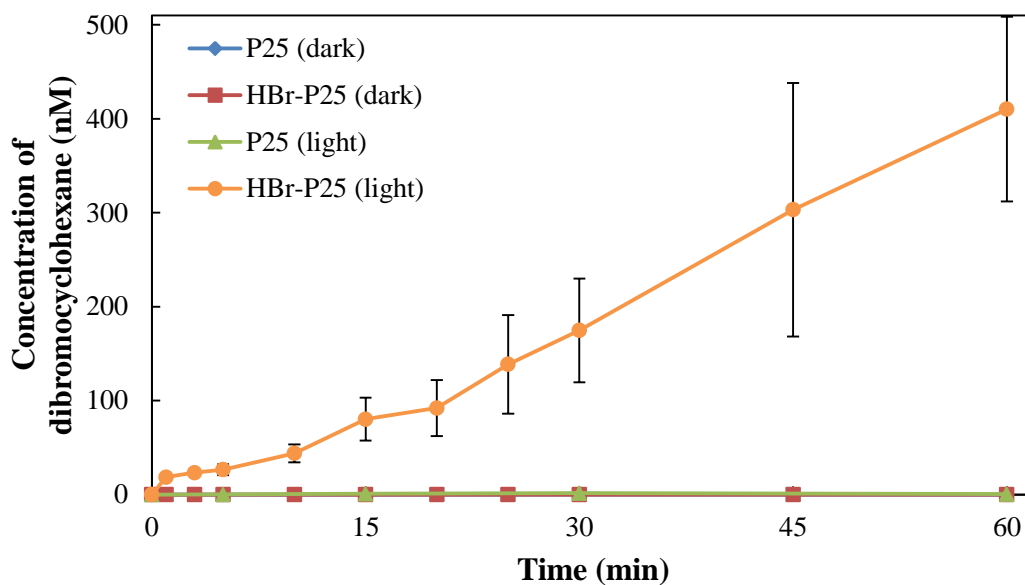


Figure 4-42. The result of dibromocyclohexane test by 300 mg/L P25 and HBr-P25.

#### 4.4.4.4 The measurement of tribromide ion

In order to detect any production of bromine, we attempted to detect the presence of tribromide ion ( $\text{Br}_3^-$ ) which is quantitatively formed from the reaction between bromine ( $\text{Br}_2$ ) and  $\text{Br}^-$  (eq. 4-17), and the reaction rate constant is  $9.6 \times 10^8$  (Ershov, 2004).



As shown in Figure 4-43, we measured the absorbance of  $\text{Br}_3^-$  at 267 nm, and the results showed that there was production of  $\text{Br}_2$  by P25 with 100 and 500 mM NaBr under UV light illumination. However, we did not observe  $\text{Br}_2$  production in the system of P25 with 10 mM NaBr under UV light irradiation. That may be due to the lower concentration of  $\text{Br}^-$  which was not enough to react with  $\text{Br}_2$  and generate  $\text{Br}_3^-$ , or the concentration of generated  $\text{Br}_3^-$  was lower than detection limit of UV-vis spectrometer. On the other hand, we did not detect the presence of  $\text{Br}_3^-$  in the system of HBr-P25, either. Since at 500 mM NaBr, less  $\text{Br}_3^-$  was observed compared to 100

mM NaBr, indicating  $\bullet\text{Br}$  or  $\text{Br}_2$  could form on  $\text{TiO}_2$  surface and not diffuse into solutions a lot or  $\text{Br}_2$  gas could vaporize out of water. Especially, compared to dibromocyclohexane results, most RHS could be generated and adsorbed on  $\text{TiO}_2$  surface.

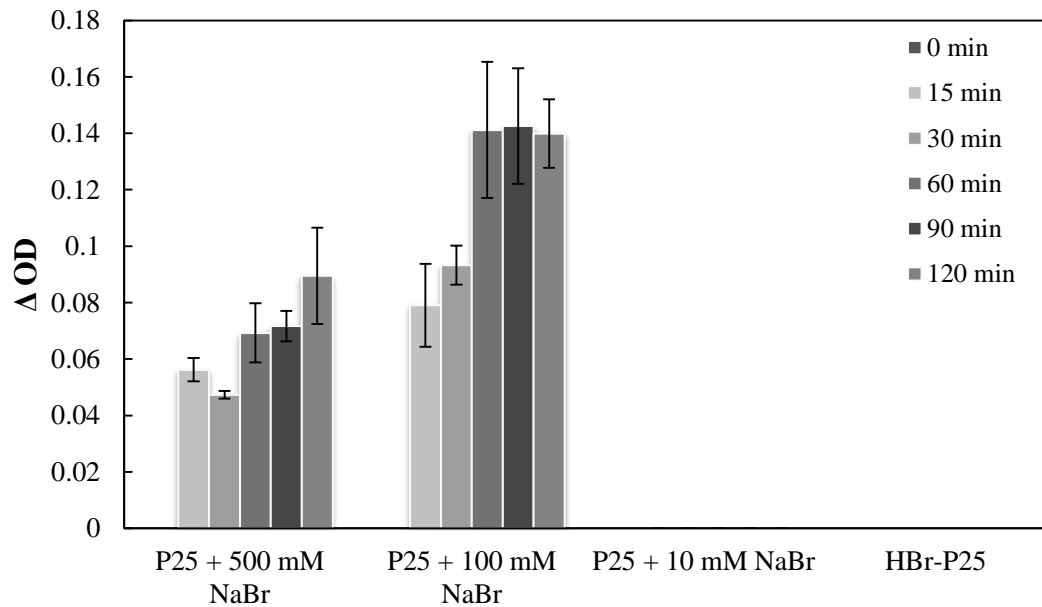
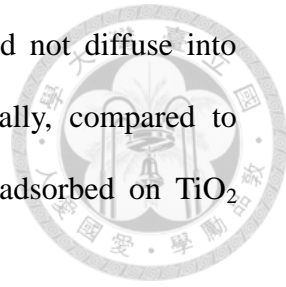


Figure 4-43. The  $\text{Br}_3^-$  absorbance test ( $\lambda_{\text{max}} = 267 \text{ nm}$ ) of 10 mg/L P25 with different concentration of NaBr under UV light irradiation.

#### 4.4.4.5 The measurement of photocatalytic sites by TBO method

The density of photocatalytic sites for the formation of surface hydroxyl and bromine radical (i.e.,  $\equiv\text{TiOH}$ ) was determined using the toluidine blue O (TBO) colorimetric method (Barazesh et al., 2016; Chua et al., 2005; Ray et al., 2012).

As shown in Figure 4-44, with addition of 100 mM NaBr, the density of photocatalytic sites on P25 surface increased instead of decreasing, indicating more sites generated which could be resulted from bromide oxidation as discussed above.

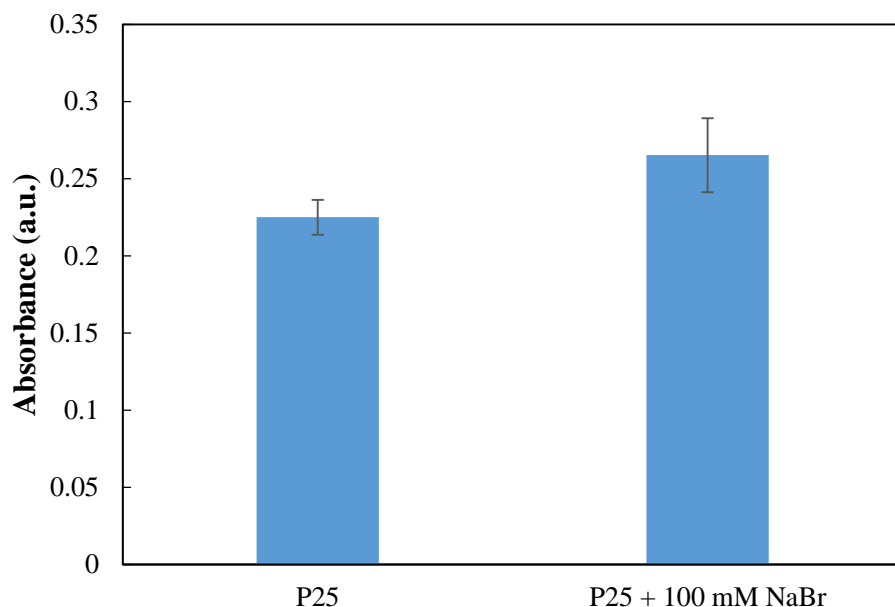


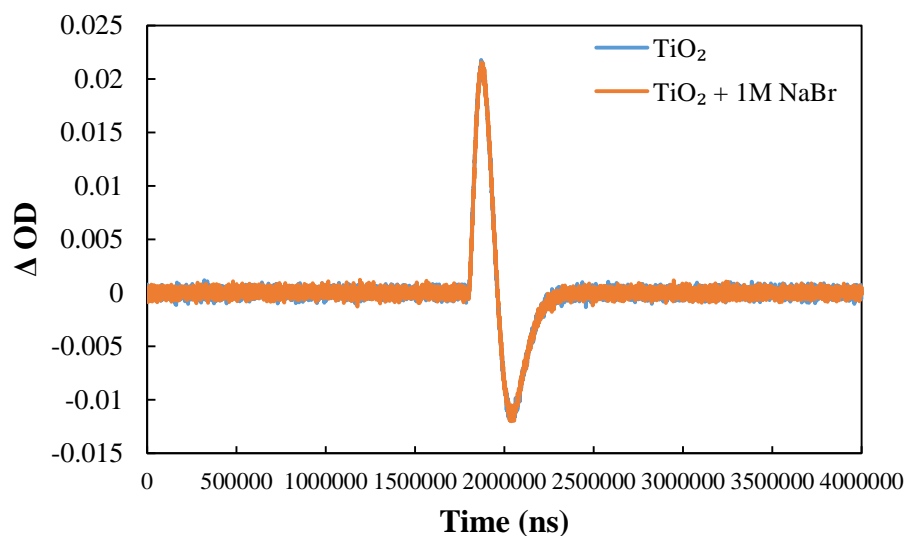
Figure 4-44. The results of TBO test.

#### 4.4.4.6 Transient absorption spectra (TAS)

Jing et al. (2012) concluded that the TAS signals at 450 nm and 800 nm are assigned to relaxed photoholes and photoelectrons in  $\text{TiO}_2$ , respectively. The transient absorption spectra are given in Figure 4-45. Neither the TAS signals at 450 nm and 800 nm of P25 with 100 mM NaBr nor those of P25 with 500 mM NaBr could be observed. Therefore, P25 with 1 M NaBr was chosen to conduct the experiments. The TAS of pure P25 solution and P25 with 1M NaBr both showed typical absorption at  $\lambda = 450$  nm, corresponding to photogenerated holes in  $\text{TiO}_2$ , as shown in Figure 4-45a. However,  $\Delta\text{OD}$  of P25 with 1M NaBr did not have difference from pure P25. On the other hand, Figure 4-45b illustrated that both pure P25 solution and P25 with 1M NaBr had TAS signal at 800 nm, related to photoexcited electrons in  $\text{TiO}_2$ . Nevertheless,  $\Delta\text{OD}$  of P25 with 1M NaBr did not have difference from pure P25.



(a)



(b)

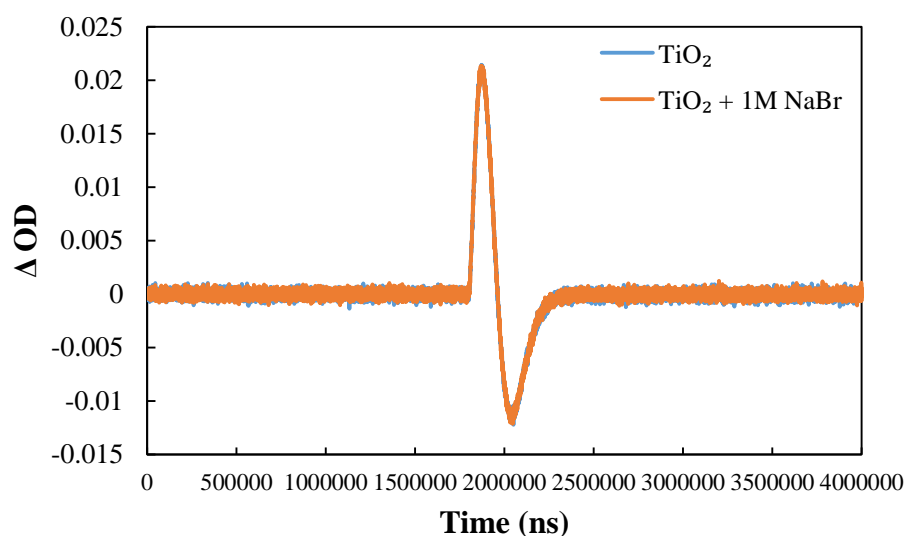
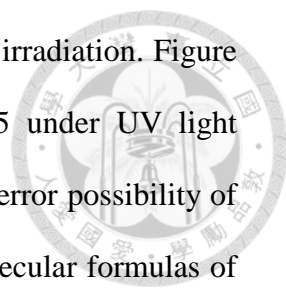


Figure 4-45. Transient absorption spectra of photoelectrons of  $\text{TiO}_2$  and  $\text{TiO}_2$  with 1 M NaBr. (a) TAS signals: 450 nm (b) TAS signals: 800 nm.

#### 4.4.5 Byproducts measurements

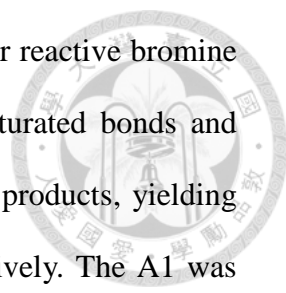
To fully understand the photocatalytic degradation process of SMZ by P25 with NaBr under UV light irradiation, HPLC/MS analyses were further performed to identify the oxidation byproducts of SMZ. Table 4-20 listed the susceptible oxidation byproduct in the photocatalytic degradation process. Figure 4-46 illustrated the



brominated byproducts of SMZ by P25 with NaBr under UV light irradiation. Figure 4-47 presented the brominated byproducts of SMZ by HBr-P25 under UV light irradiation. The molecular structures, formulas,  $m/z$  ( $[M+H]^+$ ) and error possibility of the oxidation byproducts were summarized in Table 4-21. The molecular formulas of the oxidation byproducts were assigned by software-based mass assignments using their exact masses and isotope patterns. The theoretical  $m/z$  values were within less than 1 ppm error compared with the observed  $m/z$  values, indicating strong confidence in the assignments.

In photocatalytic degradation of SMZ by  $TiO_2$ , numerous byproducts can be formed since  $\bullet OH$  does not exhibit a high degree of functional group selectivity. From LC/MS spectrum, one susceptible byproduct was detected but not well identified. The susceptible byproduct was 3-amino-5-methylisoxazole with  $m/z = 99.055$  for  $[M+H]^+$ . Further confirmation was still needed to identify this byproduct. Byproduct 3-amino-5-methylisoxazole should be generated due to the hydroxyl radical attack. The hydroxyl radical attack on the sulfonamide bond results in the cleavage of the S–N bond. Subsequent abstraction of a hydrogen by the cleaved nitrogen results in the formation of 3-amino-5-methylisoxazole, sulfanilic acid, and hydroxysulfanilic acid (Hu et al., 2007).

For the effect of bromide addition on the transformation of SMZ, two brominated byproducts were detected. Moreover, in the photodegradation process of SMZ by HBr-P25, the same two brominated byproducts were also observed. The corresponding MS spectra were shown in Figures 4-46 and 4-47. For byproduct A1 ( $m/z = 331.96$  for  $[M+H]^+$ ), an ion at  $m/z$  of 331 with a bromine isotopic peak at 333 was detected shown in Figure 4-46a and 4-47a. Moreover, for byproduct A2 ( $m/z = 412.86$  for  $[M+H]^+$ ), an ion at  $m/z$  of 411 with two bromine isotopic peaks at 409 and 413 was detected shown in Figure 4-46b and 4-47b. The photodegradation of SMZ by

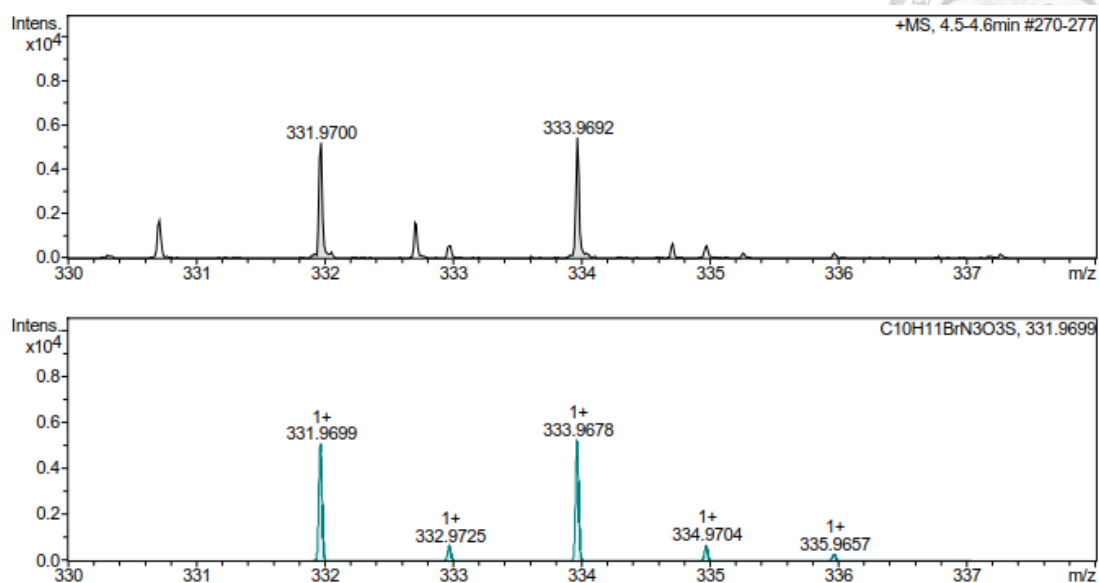


P25 with the addition of bromide yielded  $\text{Br}_2$ ,  $\text{HOBr}/\text{OBr}^-$  and other reactive bromine species (e.g.,  $\bullet\text{Br}$ ,  $\bullet\text{Br}_2^-$ ). Hypobromous acid can react with unsaturated bonds and electron-rich moieties such as aromatic rings to form halogenated products, yielding mono and di-brominated derivatives of SMZ, A1 and A2, respectively. The A1 was identified as N-brominated SMZ or another byproduct that the electrophilic substitution with bromine occurred at the aniline moiety. In A2, electrophilic substitution with bromine occurred at the aniline moiety. The exact position of two bromine substituents could not be determined just based on the obtained LC/MS spectra. Though further analysis was required to confirm the real structure of brominated byproducts A1 and A2, we discovered the brominated derivatives of SMZ that were reported by few papers, and this was the first time that these brominated byproducts were discovered in the photocatalytic degradation of SMZ by  $\text{TiO}_2$  under UV-A light irradiation.

The LC peak of SMZ byproduct which was generated and photodegraded by P25 with NaBr or by HBr-P25 under UV irradiation was shown in Figure 4-48 and 4-49. The peak of SMZ byproduct in UV/ $\text{TiO}_2$  system in the presence of 100 mM NaBr first generated at 5 min irradiation and did not decrease until 60 min. At 120 min, the peak of byproduct was eliminated to low intensity, and the concentration of it was less than 1 mg/L. On the other hand, the peak of SMZ byproduct in UV/HBr-P25 system first generated within 5 min and then kept decreasing. After irradiation for 30 min, the byproduct's peak was almost diminished. Previous study indicated that chlorinated organic compounds were considered to be more toxic than parent compounds, and the brominated organic compounds were even toxic than chlorinated organic compounds. Since the formation of brominated derivatives of SMZ declined in the following process of photodegradation, the photocatalytic reaction by P25 NPs with  $\text{Br}^-$  or by HBr-P25 may not cause further problems of toxic byproducts.



(a)



(b)

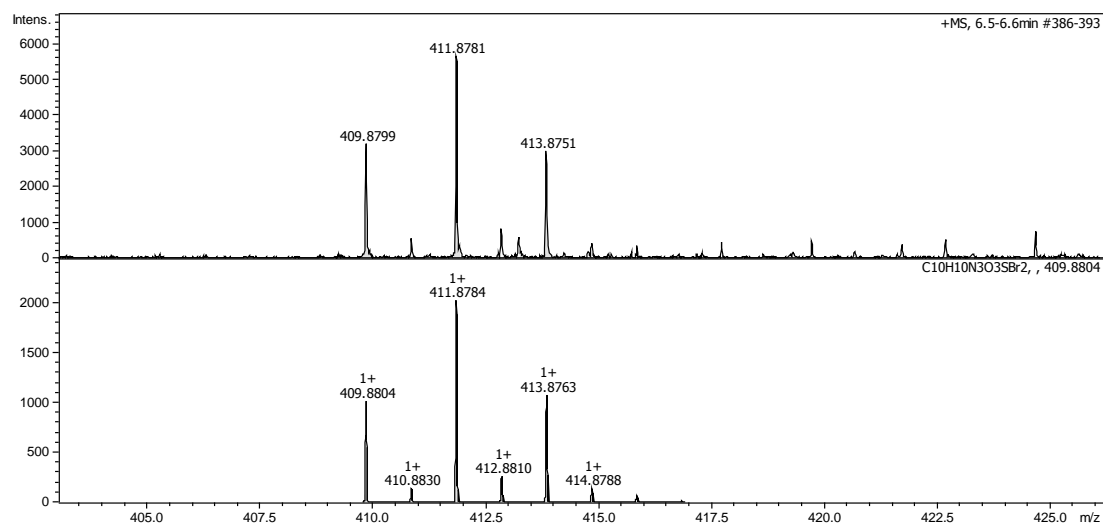


Figure 4-46. Mass spectra for byproducts of SMZ photocatalytic degradation by  $TiO_2$  with 100 mM NaBr: (a) brominated SMZ and (b) dibrominated SMZ. Spectra a and b were both obtained by LC/MS-ESI<sup>+</sup>.

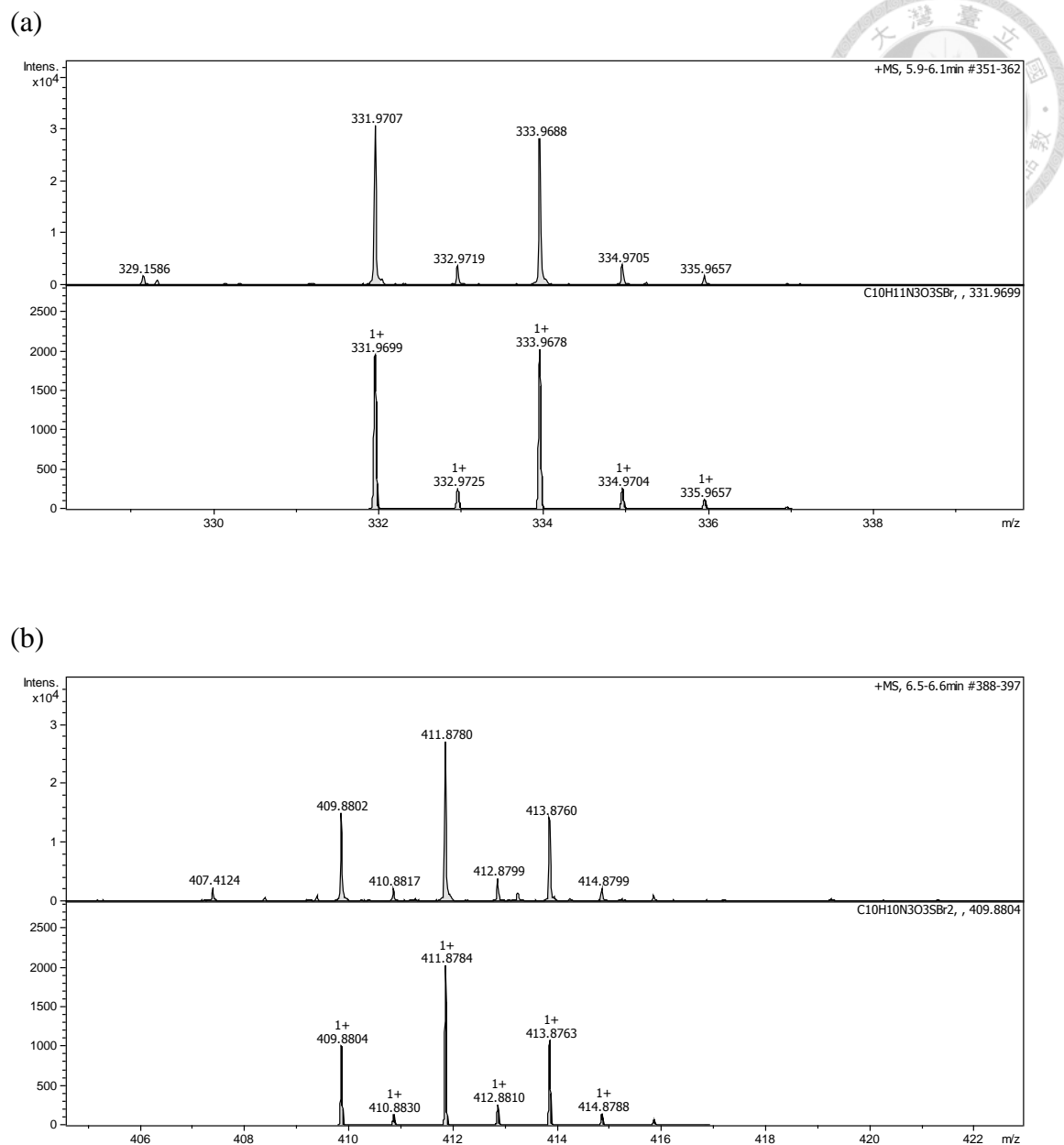
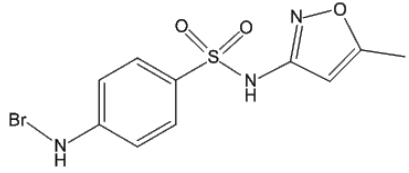
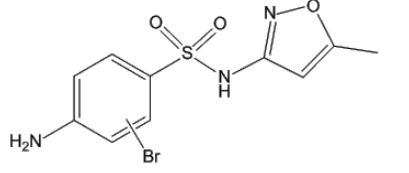
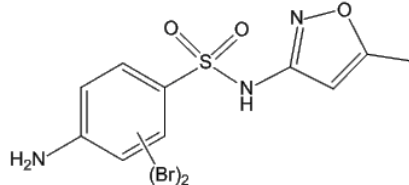


Figure 4-47. Mass spectra for byproducts of SMZ photocatalytic degradation by HBr-P25: (a) brominated SMZ and (b) dibrominated SMZ. Spectra a and b were both obtained by LC/MS-ESI<sup>+</sup>.

Table 4-20. The structure and m/z ([M+H]<sup>+</sup>) of susceptible byproduct.

Molecule structure	Formula	m/z ([M+H] <sup>+</sup> )	IUPAC name
	C <sub>4</sub> H <sub>6</sub> N <sub>2</sub> O	99.055	3-amino-5-methylisoxazole

Table 4-21. The structure and m/z ( $[M+H]^+$ ) of brominated byproducts.

Molecule structure	Formula	m/z ( $[M+H]^+$ )	Error (ppm)	Products
	$C_{10}H_{10}N_3O_3SBr$	331.96	0.3	A1
	$C_{10}H_{10}N_3O_3S(Br)_2$	412.86	0.5	A2
				

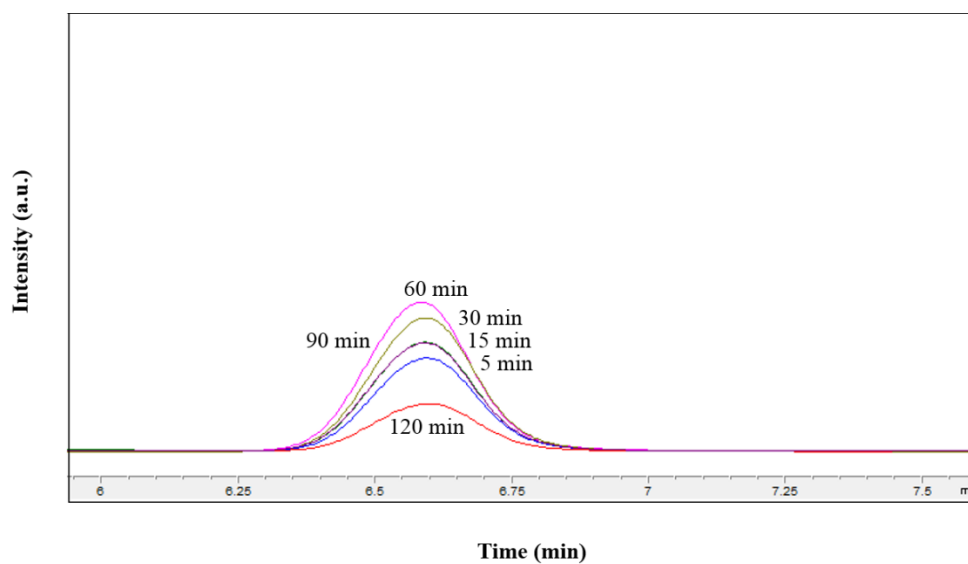


Figure 4-48. LC pattern of SMZ byproduct which was photodegraded by P25 NPs aggregates with 100 mM NaBr within 120 min.

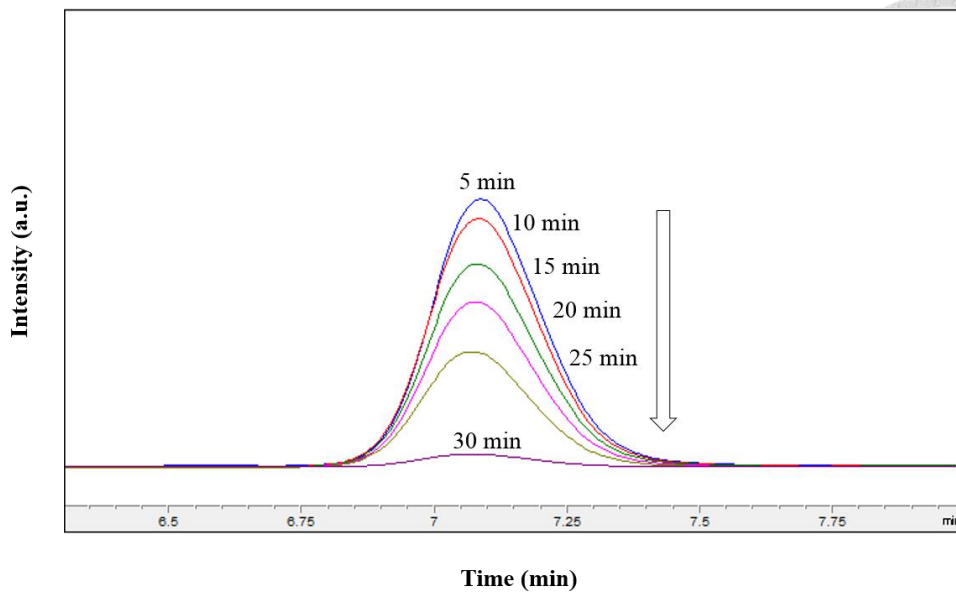


Figure 4-49. LC pattern of SMZ byproduct which was photodegraded by HBr-P25 within 30 min.

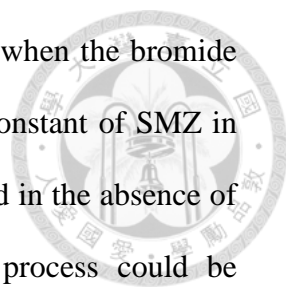
## Chapter 5 Conclusion



The particle size of P25 was around 26.5 nm confirmed by TEM and the hydrodynamic diameter of P25 was about 180 nm. The values of total surface area of P25, HBr-P25, HCl-P25, NaBr-P25 and NaCl-P25 were 54.9, 52.1, 50.3, 34.9 and 43.3 m<sup>2</sup>/g, respectively. The SEM-EDX and XPS results of HBr-P25, HCl-P25, NaBr-P25 and NaCl-P25 revealed that bromine or chlorine element existed. The morphologies of P25, HBr-P25, HCl-P25 and NaBr-P25 were crystalline anatase and rutile phase presented by XRD pattern, except NaCl-P25. It only showed the (101) planes of anatase TiO<sub>2</sub>.

The particle size of P25 increased with time progressively with the increasing concentrations of NaCl or NaBr. With more than 10 mM NaCl or NaBr, the particle sizes of P25 increased quickly within 3 min and exceeded 1000 nm after 15 min. The particle slightly settled down, resulting in 25~30% particle lost in the suspension within 3 hr.

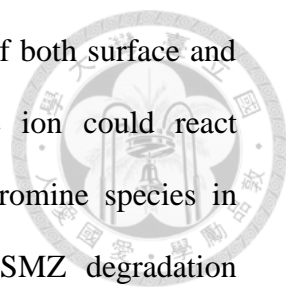
The amount of SMZ adsorbed to P25 surface was negligible. When there were halide salts in the solution, TiO<sub>2</sub> NPs aggregated and became larger particle agglomerates, resulting in the decrease of surface area and active site on the surface, which reduced the photocatalytic performance of TiO<sub>2</sub>. Therefore, the addition of NaCl diminished the photodegradation rate. The degradation rate of SMZ slightly decreased with any concentration of NaCl but slightly increased with 10 mM NaCl. However, the photodegradation rate of SMZ by TiO<sub>2</sub> with the addition of NaBr increased instead of decreasing. A significant enhancement effect, which was promoted by adding bromide ions, was observed in the process of SMZ photodegradation using TiO<sub>2</sub> NPs aggregates under UV irradiation. This enhancement



enlarged as the bromide concentration was increased but lessened when the bromide concentration exceeded 100 mM. The observed degradation rate constant of SMZ in the presence of 100 mM NaBr was 6-fold greater than that observed in the absence of bromide. The enhanced degradation of SMZ in the UV/TiO<sub>2</sub> process could be achieved by reactive bromine species generated from bromide ions.

SMZ degradation rate was accelerated by the presence of NaBr, and the concentration had much more effect on the degradation rate even in a low concentration. As a result, it may be possible that the enhancement of SMZ degradation was related to the presence of bromide ions. According to the “antenna effect” proposed by Wang et al.(2003), there was the interparticle charge transfer in the agglomerates of TiO<sub>2</sub> NPs. Therefore, the photoluminescence and photocurrent were investigated. With the addition of different concentration of NaBr, the decrease in the intensity of PL peaks compared to P25 was observed, which depicted less charge recombination compared to P25. The photocurrent for P25 with NaBr was lower than that observed for pure P25, which indicated that Br<sub>2</sub> may be generated in the system, and the recombination of Br<sub>2</sub> with the reduced oxide surface would result in poorer photocurrent efficiencies.

In this study, the enhancement mechanism of SMZ photodegradation with aggregated P25 NPs in the presence of bromide ions was studied. The degradation of SMZ by P25 was significantly inhibited by AA and *t*-buOH, two oxidants scavengers. The photogenerated holes on the surface of TiO<sub>2</sub> were consumed by C<sub>2</sub>O<sub>4</sub><sup>2-</sup>, the hole scavenger, resulting in the inhibition of SMZ degradation. The photogenerated holes possessed ability to produce radicals like •OH and reactive bromine species, and dominated SMZ degradation. On the other hand, under UV irradiation, gradual increases in the fluorescence of P25 with coumarin and CCA were observed with the UV irradiation time, which indicated dissolved and surface •OH generation,

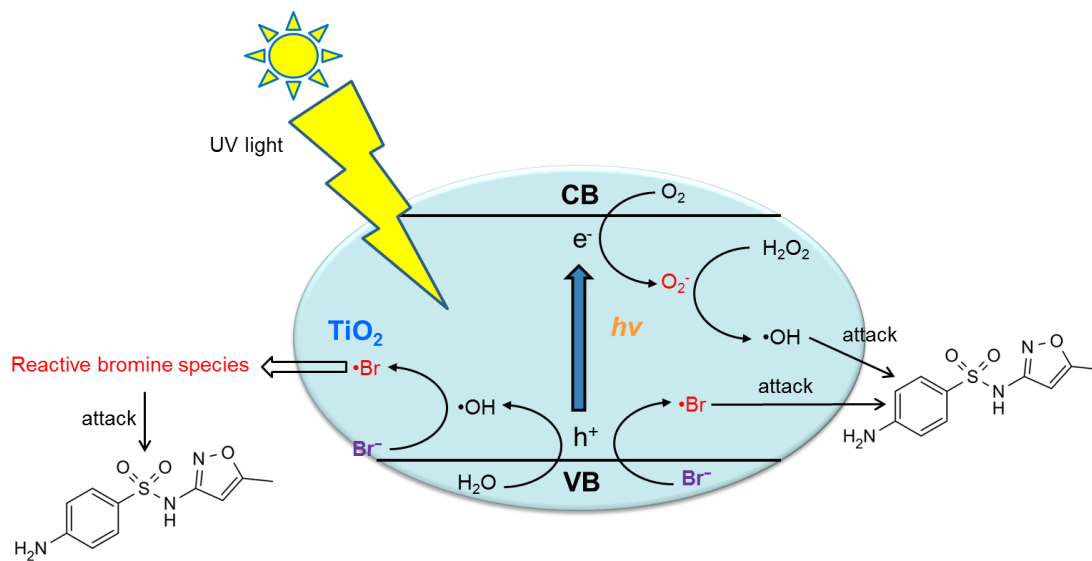


respectively. However, with the addition of NaBr, the generation of both surface and dissolved  $\bullet\text{OH}$  was totally inhibited, elucidating that bromide ion could react with  $\bullet\text{OH}$  radicals. To gain insight into the effect of reactive bromine species in photoreaction, the detection of reactive bromine species and SMZ degradation byproducts analysis were conducted. The results of DPD test depicted that there were reactive bromine species generated in the system of P25 with NaBr. Bromine can not only react with cyclohexene to form dibromocyclohexane, but also react with  $\text{Br}^-$  to form  $\text{Br}_3^-$ . Therefore, through dibromocyclohexane and  $\text{Br}_3^-$  test, it could be confirmed that there was production of bromine on the surface of P25 with NaBr. Under UV light irradiation,  $\text{Br}^-$  reacts with the photogenerated holes of  $\text{TiO}_2$  or  $\bullet\text{OH}$  to produce  $\bullet\text{Br}$  and reactive bromine species, accelerating the photodegradation of SMZ. Compared to P25, HBr-P25 had an enhanced photocatalytic performance. There were also reactive bromine species generated in the system of HBr-P25, indicating that this reaction occurs on the surface of  $\text{TiO}_2$ . Furthermore, in the system of P25 with 100 mM NaBr, the degradation rate of SMZ were significantly decreased by AA (surface-bound oxidants scavenger), but were slightly decreased by *t*-buOH (dissolved oxidants scavenger), thus confirming the importance of surface-bound oxidants.

Reactive bromine species can react with unsaturated bonds and electron-rich moieties such as aromatic rings to form halogenated products. HPLC-MS results showed that there were two halogenated byproducts, mono and di-brominated derivatives of SMZ, in the photodegradation process of SMZ by P25 in the presence of NaBr and by HBr-P25.

In summary, under UV irradiation, the photogenerated holes on the surface of  $\text{TiO}_2$  may interact with bromide ions and produce reactive bromine species, including radical reactive bromine species ( $\bullet\text{Br}$  and  $\bullet\text{Br}_2^-$ ) and non-radical reactive bromine species ( $\text{HOBr}$ ,  $\text{Br}_2$ ,  $\text{Br}_3^-$  etc.). Reactive bromine species were stronger electrophiles

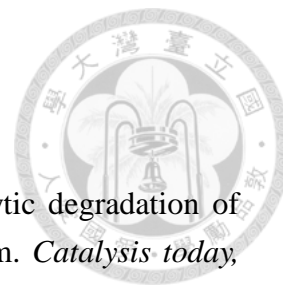
and longer half-life oxidants than  $\cdot\text{OH}$ . Therefore, in the photocatalytic degradation of SMZ by P25, reactive bromine species were generated, resulting in the enhancement of degradation rate. Photocatalytic degradation of SMZ by  $\text{TiO}_2$  nanoparticles in a high concentration of halides is an example which could be considered as an efficient and cheap method for the treatment of organic wastewater. These findings may have significant technical implications for optimizing the photochemical technologies in salt-rich wastewater treatment.



Scheme 5-1. The mechanism of SMZ photocatalytic degradation by  $\text{TiO}_2$  NPs aggregates in the presence of bromide ions.



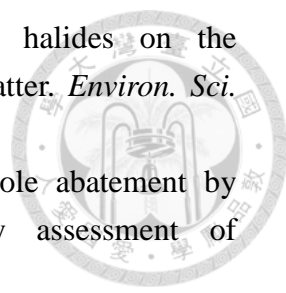
## References



- Abellán, M. N., Giménez, J., & Esplugas, S. (2009). Photocatalytic degradation of antibiotics: The case of sulfamethoxazole and trimethoprim. *Catalysis today*, *144*(1-2), 131-136.
- Amano, F., Ishinaga, E., & Yamakata, A. (2013). Effect of Particle Size on the Photocatalytic Activity of WO<sub>3</sub> Particles for Water Oxidation. *J. Phys. Chem. C*, *117*(44), 22584-22590.
- Anastasio, C., & Matthew, B. (2006). A chemical probe technique for the determination of reactive halogen species in aqueous solution: Part 2—Chloride solutions and mixed bromide/chloride solutions. *Atmos. Chem. Phys.*, *6*(9), 2439-2451.
- Barazesh, J. M., Prasse, C., & Sedlak, D. L. (2016). Electrochemical Transformation of Trace Organic Contaminants in the Presence of Halide and Carbonate Ions. *Environ. Sci. Technol.*, *50*(18), 10143-10152.
- Bu, Y., Wang, L., Chen, B., Niu, R., & Chen, Y. (2018). Effects of typical water components on the UV 254 photodegradation kinetics of haloacetic acids in water. *Sep. Purif. Technol.*, *200*, 255-265.
- Buxton, G. V., Greenstock, C. L., Helman, W. P., & Ross, A. B. (1988). Critical review of rate constants for reactions of hydrated electrons, hydrogen atoms and hydroxyl radicals ( $\cdot\text{OH}/\cdot\text{O}^-$ ) in aqueous solution. *J. Phys. Chem. Ref. Data*, *17*(2), 513-886.
- Calza, P., Massolino, C., Pelizzetti, E., & Minero, C. (2008). Solar driven production of toxic halogenated and nitroaromatic compounds in natural seawater. *Sci. Total Environ.*, *398*(1-3), 196-202.
- Calza, P., Massolino, C., Pelizzetti, E., & Minero, C. (2012). Role of iron species in the photo-transformation of phenol in artificial and natural seawater. *Sci. Total Environ.*, *426*, 281-288.
- Caregnato, P., Rosso, J. A., Soler, J. M., Arques, A., Martire, D. O., & Gonzalez, M. C. (2013). Chloride anion effect on the advanced oxidation processes of methidathion and dimethoate: role of Cl<sub>2</sub><sup>•-</sup> radical. *Water Res*, *47*(1), 351-362.
- Carp, O. (2004). Photoinduced reactivity of titanium dioxide. *Prog. Solid State Ch.*, *32*(1-2), 33-177.
- Chen, G., Liu, X., & Su, C. (2012). Distinct effects of humic acid on transport and retention of TiO<sub>2</sub> rutile nanoparticles in saturated sand columns. *Environ. Sci. Technol.*, *46*(13), 7142-7150.
- Cheng, M., & Bakac, A. (2008). Photochemical Oxidation of Halide Ions by a

- Nitratochromium(III) Complex. Kinetics, Mechanism, and Intermediates. *J. Am. Chem. Soc.*, 130(16), 5600-5605.
- Cheng, Q., Deng, X., Zhang, H., Guo, R., Cui, Y., Ma, Q., Zhang, X., Cheng, X., Xie, M., & Li, B. (2018). Microwave assisted construction of Ag-AgBr/reduced TiO<sub>2</sub> nano-tube arrays photoelectrode and its enhanced visible light photocatalytic performance for degradation of 4-chlorophenol. *Sep. Purif. Technol.*, 193, 255-263.
- Chiang, K., Lim, T. M., Tsen, L., & Lee, C. C. (2004). Photocatalytic degradation and mineralization of bisphenol A by TiO<sub>2</sub> and platinized TiO<sub>2</sub>. *Appl. Catal. A-Gen.*, 261(2), 225-237.
- Chua, K.-N., Lim, W.-S., Zhang, P., Lu, H., Wen, J., Ramakrishna, S., Leong, K. W., & Mao, H.-Q. (2005). Stable immobilization of rat hepatocyte spheroids on galactosylated nanofiber scaffold. *Biomaterials*, 26(15), 2537-2547.
- Company, V. L. (2015). The chemistry of chlorine.
- Criquet, J., Rodriguez, E. M., Allard, S., Wellauer, S., Salhi, E., Joll, C. A., & von Gunten, U. (2015). Reaction of bromine and chlorine with phenolic compounds and natural organic matter extracts--Electrophilic aromatic substitution and oxidation. *Water Res*, 85, 476-486.
- Cui, Y., Zhang, Z., Li, B., Guo, R., Zhang, X., Cheng, X., Xie, M., & Cheng, Q. (2018). Ultrasound assisted fabrication of AgBr/TiO<sub>2</sub> nano-tube arrays photoelectrode and its enhanced visible photocatalytic performance and mechanism for detoxification of 4-chlorophenol. *Sep. Purif. Technol.*, 197, 189-196.
- De Luca, A., He, X., Dionysiou, D. D., Dantas, R. F., & Esplugas, S. (2017). Effects of bromide on the degradation of organic contaminants with UV and Fe<sup>2+</sup> activated persulfate. *Chem. Eng. J.*, 318, 206-213.
- Deng, X., Zhang, H., Guo, R., Cheng, X., & Cheng, Q. (2018). Construction of AgBr nano-cakes decorated Ti<sup>3+</sup> self-doped TiO<sub>2</sub> nanorods/nanosheets photoelectrode and its enhanced visible light driven photocatalytic and photoelectrochemical properties. *Appl. Surf. Sci.*, 441, 420-428.
- Ding, S., Niu, J., Bao, Y., & Hu, L. (2013). Evidence of superoxide radical contribution to demineralization of sulfamethoxazole by visible-light-driven Bi<sub>2</sub>O<sub>3</sub>/Bi<sub>2</sub>O<sub>2</sub>CO<sub>3</sub>/Sr<sub>6</sub>Bi<sub>2</sub>O<sub>9</sub> photocatalyst. *J Hazard Mater*, 262, 812-818.
- Dodd, M. C., & Huang, C. (2004). Transformation of the Antibacterial Agent Sulfamethoxazole in Reactions with Chlorine: Kinetics, Mechanisms, and Pathways. *Environ. Sci. Technol.*, 38, 5607-5615.
- Dong, H., Zeng, G., Tang, L., Fan, C., Zhang, C., He, X., & He, Y. (2015). An overview on limitations of TiO<sub>2</sub>-based particles for photocatalytic degradation

- of organic pollutants and the corresponding countermeasures. *Water Res.*, *79*, 128-146.
- Dukes, F. M., Iuppa, E., Meyer, B., & Shultz, M. J. (2012). Differing photo-oxidation mechanisms: electron transfer in TiO<sub>2</sub> versus iron-doped TiO<sub>2</sub>. *Langmuir*, *28*(49), 16933-16940.
- Eaton, A. D., Cleseri, L. S., & Greenberg, A. E. (1995). Standard Methods for the Examination of Water and Wastewater. *American Water Works Association*.
- Eigen, M., & Kustin, K. (1962). The kinetics of halogen hydrolysis. *J. Am. Chem. Soc.*, *84*(8), 1355-1361.
- Emerson, D. W. (1994). Microdetermination of bromine, chlorine, and chlorine dioxide in water in any combination. *Microchem. J.*, *50*(1), 116-124.
- Ershov, B. G. (2004). Kinetics, mechanism and intermediates of some radiation-induced reactions in aqueous solutions. *Russ. Chem. Rev.*, *73*(1), 101-113.
- Ferguson, M. A., Hoffmann, M. R., & Hering, J. G. (2005). TiO<sub>2</sub>-Photocatalyzed As(III) Oxidation in Aqueous Suspensions: Reaction Kinetics and Effects of Adsorption. *Environ. Sci. Technol.*, *39*, 1880-1886.
- Fox, M. A., & Pettit, T. L. (1985). Use of Organic Molecules as Mechanistic Probes for Semiconductor-Mediated Photoelectrochemical Oxidations: Bromide Oxidation. *The Journal of Organic Chemistry*, *50*(25), 5013-5015.
- Fujishima, A., Rao, T. N., & Tryk, D. A. (2000). Titanium dioxide photocatalysis. *J. Photoch. Photobio. C.*, *1*(1), 1-21.
- Gallard, H., Leclercq, A., & Croue, J. P. (2004). Chlorination of bisphenol A: kinetics and by-products formation. *Chemosphere*, *56*(5), 465-473.
- Gao, S., Zhao, Z., Xu, Y., Tian, J., Qi, H., Lin, W., & Cui, F. (2014). Oxidation of sulfamethoxazole (SMX) by chlorine, ozone and permanganate--a comparative study. *J Hazard Mater*, *274*, 258-269.
- García-Figueroa, A., Pena-Pereira, F., Lavilla, I., & Bendicho, C. (2017). Headspace single-drop microextraction coupled with microvolume fluorospectrometry for highly sensitive determination of bromide. *Talanta*, *170*, 9-14.
- Geng, Y., Lei, G., Liao, Y., Jiang, H.-Y., Xie, G., & Chen, S. (2017). Rapid organic degradation and bacteria destruction under visible light by ternary photocatalysts of Ag/AgX/TiO<sub>2</sub>. *J. Environ. Chem. Eng.*, *5*(6), 5566-5572.
- Ghosh, A. K., Wakim, F., & Addiss Jr, R. (1969). Photoelectronic processes in rutile. *Phys. Rev.*, *184*(3), 979.
- Gilbert, B. C., Stell, J. K., Peet, W. J., & Radford, K. J. (1988). Generation and Reactions of the Chlorine Atom in Aqueous Solution. *J. Chem. Soc., Faraday Trans. I*, *84*(10), 3319-3330.

- 
- Glover, C. M., & Rosario-Ortiz, F. L. (2013). Impact of halides on the photoproduction of reactive intermediates from organic matter. *Environ. Sci. Technol.*, 47(24), 13949-13956.
- Gonzalez, O., Sans, C., & Esplugas, S. (2007). Sulfamethoxazole abatement by photo-Fenton toxicity, inhibition and biodegradability assessment of intermediates. *J Hazard Mater*, 146(3), 459-464.
- Grebel, J. E., Pignatello, J. J., & Mitch, W. A. (2010). Effect of halide ions and carbonates on organic contaminant degradation by hydroxyl radical-based advanced oxidation processes in saline waters. *Environ. Sci. Technol.*, 44(17), 6822-6828.
- Greenberg, A. E. T., R. Rhodes., Clesceri, L. S., & Franson, M. A. H. (1985). *Standard Methods for the Examination of Water and Wastewater* (16 ed.). Washington, D.C.: American Public Health Association.
- Guha, S. N., Schoneich, C., & Asmus, K. D. (1993). Free Radical Reductive Degradation of vic-Dibromoalkanes and Reaction of Bromine Atoms with Polyunsaturated Fatty Acids: Possible Involvement of Br. in the 1, 2-Dibromoethane-Induced Lipid-Peroxidation. *Arch. Biochem. Biophys.*, 305(1), 132-140.
- Gunten, U. v., & Oliveras, Y. (1998). Advanced Oxidation of Bromide-Containing Waters: Bromate Formation Mechanisms. *Environ. Sci. Technol.*, 32, 63-70.
- Guo, C., Xu, J., Wang, S., Zhang, Y., He, Y., & Li, X. (2013). Photodegradation of sulfamethazine in an aqueous solution by a bismuth molybdate photocatalyst. *Catal. Sci. Technol.*, 3(6), 1603.
- Hakim, A., & Kobayashi, M. (2018). Aggregation and charge reversal of humic substances in the presence of hydrophobic monovalent counter-ions: Effect of hydrophobicity of humic substances. *Colloids Surf. A: Physicochem. Eng. Asp.*, 540, 1-10.
- Hao, W., Zheng, S., Wang, C., & Wang, T. (2002). Comparison of the photocatalytic activity of TiO<sub>2</sub> powder with different particle size. *J. Mater. Sci. Lett.*, 21(20), 1627-1629.
- Hsiung, C. E., Lien, H. L., Galliano, A. E., Yeh, C. S., & Shih, Y. H. (2016). Effects of water chemistry on the destabilization and sedimentation of commercial TiO<sub>2</sub> nanoparticles: Role of double-layer compression and charge neutralization. *Chemosphere*, 151, 145-151.
- Hu, L., Flanders, P. M., Miller, P. L., & Strathmann, T. J. (2007). Oxidation of sulfamethoxazole and related antimicrobial agents by TiO<sub>2</sub> photocatalysis. *Water Res*, 41(12), 2612-2626.
- Huang, Y. Y., Choi, H., Kushida, Y., Bhayana, B., Wang, Y., & Hamblin, M. R. (2016).

- Broad-Spectrum Antimicrobial Effects of Photocatalysis Using Titanium Dioxide Nanoparticles Are Strongly Potentiated by Addition of Potassium Iodide. *Antimicrob. Agents Chemother.*, 60(9), 5445-5453.
- Hui Liu, Huimin Zhao, Xie Quan, Yaobin Zhang, & Chen, S. (2009). Formation of Chlorinated Intermediate from Bisphenol A in Surface Saline Water under Simulated Solar Light Irradiation. *Environ. Sci. Technol.*, 43, 7712–7717.
- Hurum, D. C., Agrios, A. G., & Gray\*, K. A. (2003). Explaining the Enhanced Photocatalytic Activity of Degussa P25 Mixed-Phase TiO<sub>2</sub> Using EPR. *J. Phys. Chem. B*, 107(19), 4545-4549.
- Iguchi, S., Teramura, K., Hosokawa, S., & Tanaka, T. (2015). Effect of the chloride ion as a hole scavenger on the photocatalytic conversion of CO<sub>2</sub> in an aqueous solution over Ni-Al layered double hydroxides. *Phys Chem Chem Phys*, 17(27), 17995-18003.
- Ingerslev, F., & Halling - Sørensen, B. (2000). Biodegradability properties of sulfonamides in activated sludge. *Environ. Toxicol. Chem.*, 19(10), 2467-2473.
- Ismail, A. A., & Bahnemann, D. W. (2011). Mesostructured Pt/TiO<sub>2</sub> nanocomposites as highly active photocatalysts for the photooxidation of dichloroacetic acid. *J. Phys. Chem. C*, 115(13), 5784-5791.
- Ismail, A. A., Bahnemann, D. W., Bannat, I., & Wark, M. (2009). Gold nanoparticles on mesoporous interparticle networks of titanium dioxide nanocrystals for enhanced photonic efficiencies. *J. Phys. Chem. C*, 113(17), 7429-7435.
- Ismail, A. A., Bahnemann, D. W., Robben, L., Yarovy, V., & Wark, M. (2009). Palladium doped porous titania photocatalysts: impact of mesoporous order and crystallinity. *Chem. Mater.*, 22(1), 108-116.
- Isse, A. A., Lin, C. Y., Coote, M. L., & Gennaro, A. (2010). Estimation of standard reduction potentials of halogen atoms and alkyl halides. *J. Phys. Chem. B*, 115(4), 678-684.
- Jammoul, A., Dumas, S., D'anna, B., & George, C. (2009). Photoinduced oxidation of sea salt halides by aromatic ketones: a source of halogenated radicals. *Atmospheric Chem. Phys.*, 9(13), 4229-4237.
- Jang, H. D., Kim, S.-K., & Kim, S.-J. (2001). Effect of particle size and phase composition of titanium dioxide nanoparticles on the photocatalytic properties. *J. Nanopart. Res.*, 3(2-3), 141-147.
- Jayalath, S., Wu, H., Larsen, S. C., & Grassian, V. H. (2018). Surface Adsorption of Suwannee River Humic Acid on TiO<sub>2</sub> Nanoparticles: A Study of pH and Particle Size. *Langmuir*, 34(9), 3136-3145.
- Jayson, G., Parsons, B., & Swallow, A. J. (1973). Some simple, highly reactive, inorganic chlorine derivatives in aqueous solution. Their formation using

- pulses of radiation and their role in the mechanism of the Fricke dosimeter. *J. Chem. Soc., Faraday Trans. 1*, 69, 1597-1607.
- Jayson, G. G., Parsons, B. J., & Swallow, A. J. (1973). Some simple, highly reactive, inorganic chlorine derivatives in aqueous solution. Their formation using pulses of radiation and their role in the mechanism of the Fricke dosimeter. *J. Chem. Soc., Faraday Trans. 1*, 69, 1597-1607.
- Jennings, G., & Elia, M. (1996). Automated assay of plasma bromide after a single deproteinization step. *Clin. Chem.*, 42(8), 1210-1213.
- Jia, C., Wang, Y., Zhang, C., Qin, Q., Kong, S., & Kouakou Yao, S. (2012). Photocatalytic degradation of bisphenol A in aqueous suspensions of titanium dioxide. *Environ. Eng. Sci.*, 29(7), 630-637.
- Jia, J., Zhang, J., Wang, F., Han, L., Zhou, J. Z., Mao, B. W., & Zhan, D. (2015). Synergetic effect enhanced photoelectrocatalysis. *Chem Commun (Camb)*, 51(100), 17700-17703.
- Jiang, Y., Goodwill, J. E., Tobiasson, J. E., & Reckhow, D. A. (2016). Bromide oxidation by ferrate(VI): The formation of active bromine and bromate. *Water Res*, 96, 188-197.
- Jing, L., Zhou, J., Durrant, J. R., Tang, J., Liu, D., & Fu, H. (2012). Dynamics of photogenerated charges in the phosphate modified TiO<sub>2</sub> and the enhanced activity for photoelectrochemical water splitting. *Energy & Environmental Science*, 5(4), 6552.
- Khuzwayo, Z., & Chirwa, E. M. N. (2017). The impact of alkali metal halide electron donor complexes in the photocatalytic degradation of pentachlorophenol. *J Hazard Mater*, 321, 424-431.
- Kim, K.-S., Kam, S. K., & Mok, Y. S. (2015). Elucidation of the degradation pathways of sulfonamide antibiotics in a dielectric barrier discharge plasma system. *Chem. Eng. J.*, 271, 31-42.
- Kim, T.-H., Rodríguez-González, V., Gyawali, G., Cho, S.-H., Sekino, T., & Lee, S.-W. (2013). Synthesis of solar light responsive Fe, N co-doped TiO<sub>2</sub> photocatalyst by sonochemical method. *Catalysis today*, 212, 75-80.
- Klán, P., & Wirz, J. (2009). *Photochemistry of organic compounds: from concepts to practice*: John Wiley & Sons.
- Kläning, U. K., & Wolff, T. (1985). Laser Flash Photolysis of HClO, ClO<sup>-</sup>, HBrO, and BrO<sup>-</sup> in Aqueous Solution. Reactions of Cl<sup>-</sup> and Br<sup>-</sup> Atoms. *Berichte der Bunsengesellschaft für physikalische Chemie*, 89(3), 243-245.
- Knorr, F. J., Mercado, C. C., & McHale, J. L. (2008). Trap-State Distributions and Carrier Transport in Pure and Mixed-Phase TiO<sub>2</sub>: Influence of Contacting Solvent and Interphasial Electron Transfer. *J. Phys. Chem. C*, 112,

12786-12794.

- Kosmulski, M. (2011). The pH-dependent surface charging and points of zero charge: V. Update. *J. Colloid Interface Sci.*, 353(1), 1-15.
- Koyuncu, I., Arikan, O. A., Wiesner, M. R., & Rice, C. (2008). Removal of hormones and antibiotics by nanofiltration membranes. *J. Membr. Sci.*, 309(1-2), 94-101.
- Krivec, M., Dillert, R., Bahnemann, D. W., Mehle, A., Strancar, J., & Drazic, G. (2014). The nature of chlorine-inhibition of photocatalytic degradation of dichloroacetic acid in a TiO<sub>2</sub>-based microreactor. *Phys Chem Chem Phys*, 16(28), 14867-14873.
- Kummerer, K. (2009). Antibiotics in the aquatic environment--a review--part I. *Chemosphere*, 75(4), 417-434.
- Kuvarega, A. T., Krause, R. W., & Mamba, B. B. (2013). Photocatalytic performance of nitrogen, osmium co-doped TiO<sub>2</sub> for removal of eosin yellow in water under simulated solar radiation. *J. Nanosci. Nanotechnol.*, 13(7), 5017-5027.
- Kuvarega, A. T., Krause, R. W. M., & Mamba, B. B. (2014). Comparison between Base Metals and Platinum Group Metals in Nitrogen, M Codoped TiO<sub>2</sub> (M = Fe, Cu, Pd, Os) for Photocatalytic Removal of an Organic Dye in Water. *J. Nanomater.*, 2014, 1-12.
- Lakshminarasimhan, N., Kim, W., & Choi, W. (2008). Effect of the agglomerated state on the photocatalytic hydrogen production with in situ agglomeration of colloidal TiO<sub>2</sub> nanoparticles. *J. Phys. Chem. C*, 112(51), 20451-20457.
- Le-Minh, N., Khan, S. J., Drewes, J. E., & Stuetz, R. M. (2010). Fate of antibiotics during municipal water recycling treatment processes. *Water Res*, 44(15), 4295-4323.
- Lee, J.-M., Kim, M.-S., & Kim, B.-W. (2004). Photodegradation of bisphenol-A with TiO<sub>2</sub> immobilized on the glass tubes including the UV light lamps. *Water Res*, 38(16), 3605-3613.
- Lee, J., Choi, W., & Yoon, J. (2005). Photocatalytic degradation of N-nitrosodimethylamine: mechanism, product distribution, and TiO<sub>2</sub> surface modification. *Environ. Sci. Technol.*, 39(17), 6800-6807.
- Lewandowski, M. (2003). Halide acid pretreatments of photocatalysts for oxidation of aromatic air contaminants: rate enhancement, rate inhibition, and a thermodynamic rationale. *J. Catal.*
- Li, F., Kong, Q., Chen, P., Chen, M., Liu, G., Lv, W., & Yao, K. (2017). Effect of halide ions on the photodegradation of ibuprofen in aqueous environments. *Chemosphere*, 166, 412-417.
- Li, G., Liu, X., Zhang, H., An, T., Zhang, S., Carroll, A. R., & Zhao, H. (2011). In situ photoelectrocatalytic generation of bactericide for instant inactivation and

- rapid decomposition of Gram-negative bacteria. *J. Catal.*, 277(1), 88-94.
- Li, Y., Qiao, X., Zhang, Y. N., Zhou, C., Xie, H., & Chen, J. (2016). Effects of halide ions on photodegradation of sulfonamide antibiotics: Formation of halogenated intermediates. *Water Res.*, 102, 405-412.
- Li, Y., Wang, P., Huang, C., Yao, W., Wu, Q., & Xu, Q. (2017). Synthesis and photocatalytic activity of ultrafine Ag<sub>3</sub>PO<sub>4</sub> nanoparticles on oxygen vacated TiO<sub>2</sub>. *Appl. Catal. B.*, 205, 489-497.
- Liang, H. C., Li, X. Z., Yang, Y. H., & Sze, K. H. (2008). Effects of dissolved oxygen, pH, and anions on the 2,3-dichlorophenol degradation by photocatalytic reaction with anodic TiO<sub>2</sub> nanotube films. *Chemosphere*, 73(5), 805-812.
- Liao, C.-H., Kang, S.-F., & Wu, F.-A. (2001). Hydroxyl radical scavenging role of chloride and bicarbonate ions in the H<sub>2</sub>O<sub>2</sub>/UV process. *Chemosphere*, 44(5), 1193-1200.
- Lim, S. P., Pandikumar, A., Lim, H. N., Ramaraj, R., & Huang, N. M. (2015). Boosting Photovoltaic Performance of Dye-Sensitized Solar Cells Using Silver Nanoparticle-Decorated N,S-Co-Doped-TiO<sub>2</sub> Photoanode. *Sci Rep*, 5, 11922.
- Lin, C.-E., Chang, C.-C., & Lin, W.-C. (1997). Migration behavior and separation of sulfonamides in capillary zone electrophoresis III. Citrate buffer as a background electrolyte *J. Chromatogr. A*, 768, 105-112.
- Lin, H., Huang, C., Li, W., Ni, C., Shah, S., & Tseng, Y. (2006). Size dependency of nanocrystalline TiO<sub>2</sub> on its optical property and photocatalytic reactivity exemplified by 2-chlorophenol. *Appl. Catal. B.*, 68(1-2), 1-11.
- Liu, H., Zhao, H., Quan, X., Zhang, Y., & Chen, S. (2009). Formation of chlorinated intermediate from bisphenol A in surface saline water under simulated solar light irradiation. *Environ. Sci. Technol.*, 43(20), 7712-7717.
- Luther, G. W., Swartz, C. B., & Ullman, W. J. (1988). Direct determination of iodide in seawater by cathodic stripping square wave voltammetry. *Anal. Chem.*, 60(17), 1721-1724.
- Méndez-Díaz, J. D., Shimabuku, K. K., Ma, J., Enumah, Z. O., Pignatello, J. J., Mitch, W. A., & Dodd, M. C. (2014). Sunlight-driven photochemical halogenation of dissolved organic matter in seawater: a natural abiotic source of organobromine and organoiodine. *Environ. Sci. Technol.*, 48(13), 7418-7427.
- Maira, A., Yeung, K. L., Lee, C., Yue, P. L., & Chan, C. K. (2000). Size effects in gas-phase photo-oxidation of trichloroethylene using nanometer-sized TiO<sub>2</sub> catalysts. *J. Catal.*, 192(1), 185-196.
- Marczenko, Z., & Balcerzak, M. (2000). Bromine *Analytical Spectroscopy Library* (Vol. 10, pp. 129-132): Elsevier.



- Marotta, E., Ceriani, E., Schiorlin, M., Ceretta, C., & Paradisi, C. (2012). Comparison of the rates of phenol advanced oxidation in deionized and tap water within a dielectric barrier discharge reactor. *Water Res*, 46(19), 6239-6246.
- Matthew, B., & Anastasio, C. (2006). A chemical probe technique for the determination of reactive halogen species in aqueous solution: Part 1—bromide solutions. *Atmos. Chem. Phys.*, 6(9), 2423-2437.
- Matthew, B. M., & Anastasio, C. (2006). A chemical probe technique for the determination of reactive halogen species in aqueous solution: Part 1 - bromide solutions. *Atmos. Chem. Phys.*, 6, 2423-2437.
- Matthew, B. M., George, I., & Anastasio, C. (2003). Hydroperoxyl radical ( $\text{HO}_2\cdot$ ) oxidizes dibromide radical anion ( $\text{Br}_2^-$ ) to bromine ( $\text{Br}_2$ ) in aqueous solution: Implications for the formation of  $\text{Br}_2$  in the marine boundary layer. *Geophysical research letters*, 30(24).
- Merenyi, G., & Lind, J. (1994). Reaction Mechanism of Hydrogen Abstraction by the Bromine Atom in Water *J. Am. Chem. Soc.*, 116, 7872-7876.
- Michael, I., Rizzo, L., McArdell, C. S., Manaia, C. M., Merlin, C., Schwartz, T., Dagot, C., & Fatta-Kassinos, D. (2013). Urban wastewater treatment plants as hotspots for the release of antibiotics in the environment: a review. *Water Res*, 47(3), 957-995.
- Minero, C., Mariella, G., Maurino, V., Vione, D., & Pelizzetti, E. (2000). Photocatalytic Transformation of Organic Compounds in the Presence of Inorganic Ions. 2. Competitive Reactions of Phenol and Alcohols on a Titanium Dioxide-Fluoride System. *Langmuir*, 16, 8964-8972.
- Moberg, L., & Karlberg, B. (2000). An improved *N,N'*-diethyl-*p*-phenylenediamine (DPD) method for the determination of free chlorine based on multiple wavelength detection. *Anal. Chim. Acta*, 407, 127-133.
- Moore, H. E., Garmendia, M. J., & Cooper, W. J. (1984). Kinetics of monochloramine oxidation of *N,N'*-diethyl-*p*-phenylenediamine. *Environ. Sci. Technol.*, 18(5), 348-353.
- Mopper, K., & Zhou, X. (1990). Hydroxyl radical photoproduction in the sea and its potential impact on marine processes. *Science*, 250(4981), 661-664.
- Nakata, K., & Fujishima, A. (2012).  $\text{TiO}_2$  photocatalysis: Design and applications. *J. Photoch. Photobio. C.*, 13(3), 169-189.
- Nakato, Y., Tsumura, A., & Tsubomura, H. (1983). Photo-and electroluminescence spectra from an n-titanium dioxide semiconductor electrode as related to the intermediates of the photooxidation reaction of water. *J. Phys. Chem.*, 87(13), 2402-2405.
- Nasuhoglu, D., Yargeau, V., & Berk, D. (2011). Photo-removal of sulfamethoxazole

- (SMX) by photolytic and photocatalytic processes in a batch reactor under UV-C radiation ( $\lambda_{\text{max}}=254$  nm). *J Hazard Mater*, 186(1), 67-75.
- Newton, G. L., & Milligan, J. R. (2006). Fluorescence detection of hydroxyl radicals. *Radiat. Phys. Chem.*, 75(4), 473-478.
- Ng, T. W., Li, B., Chow, A., & Wong, P. K. (2016). Effects of bromide on inactivation efficacy and disinfection byproduct formation in photocatalytic inactivation. *J. photochem. photobiol. A*, 324, 145-151.
- Nokes, C. J., Fenton, E., & Randall, C. J. (1999). Modelling the formation of brominated trihalomethanes in chlorinated drinking waters. *Water Res*, 33(17), 3557-3568.
- Nosaka, Y., & Nosaka, A. Y. (2017). Generation and Detection of Reactive Oxygen Species in Photocatalysis. *Chem Rev*, 117(17), 11302-11336.
- Oosting, M., & Reijnders, H. F. R. (1980). Spectrophotometric Determination of Bromide in Aqueous Solutions. *Fresenius Z. Anal. Chem.*, 301, 28-29.
- Ou, B., Hampsch-Woodill, M., Flanagan, J., Deemer, E. K., Prior, R. L., & Huang, D. (2002). Novel fluorometric assay for hydroxyl radical prevention capacity using fluorescein as the probe. *Journal of agricultural and food chemistry*, 50(10), 2772-2777.
- Ou, B., Hampsch-Woodill, M., & Prior, R. L. (2001). Development and validation of an improved oxygen radical absorbance capacity assay using fluorescein as the fluorescent probe. *Journal of agricultural and food chemistry*, 49(10), 4619-4626.
- Pérez, S., Eichhorn, P., & Aga, D. S. (2005). Evaluating the biodegradability of sulfamethazine, sulfamethoxazole, sulfathiazole, and trimethoprim at different stages of sewage treatment. *Environ. Toxicol. Chem.*, 24(6), 1361-1367.
- Padhye, L. P., Yao, H., Kung'u, F. T., & Huang, C. H. (2014). Year-long evaluation on the occurrence and fate of pharmaceuticals, personal care products, and endocrine disrupting chemicals in an urban drinking water treatment plant. *Water Res*, 51, 266-276.
- Palin, A. (1975). Current DPD methods for residual halogen compounds and ozone in water. *Journal-American Water Works Association*, 67(1), 32-33.
- Panwar, K., Jassal, M., & Agrawal, A. K. (2016). TiO<sub>2</sub>-SiO<sub>2</sub> Janus particles with highly enhanced photocatalytic activity. *RSC Advances*, 6(95), 92754-92764.
- Park, H., & Choi, W. (2004). Effects of TiO<sub>2</sub> Surface Fluorination on Photocatalytic Reactions and Photoelectrochemical Behaviors. *J. Phys. Chem. B*, 108, 4086-4093.
- Park, Y., Kim, W., Monllor-Satoca, D., Tachikawa, T., Majima, T., & Choi, W. (2013). Role of Interparticle Charge Transfers in Agglomerated Photocatalyst

- Nanoparticles: Demonstration in Aqueous Suspension of Dye-Sensitized TiO<sub>2</sub>. *J Phys Chem Lett*, 4(1), 189-194.
- Park, Y., Singh, N. J., Kim, K. S., Tachikawa, T., Majima, T., & Choi, W. (2009). Fullerol-titania charge-transfer-mediated photocatalysis working under visible light. *Chemistry*, 15(41), 10843-10850.
- Parker, K. M., Pignatello, J. J., & Mitch, W. A. (2013). Influence of ionic strength on triplet-state natural organic matter loss by energy transfer and electron transfer pathways. *Environ. Sci. Technol.*, 47(19), 10987-10994.
- Peng, Y.-H., Tsai, Y.-C., Hsiung, C.-E., Lin, Y.-H., & Shih, Y.-h. (2017). Influence of water chemistry on the environmental behaviors of commercial ZnO nanoparticles in various water and wastewater samples. *J Hazard Mater*, 322, 348-356.
- Peng, Y.-H., Tso, C.-p., Tsai, Y.-c., Zhuang, C.-m., & Shih, Y.-h. (2015). The effect of electrolytes on the aggregation kinetics of three different ZnO nanoparticles in water. *Sci. Total Environ.*, 530, 183-190.
- Pignatello, J. J. (1992). Dark and photoassisted iron<sup>3+</sup>-catalyzed degradation of chlorophenoxy herbicides by hydrogen peroxide. *Environ. Sci. Technol.*, 26(5), 944-951.
- Pratt, K. A., Custard, K. D., Shepson, P. B., Douglas, T. A., Pöhler, D., General, S., Zielcke, J., Simpson, W. R., Platt, U., & Tanner, D. J. (2013). Photochemical production of molecular bromine in Arctic surface snowpacks. *Nature Geosci.*, 6(5), 351.
- Ramjaun, S. N., Yuan, R., Wang, Z., & Liu, J. (2011). Degradation of reactive dyes by contact glow discharge electrolysis in the presence of Cl<sup>-</sup> ions: kinetics and AOX formation. *Electrochim. Acta*, 58, 364-371.
- Ray, J. R., Lee, B., Baltrusaitis, J., & Jun, Y.-S. (2012). Formation of iron (III)(hydr)oxides on polyaspartate-and alginate-coated substrates: effects of coating hydrophilicity and functional group. *Environ. Sci. Technol.*, 46(24), 13167-13175.
- Reichman, B., & Byvik, C. E. (1981). Photoproduction of I<sub>2</sub>, Br<sub>2</sub>, and Cl<sub>2</sub> on n-semiconducting powder. *J. Phys. Chem.*, 85(15), 2255-2258.
- Ritchie, J. D., & Perdue, E. M. (2003). Proton-binding study of standard and reference fulvic acids, humic acids, and natural organic matter. *Geochim. Cosmochim. Acta.*, 67(1), 85-96.
- Rodríguez, E. M., Márquez, G., Tena, M., Álvarez, P. M., & Beltrán, F. J. (2015). Determination of main species involved in the first steps of TiO<sub>2</sub> photocatalytic degradation of organics with the use of scavengers: The case of ofloxacin. *Appl. Catal. B.*, 178, 44-53.

- Rook, J. J., Gras, A., Van der Heijden, B., & De Wee, J. (1978). Bromide oxidation and organic substitution in water treatment. *J. Environ. Sci. Heal. A*, 13(2), 91-116.
- Ross, A. B., Bielski, B. H. J., Buxton, G. V., Cabelli, D. E., Helman, W. P., Huie, R. E., Grodkowski, J., Neta, P., Mulazzani, Q. G., & Wilkinson, F. (1998). NIST Standard Reference Database 40: NDRL/NIST Solution Kinetics Database V. 3.0.
- Ross, A. B., Mallard, W. G., Helman, W. P., Buxton, G. V., Huie, R. E., & Neta, P. (1998). NDRL-NIST solution kinetics database. *Ver 2 NIST Standard Reference Data*.
- Salimi, R., Yener, N., & Safari, R. (2016). Use and Evaluation of Newly Synthesized Fluorescence Probes to Detect Generated OH• Radicals in Fibroblast Cells. *J Fluoresc*, 26(3), 919-924.
- Savory, D. M., Warren, D. S., & McQuillan, A. J. (2010). Shallow electron trap, interfacial water, and outer-sphere adsorbed oxalate IR absorptions correlate during UV irradiation of photocatalytic TiO<sub>2</sub> films in aqueous solution. *J. Phys. Chem. C*, 115(4), 902-907.
- Segets, D., Marczak, R., Schäfer, S., Paula, C., Gnichwitz, J.-F., Hirsch, A., & Peukert, W. (2011). Experimental and theoretical studies of the colloidal stability of nanoparticles— a general interpretation based on stability maps. *ACS nano*, 5(6), 4658-4669.
- Selcuk, H., Sarikaya, H. Z., Bekbolet, M., & Anderson, M. A. (2006). Bromate formation on the non-porous TiO<sub>2</sub> photoanode in the photoelectrocatalytic system. *Chemosphere*, 62(5), 715-721.
- Serpone, N. (1995). Brief introductory remarks on heterogeneous photocatalysis. *Sol. Energ. Mat. Sol. C.*, 38(1-4), 369-379.
- Shaw, H., Perlmutter, H. D., & Gu, C. (1997). Free-Radical Bromination of Selected Organic Compounds in Water. *J. Org. Chem.*, 62, 236-237.
- Sheridan, M. V., Wang, Y., Wang, D., Troian-Gautier, L., Dares, C. J., Sherman, B. D., & Meyer, T. J. (2018). Light-Driven Water Splitting Mediated by Photogenerated Bromine. *Angew Chem Int Ed Engl*, 57(13), 3449-3453.
- Shu, Y., Qiwu, Z., Fumio, S., & Tsugio, S. (2003). Preparation of Visible Light-Activated Titania Photocatalyst by Mechanochemical Method. *Chemistry Letters*, 32(4), 358-359.
- Sin, J.-C., Lam, S.-M., Mohamed, A. R., & Lee, K.-T. (2012). Degrading Endocrine Disrupting Chemicals from Wastewater by TiO<sub>2</sub> Photocatalysis: A Review. *Int. J. Photoenergy*, 2012.
- Sojic, D. V., Anderluh, V. B., Orcic, D. Z., & Abramovic, B. F. (2009).

- Photodegradation of clopyralid in TiO<sub>2</sub> suspensions: identification of intermediates and reaction pathways. *J Hazard Mater*, 168(1), 94-101.
- Šojić, D. V., Anderluh, V. B., Orčić, D. Z., & Abramović, B. F. (2009). Photodegradation of clopyralid in TiO<sub>2</sub> suspensions: Identification of intermediates and reaction pathways. *J Hazard Mater*, 168(1), 94-101.
- Song, Y., Tian, J., Gao, S., Shao, P., Qi, J., & Cui, F. (2017). Photodegradation of sulfonamides by g-C<sub>3</sub>N<sub>4</sub> under visible light irradiation: Effectiveness, mechanism and pathways. *Appl. Catal. B.*, 210, 88-96.
- Su, Y.-f., Wang, G.-B., Kuo, D. T. F., Chang, M.-l., & Shih, Y.-h. (2016). Photoelectrocatalytic degradation of the antibiotic sulfamethoxazole using TiO<sub>2</sub>/Ti photoanode. *Appl. Catal. B.*, 186, 184-192.
- Sun, L., Chen, L., Sun, X., Du, X., Yue, Y., He, D., Xu, H., Zeng, Q., Wang, H., & Ding, L. (2009). Analysis of sulfonamides in environmental water samples based on magnetic mixed hemimicelles solid-phase extraction coupled with HPLC-UV detection. *Chemosphere*, 77(10), 1306-1312.
- Sutton, H. C., Adams, G. E., Boag, J. W., & Michael, B. D. (1965). Radical yields and kinetics in the pulse radiolysis of potassium bromide solutions. *Pulse Radiolysis (M. Ebert, JP Keene, AJ Swallow, and JH Baxendale, Eds.)*, 61-81.
- Tang, H., Berger, H., Schmid, P., & Levy, F. (1994). Optical properties of anatase (TiO<sub>2</sub>). *Solid State Commun.*, 92(3), 267-271.
- Tissot, H., Olivieri, G., Gallet, J.-J., Bournel, F., Silly, M. G., Sirotti, F., & Rochet, F. (2015). Cation Depth-Distribution at Alkali Halide Aqueous Solution Surfaces. *J. Phys. Chem. C*, 119(17), 9253-9259.
- Tsujiko, A., Kisumi, T., Magari, Y., Murakoshi, K., & Nakato, Y. (2000). Selective formation of nanoholes with (100)-face walls by photoetching of n-TiO<sub>2</sub> (rutile) electrodes, accompanied by increases in water-oxidation photocurrent. *J. Phys. Chem. B*, 104(20), 4873-4879.
- Vikesland, P. J., Fiss, E. M., Wigginton, K. R., McNeill, K., & Arnold, W. A. (2013). Halogenation of bisphenol-A, triclosan, and phenols in chlorinated waters containing iodide. *Environ. Sci. Technol.*, 47(13), 6764-6772.
- Wagner, I., & Strehlow, H. (1987). On the flash photolysis of bromide ions in aqueous solutions. *Berichte der Bunsengesellschaft für physikalische Chemie*, 91(12), 1317-1321.
- Wang, C.-y., Böttcher, C., Bahnemann, D. W., & Dohrmann, J. K. (2003). A comparative study of nanometer sized Fe(iii)-doped TiO<sub>2</sub> photocatalysts: synthesis, characterization and activity. *J. Mater. Chem.*, 13(9), 2322-2329.
- Wang, K.-H., Hsieh, Y.-H., Wu, C.-H., & Chang, C.-Y. (2000). The pH and anion effects on the heterogeneous photocatalytic degradation of o-methylbenzoic

- acid in TiO<sub>2</sub> aqueous suspension. *Chemosphere*, 40, 389-394.
- Wang, P. (2017). Ag-AgBr/TiO<sub>2</sub>/RGO nanocomposite: Synthesis, characterization, photocatalytic activity and aggregation evaluation. *J Environ Sci (China)*, 56, 202-213.
- Wang, R., Hashimoto, K., Fujishima, A., Chikuni, M., Kojima, E., Kitamura, A., Shimohigoshi, M., & Watanabe, T. (1997). Light-induced amphiphilic surfaces. *Nature*, 388(6641), 431.
- Westerhoff, P., Chao, P., & Mash, H. (2004). Reactivity of natural organic matter with aqueous chlorine and bromine. *Water Res*, 38(6), 1502-1513.
- Wu, X., Huang, Y. Y., Kushida, Y., Bhayana, B., & Hamblin, M. R. (2016). Broad-spectrum antimicrobial photocatalysis mediated by titanium dioxide and UVA is potentiated by addition of bromide ion via formation of hypobromite. *Free Radic Biol Med*, 95, 74-81.
- Wu, Z., Guo, K., Fang, J., Yang, X., Xiao, H., Hou, S., Kong, X., Shang, C., Yang, X., Meng, F., & Chen, L. (2017). Factors affecting the roles of reactive species in the degradation of micropollutants by the UV/chlorine process. *Water Res*, 126, 351-360.
- Xekoukoulotakis, N. P., Drosou, C., Brebou, C., Chatzisyneon, E., Hapeshi, E., Fatta-Kassinou, D., & Mantzavinos, D. (2011). Kinetics of UV-A/TiO<sub>2</sub> photocatalytic degradation and mineralization of the antibiotic sulfamethoxazole in aqueous matrices. *Catalysis today*, 161(1), 163-168.
- Yang, K., Lin, D., & Xing, B. (2009). Interactions of humic acid with nanosized inorganic oxides. *Langmuir*, 25(6), 3571-3576.
- Yang, S. Y., Chen, Y. X., Lou, L. P., & Wu, X. N. (2005). Involvement of chloride anion in the photocatalytic process. *J. Environ. Sci.*, 17, 761-765.
- Yang, Y., & Pignatello, J. J. (2017). Participation of the Halogens in Photochemical Reactions in Natural and Treated Waters. *Molecules*, 22(10).
- Yu, H., Miller, C. J., Ikeda-Ohno, A., & Waite, T. D. (2014). Photodegradation of contaminants using Ag@AgCl/rGO assemblages: Possibilities and limitations. *Catalysis today*, 224, 122-131.
- Yuan, R., Chen, T., Fei, E., Lin, J., Ding, Z., Long, J., Zhang, Z., Fu, X., Liu, P., & Wu, L. (2011). Surface chlorination of TiO<sub>2</sub>-based photocatalysts: a way to remarkably improve photocatalytic activity in both UV and visible region. *ACS Catalysis*, 1(3), 200-206.
- Yuan, R., Ramjaun, S. N., Wang, Z., & Liu, J. (2012). Photocatalytic degradation and chlorination of azo dye in saline wastewater: kinetics and AOX formation. *Chem. Eng. J.*, 192, 171-178.
- Yurdakal, S., Loddo, V., Ferrer, B. B., Palmisano, G., Augugliaro, V., Farreras, J. G.,

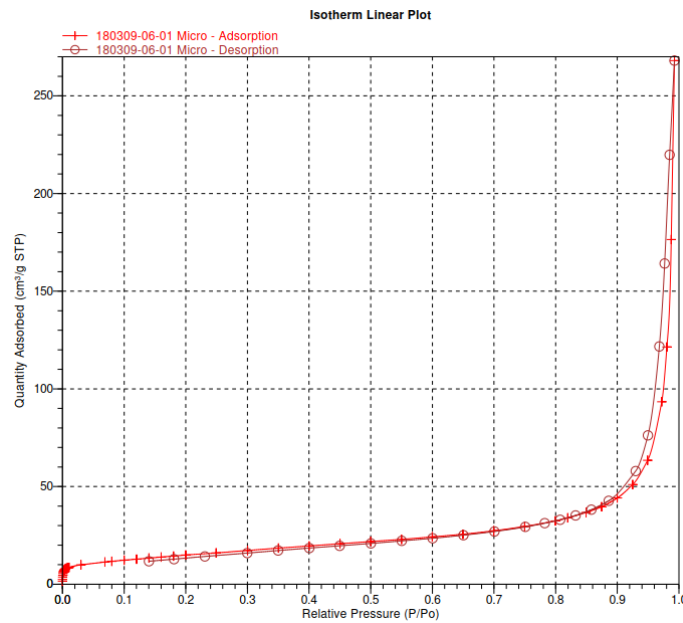
- & Palmisano, L. (2007). Optical Properties of TiO<sub>2</sub> Suspensions: Influence of pH and Powder Concentration on Mean Particle Size. *Ind. Eng. Chem. Res.*, 46(23), 7620-7626.
- Zabicky, J., & Nutkovitch, M. (1986). Reactions of Bromine and Cyclohexene in Aqueous Media. Selectivity of Bromohydrin vs. Dibromo Adduct Formation. *Ind. Eng. Chem. Prod. Res. Dev.*, 25(2), 372-375.
- Zafiriou, O. C. (1974). Sources and reactions of OH and daughter radicals in seawater. *J. Geophys. Res.*, 79(30), 4491-4497.
- Zehavi, D., & Rabani, J. (1972). Oxidation of aqueous bromide ions by hydroxyl radicals. Pulse radiolytic investigation. *J. Phys. Chem.*, 76(3), 312-319.
- Zhang, C., Hua, H., Liu, J., Han, X., Liu, Q., Wei, Z., Shao, C., & Hu, C. (2017). Enhanced Photocatalytic Activity of Nanoparticle-Aggregated Ag-AgX(X = Cl, Br)@TiO<sub>2</sub> Microspheres Under Visible Light. *Nano-Micro Letters*, 9(4).
- Zhang, F., Li, M., Li, W., Feng, C., Jin, Y., Guo, X., & Cui, J. (2011). Degradation of phenol by a combined independent photocatalytic and electrochemical process. *Chem. Eng. J.*, 175, 349-355.
- Zhang, J., & Nosaka, Y. (2013). Quantitative Detection of OH Radicals for Investigating the Reaction Mechanism of Various Visible-Light TiO<sub>2</sub> Photocatalysts in Aqueous Suspension. *J. Phys. Chem. C*, 117(3), 1383-1391.
- Zhang, J., & Nosaka, Y. (2014). Mechanism of the OH Radical Generation in Photocatalysis with TiO<sub>2</sub> of Different Crystalline Types. *J. Phys. Chem. C*, 118(20), 10824-10832.
- Zhang, J., & Nosaka, Y. (2015). Photocatalytic oxidation mechanism of methanol and the other reactants in irradiated TiO<sub>2</sub> aqueous suspension investigated by OH radical detection. *Appl. Catal. B.*, 166-167, 32-36.
- Zhang, Y., & Meshnick, S. (1991). Inhibition of Plasmodium falciparum dihydropteroate synthetase and growth in vitro by sulfa drugs. *Antimicrob. Agents Chemother.*, 35(2), 267-271.
- Zhang, Z., Wang, C.-C., Zakaria, R., & Ying, J. Y. (1998). Role of particle size in nanocrystalline TiO<sub>2</sub>-based photocatalysts. *J. Phys. Chem. B*, 102(52), 10871-10878.
- Zhou, X., & Mopper, K. (1990). Determination of photochemically produced hydroxyl radicals in seawater and freshwater. *Marine Chemistry*, 30, 71-88.

# Appendix

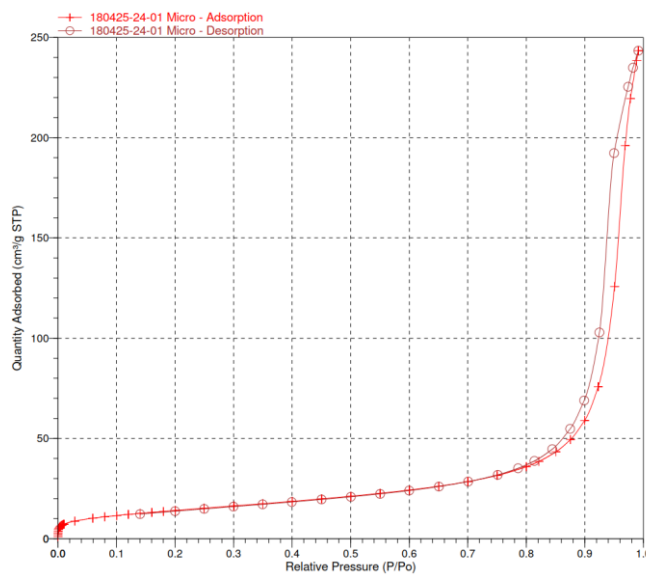


The light intensity of each UV lamp is 882 lux at maximum and 832 lux at minimum.

The adsorption and desorption of nitrogen gas isotherms of P25, HBr-P25, HCl-P25, NaBr-P25 and NaCl-P25 are shown in Appendix 1 – 5, respectively.

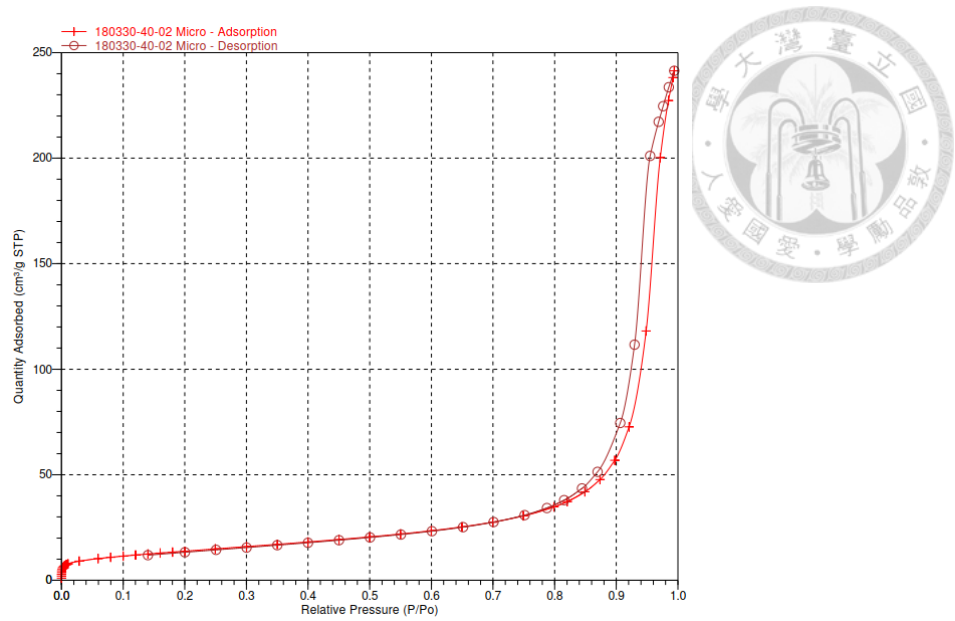


Appendix 1. Adsorption and desorption of nitrogen gas isotherms of P25.

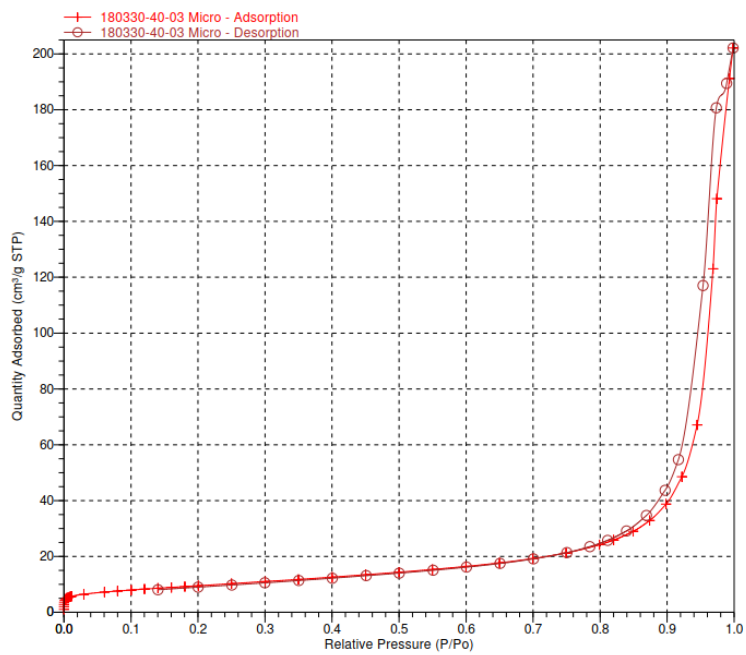


Appendix 2. Adsorption and desorption of nitrogen gas isotherms of HBr-P25.

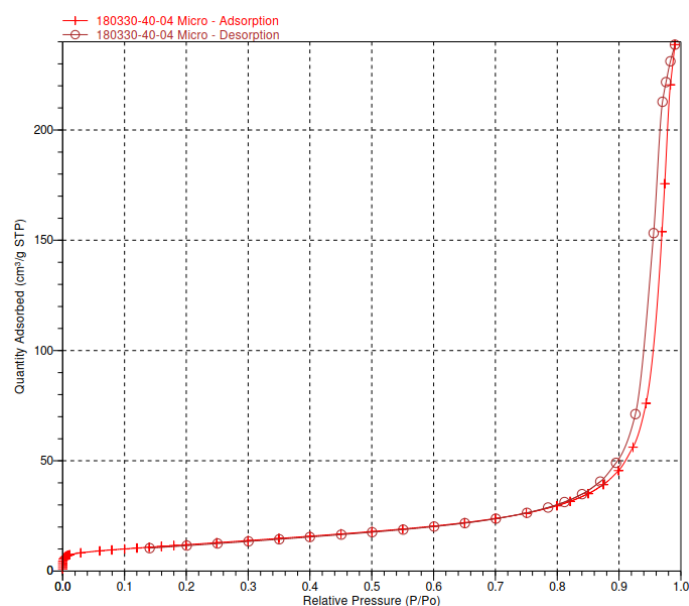




Appendix 3. Adsorption and desorption of nitrogen gas isotherms of HCl-P25.



Appendix 4. Adsorption and desorption of nitrogen gas isotherms of NaBr-P25.

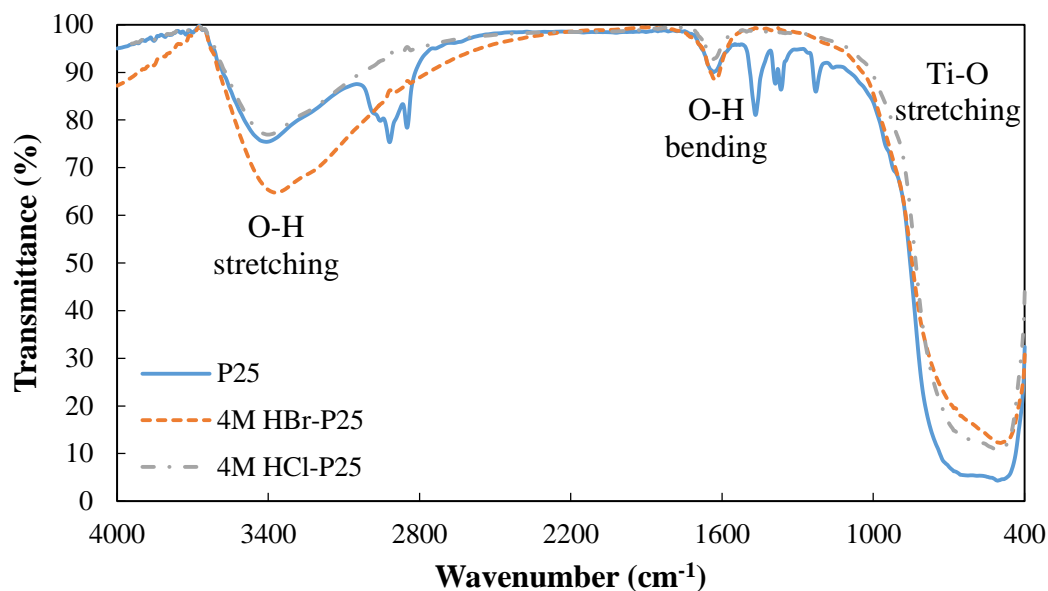


#### Appendix 5. Adsorption and desorption of nitrogen gas isotherms of NaCl-P25.

Another sample of surface brominated  $\text{TiO}_2$  with higher  $\text{Br}^-$  concentration was synthesized by impregnation of 0.3 g of P25 into 1 mL of 4 M HBr, followed by a drying process at room temperature in the hood for about 4 hr, and with a further 60 °C drying in the oven for 5 days. Once the drying was completed, the catalyst samples were ground using a mortar and pestle to break up agglomerates and to prepare the titania for use in photocatalytic experiments. As for surface chlorination of  $\text{TiO}_2$  with higher  $\text{Cl}^-$  concentration, 4M HCl was used in the same process.

The FTIR spectra of 4M HBr-P25 and HCl-P25 were shown in Appendix 6. Peaks at  $3400\text{ cm}^{-1}$  and  $1635\text{ cm}^{-1}$  can be ascribed to OH stretching of the surface hydroxyls and the OH bending vibrations of adsorbed water molecules on the  $\text{TiO}_2$  nanoparticles, respectively. The broad peak in the range  $750\text{--}520\text{ cm}^{-1}$ , observed in all the samples, is due to stretching vibration of Ti–O. HBr and HCl molecules were chemisorbed on the surface of the partially hydroxylated  $\text{TiO}_2$  (P25) by an ion-exchange reaction between the bromine, chlorine and hydroxyl groups, respectively. Yuan et al. (2011) explained the chemisorption by FTIR spectra,

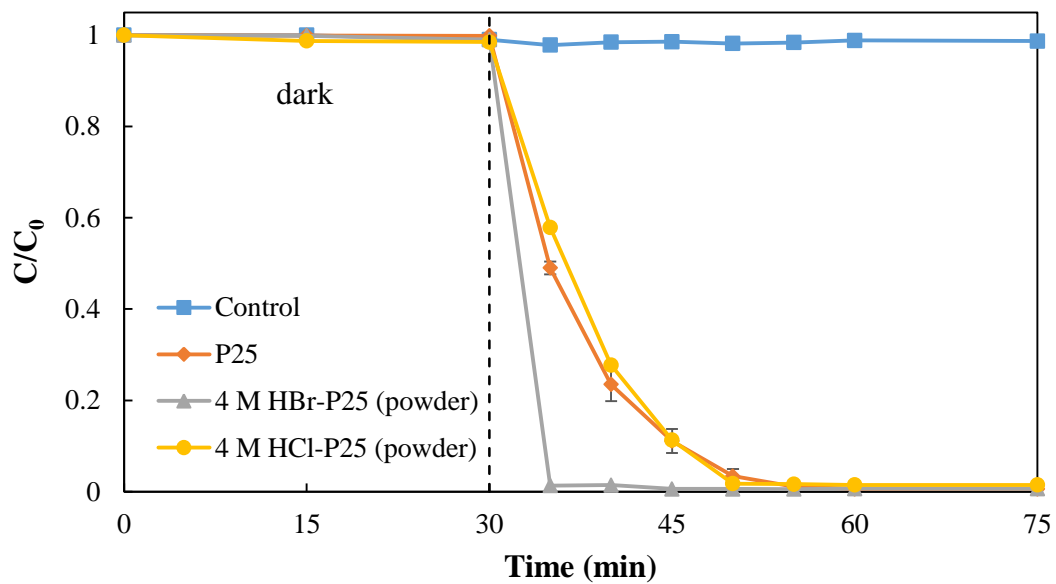
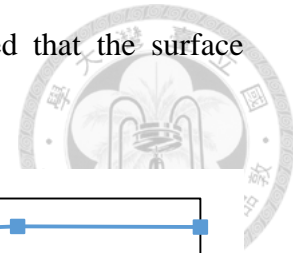
suggesting that there was a significant decrease for the band at  $3424\text{ cm}^{-1}$  corresponding to O-H stretching modes due to the substitution of bromine and chlorine groups for hydroxyl groups. However, this phenomenon could not be observed in 4 M HBr-P25 and 4 M HCl-P25.



#### Appendix 6. FTIR spectra of different types of $\text{TiO}_2$ .

The effect of surface modified P25 with higher  $\text{Br}^-$  and  $\text{Cl}^-$  concentration on the degradation of SMZ solution was investigated under UV irradiation. The results were shown in Appendix 7. In the absence of photocatalysts, the SMZ concentration was not changed obviously, indicating that no adsorption of SMZ on P25 in dark was found. The photocatalytic degradation efficiency of 5 mg/L SMZ by 0.3 g/L P25 was 99 % after UV light irradiation for 30 min. As for the effect of 4 M HCl-P25, the photodegradation of SMZ was similar to P25 but slightly inhibited in the beginning. Compared to pure P25, the photocatalytic degradation of SMZ with 4 M HBr-P25 was significantly enhanced with a steep slope. Within just 5 min of irradiation, SMZ degradation efficiency increased sharply to 99 %, and reached equilibrium at 10 min.

The increase of photodegradation rate by 4 M HBr-P25 implied that the surface reaction has significant effect on the enhancement.

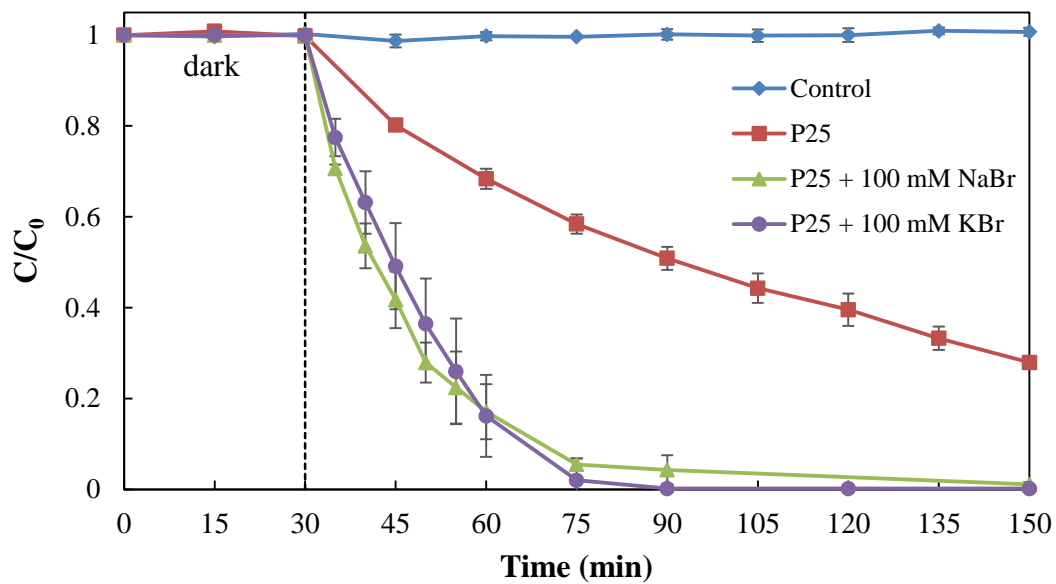
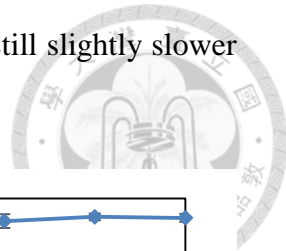


Appendix 7. The photocatalytic degradation of 5 mg/L SMZ by 0.3 g/L P25, 4 M HBr-P25 and 4 M HCl-P25 under UV light.

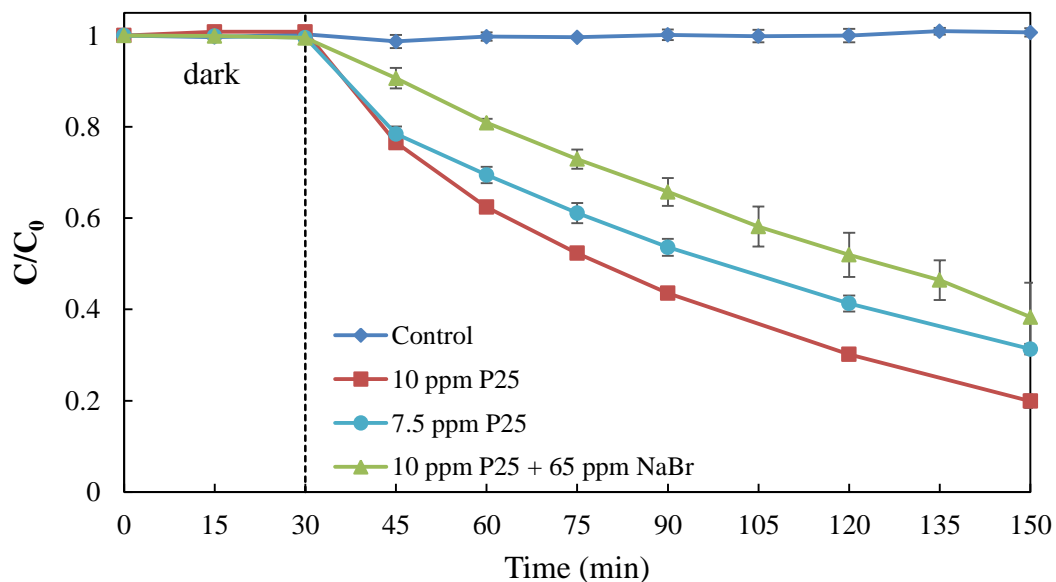
Cation does not affect the photocatalytic degradation of SMZ. As shown in Appendix 8, the cation,  $K^+$  or  $Na^+$ , did not have the influence on the enhanced photodegradation of SMZ by P25 with the addition of  $Br^-$ .

Bromide ions are ubiquitous in natural waters. An ordinary level of bromide in seawater is 65 ppm (Luther et al., 1988). The bromide level range downward in estuaries and upward in saltier water bodies relative to typical seawater levels. Surface fresh water and groundwater may contain up to 0.05 mM bromide (Grebel et al., 2010), with higher levels in some places. As for the ordinary condition in seawater, the photocatalytic degradation of SMZ by P25 with 65 ppm NaBr was conducted (Appendix 9). Considering the sedimentation of P25 with NaBr (Figure 4-12), the dosage of 7.5 mg/L P25 was performed to avoid the sedimentation effect. However,

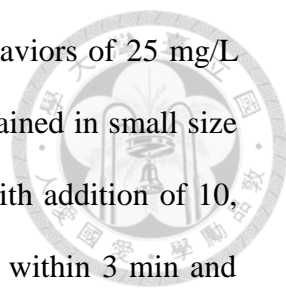
the photodegradation rate of SMZ by P25 with 65 ppm NaBr was still slightly slower than the rate by 7.5 mg/L P25.



Appendix 8. The photocatalytic degradation of 5 mg/L SMZ by 10 mg/L P25 with addition of 100 mM KBr and NaBr under UV light irradiation.

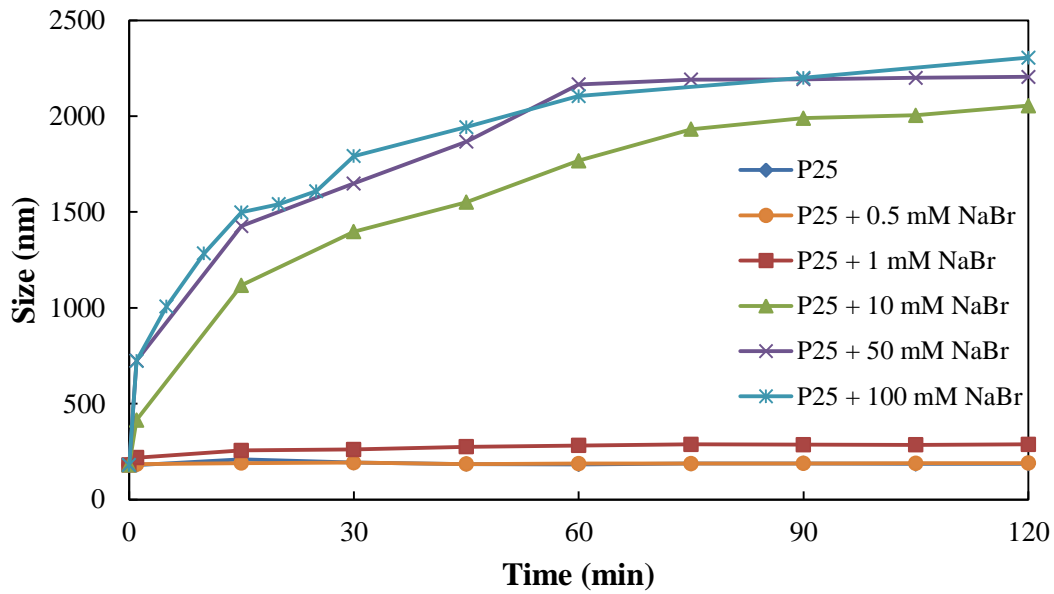


Appendix 9. The photocatalytic degradation of 5 mg/L SMZ by different concentrations of P25 with NaBr under UV light irradiation. (UV light:  $\lambda = 365$  nm)

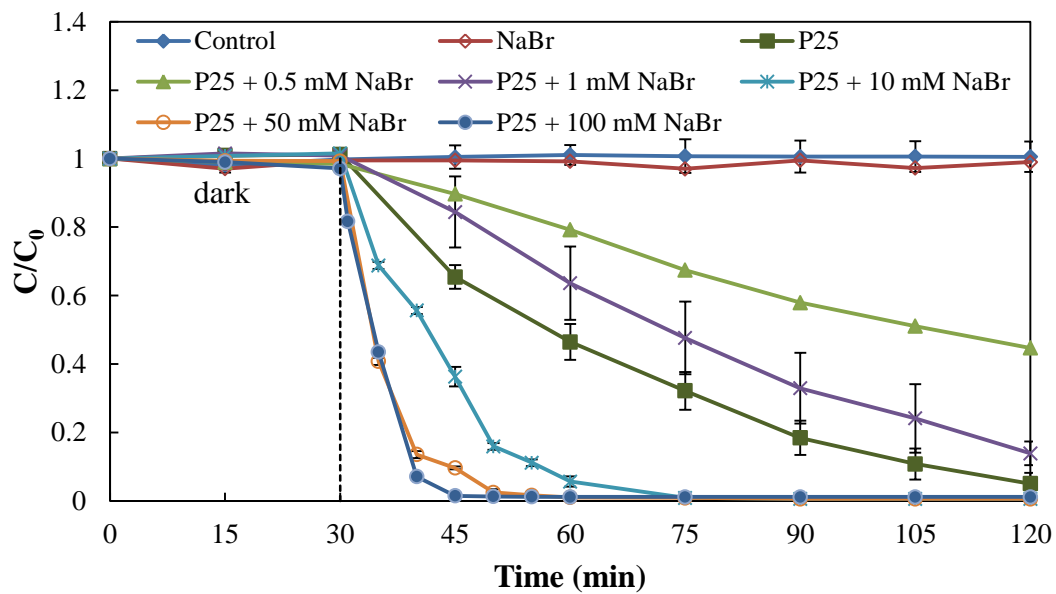


The effect of NaBr on the aggregation and sedimentation behaviors of 25 mg/L P25 NPs was also investigated. Appendix 10 showed that P25 remained in small size (about 180 nm) without NaBr addition and was well-dispersed. With addition of 10, 50 and 100 mM NaBr, the particle sizes of P25 increased quickly within 3 min and exceeded 1000 nm after 15 min. However, with addition of 0.5 and 1 mM NaBr, the particle sizes of P25 almost kept the same as pure P25.

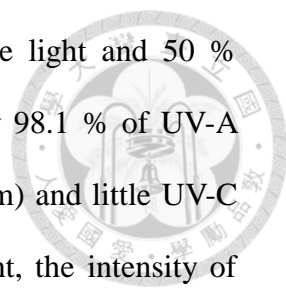
The effect of NaBr concentration on the degradation of SMZ solution by 25 mg/L P25 was investigated under UV irradiation (Appendix 11). In the control experiment, when SMZ was irradiated with UV light in the absence of P25, the changes in SMZ concentration was insignificant, indicating that no adsorption of SMZ on TiO<sub>2</sub> in dark. The photocatalytic degradation efficiency of SMZ by P25 was 99 % after UV light irradiation for 90 min, and the rate constant was 0.0297 min<sup>-1</sup>. When there was NaBr in the solution, TiO<sub>2</sub> aggregated and became larger particle agglomerates (Appendix 10), resulting in the decrease of surface area and active site on the surface. However, the photodegradation rate of SMZ by TiO<sub>2</sub> with the addition of NaBr increased instead of decreasing. Appendix 11 presented that the SMZ degradation rate was accelerated in the presence of 10, 50 and 100 mM NaBr under UV irradiation. With the addition of 100 mM NaBr, the photodegradation efficiency was 99 % after just 15 min illumination, and reached degradation equilibrium. The photodegradation rate constant of 25 mg/L P25 was 0.0297 min<sup>-1</sup>, increasing to 0.300 min<sup>-1</sup> with the addition of 100 mM NaBr. On the other hand, in the presence of 0.5 and 1 mM NaBr, the photodegradation was slightly inhibited. The photodegradation rate of SMZ by 25 mg/L P25 with 0.5 mM NaBr decreased to 0.0092 min<sup>-1</sup>.



Appendix 10. Aggregation kinetics of 25 mg/L P25 with different NaBr concentrations in 5 mg/L SMZ solutions.



Appendix 11. The photocatalytic degradation of 5 mg/L SMZ by 25 mg/L P25 at different NaBr concentrations under UV light. (UV light:  $\lambda = 365$  nm, 32W)

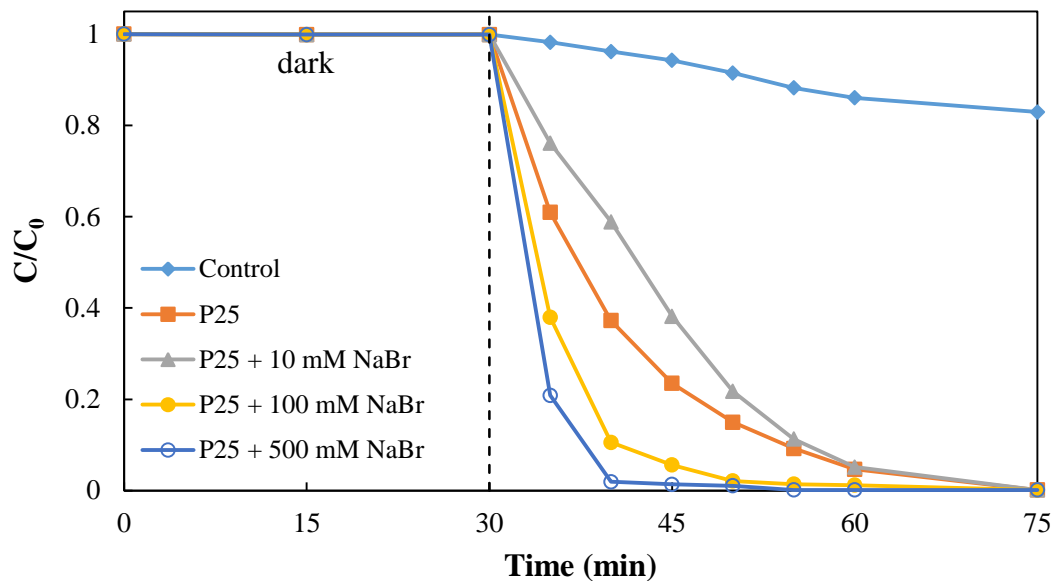


Sunlight is composed of about 5 % UV light, 45 % visible light and 50 % infrared. Among the UV light, sunlight consists of approximately 98.1 % of UV-A light ( $\lambda = 400 \sim 315$  nm), 1.1 % of UV-B light ( $\lambda = 315 \sim 280$  nm) and little UV-C light ( $\lambda = 280 \sim 230$  nm). Although sunlight has little UV-C light, the intensity of sunlight is very high, suggesting that the effect of UV-C light could not be easily ignored. Besides, in full daylight, the illuminance of sunlight can raise up to 100,000 lux.

Appendix 12 illustrated that the photocatalytic degradation of 5 mg/L SMZ by 10 mg/L P25 with different concentrations of NaBr under sunlight irradiation. It can be observed that there was a little degradation of SMZ in the control group, i.e. the pure SMZ solution. The experiment was conducted on a scorching hot day with 100,000 lux of illuminance, indicating that UV-C light may have the influence on the photodegradation. Moreover, SMZ can absorb light within the range between 240 and 310 nm. Therefore, the degradation of the control group could be explained that SMZ absorbed the UV-C light of sunlight, and then degraded by photolysis process.

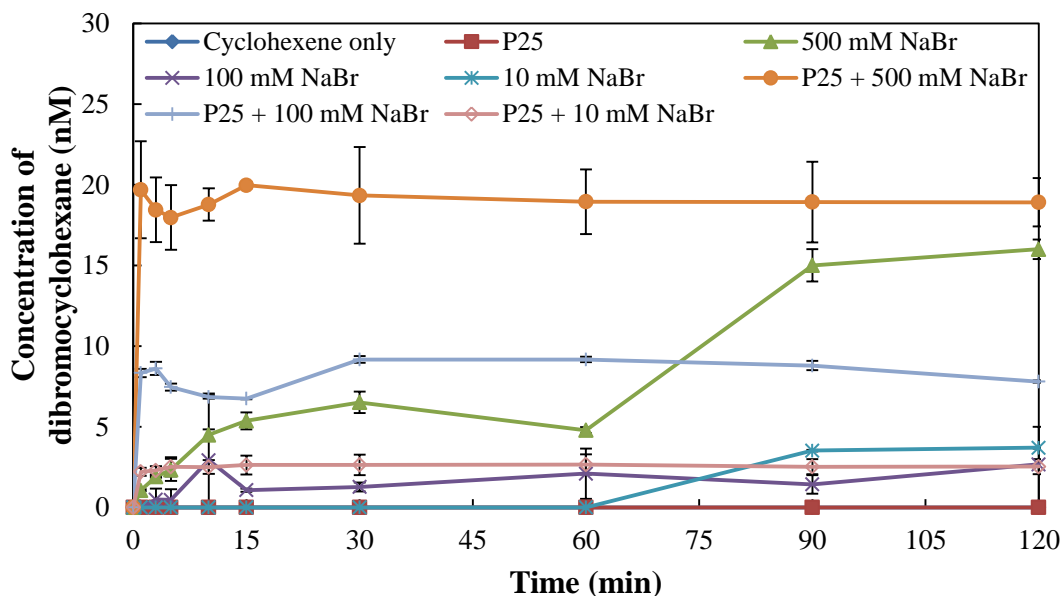
Under sunlight irradiation, the addition of  $\text{Br}^-$  still increased the photodegradation rate of SMZ by P25. This enhancement enlarged as the bromide concentration was increased. With the addition of 100 mM NaBr, the photodegradation efficiency was 99 % after 20 min illumination, and reached degradation equilibrium. Moreover, in the presence of 500 mM NaBr, the removal efficiency of SMZ was 99 % after just 10 min of irradiation.





Appendix 12. The photocatalytic degradation of 5 mg/L SMZ by 10 mg/L P25 with different concentrations of NaBr under sunlight irradiation. (Light intensity: 100,000 lux, temperature: 34.4 °C)

Figure 4-41 showed the result of dibromocyclohexane test under 15 min illumination, while Appendix 13 was presenting the result of dibromocyclohexane test under 120 min illumination. There was no dibromocyclohexane generated under irradiation for 2 hr in the system containing only cyclohexene or P25. Once upon irradiation, trans-1,2-dibromocyclohexane quickly generated in the system containing P25 and 500 mM NaBr. Within 1 min of irradiation, the concentration of generated dibromocyclohexane increased rapidly to 20 nM, and then reached the equilibrium. However, in the system containing 500 mM NaBr, there was a little dibromocyclohexane formed in the beginning. After 60 min, the concentration of dibromocyclohexane increased to 15 nM, exceeding the dibromocyclohexane concentration in the system containing P25 and 100 mM NaBr.



Appendix 13. The result of dibromocyclohexane test.

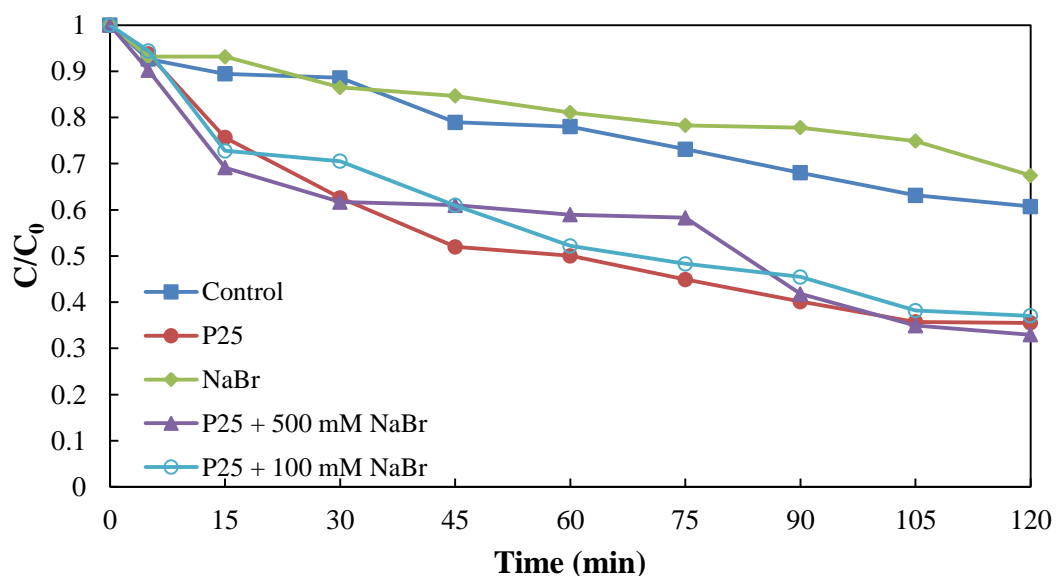
Oosting and Reijnders (1980) reported that after bromide is oxidized, the liberated bromine reacts with fluorescein to yield the intensively colored eosin. Other studies also elucidated that bromine can react with fluorescein (Jennings & Elia, 1996; Marczenko & Balcerzak, 2000). García-Figueroa et al. (2017) described the chemical reactions involved as follows:



If there is bromine existed in the system, the fluorescein will react with bromine and thus the fluorescence intensity will decrease. Therefore, the fluorescence intensity of fluorescein was measured, and then the concentration of fluorescein was calculated. The excitation and emission wavelengths of fluorescein were set at 470 and 513 nm, respectively.

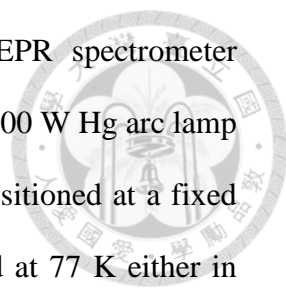
From Appendix 14, it can be observed that the concentration of fluorescein declined under UV light irradiation. In the system of P25 with 100 and 500 mM NaBr, the decrease of fluorescein concentration was larger than fluorescein only, indicating

that there may be some bromine generated. However, in the system of P25, the decrease of fluorescein concentration was almost the same as that of P25 with NaBr. This can be explained that the fluorescein also reacted with  $\bullet\text{OH}$ . Ou et al.(2002; 2001) used fluorescein as a fluorescent probe to detect  $\bullet\text{OH}$  radicals. As a result, the decrease of fluorescein concentration in the system of P25 could be attributed to the  $\bullet\text{OH}$  radicals.



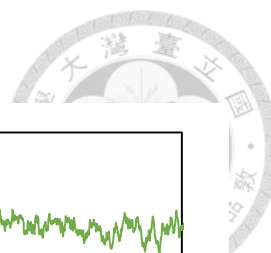
Appendix 14. The result of fluorescein experiment under UV light irradiation. (UV light:  $\lambda = 365 \text{ nm}$ , 32W; Initial concentration of fluorescein: 0.02 mM)

The electron paramagnetic resonance (EPR, or electron spin resonance, ESR) is a powerful tool to detect photogenerated electron-hole pairs on the surface of  $\text{TiO}_2$ . Some radicals such as reactive oxygen species (ROS) and reactive halogen species (RHS) could also be captured by specific probe molecules and then detected by EPR. Here we tested several conditions to investigate the generation of RHS by P25 with the halide ion addition under UV light irradiation.

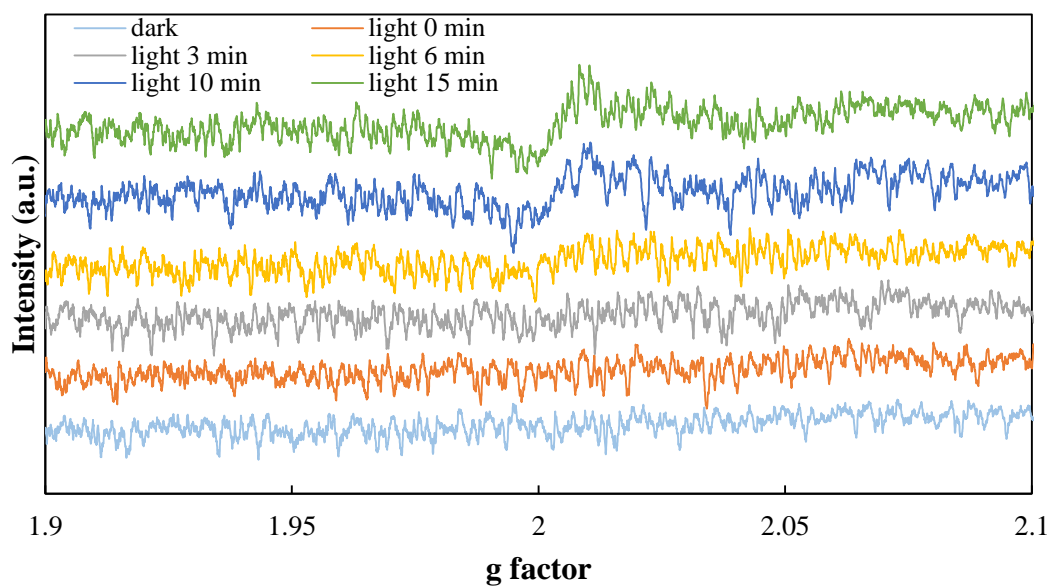


The photoinduced charge carriers were examined by an EPR spectrometer (Bruker ELEXSYS series E-580) working at X-band frequency. A 400 W Hg arc lamp (Oriental Instruments, Model 66021) was used as the light source, positioned at a fixed distance from a sample cavity. The measurements were conducted at 77 K either in the dark or under irradiation. The instrumental conditions were set at a center field of 3400 G and a sweep width of 200.0 G. The microwave frequency was 9.50 GHz and the power was 8.0 mW. The alpha-phenyl-N-tert-butyl nitron (PBN) was used as a probe to trap bromide radicals. The initial concentration of PBN was 100 mM. Subsequently, 1 mL sample solution mixed with 1 mL PBN was delivered into a quartz capillary tube and analyzed the spin-trapped adducts under irradiation at 77K.

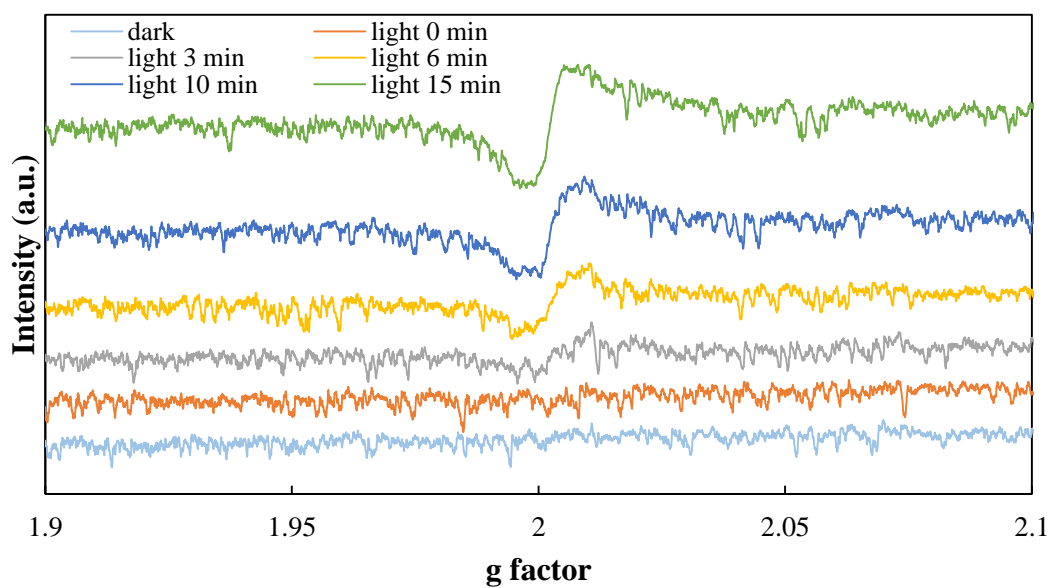
Appendix 15ab presented the EPR results of 10 mg/L P25 with 100 and 500 mM NaBr, respectively. In the system of P25 with 100 mM NaBr, there was a signal detected after 10 min illumination. The intensity of the signal increased with the irradiation time. As for P25 with 500 mM NaBr, the signal could be detected once upon UV light irradiation, and the intensity of the signal increased with the irradiation time. Moreover, the intensity of the signal was stronger than that of P25 with 100 mM NaBr.



(a)



(b)



Appendix 15. The EPR results of (a) 10 mg/L P25 with 100 mM NaBr, and (b) 10 mg/L P25 with 500 mM NaBr.